Alma Mater Studiorum – University of Bologna

RESEARCH DOCTORATE

Fluid machines and Energy Systems

Cycle XXIV

Affiliation sector: 09/C1

Scientific-disciplinary sector: ING-IND/08

Comparative Analysis of Alternative Hybrid Systems for Automotive Applications

Igor Trivić

Doctorate School Coordinator **Supervisor**

Prof. Ing. Vincenzo Parenti Castelli **Prof. Ing. Davide Moro**

Final exam 2012

ACKNOWLEDGMENTS

First of all, I am deeply thankful to my parents and to my brother Branislav who have always been there for me and supported me throughout all my life. Despite the geographical distance in the last few years I always felt their support and encouragement.

It is a great pleasure to thank my supervisor Prof. Ing. Davide Moro for his continued guidance, encouragement, patience and his parental care that added considerably to my academic experience.

Special thanks also goes to Prof. Ing. Nicolò Cavina for helping me and offering support in the most critical moments and who also contributed to this thesis with numerous suggestions.

I am greatly indebted to Ing. Mauro Rioli from IEV Srl, for his guidance and supervision during the last years. I feel very fortunate to have had the opportunity to work with him and benefit from his vast experience of many years in the automotive industry. Thank you Mauro for setting an example in both professional and personal life.

Also I would like to thank IAV Gmbh for financing and supporting this interesting research project and Dr.-Ing. Joerg Ross and Ing. Oliver Dingel for guidance and support during the development of this activity.

At the end I would like to thank all my friends in Bologna that made my doctoral period joyful and colorful. Thanks to Bruno, Giulio, Andrea, Claudio, Federico, Marco F., Marco C., Gianni, Federico, Lisa, Elisa, Roberta, Alberto, Sergio, Davide, Francesco, Mirko, Carlo, Gherardo, Gaspare, Giorgio and all the others that made my stay in Bologna a memorable experience.

CONTENTS

1. **INTRODUCTION**

Fuel consumption reduction has become the most important driver for engine, powertrain and vehicle development at present. The general concern about the effect of CO_2 emissions on the environment and the global energy situation as well as the new taxes approved by EU Community on CO_2 emissions together with the taxes proposal by the USA legislation are forcing all car manufacturers to develop new technologies and to identify the best solutions for CO_2 reduction. It is well known that for a relatively long time many research centers and the most innovative car manufacturers have been presenting to the market various "environment friendly" solutions that were promised to achieve better fuel economy. It can be said that quite a lot of the possible technologies have been in some way investigated or applied: at first within the internal combustion engine itself (downsizing and down-speeding, reduction of internal and auxiliary losses, various variable valve timing and lift systems etc.), and secondly (more promising) "around the engine". From this second point of view, a hybrid approach has shown to be particularly promising.

In the strict sense, hybrid vehicle is the vehicle that has two or more power sources – conventional internal combustion engine and additional power source (electrical, hydraulic, kinetic, pneumatic etc.). By using a secondary energy converter beside the internal combustion engine, a significant increase of the primary converter efficiency can be achieved (associated with engine downsizing and load point moving) while adding the regenerative braking features to the powertrain.

In the recent years, several car manufacturers have gained significant market share with hybrid electric vehicles (Toyota Prius and Honda Insight). One of the goals of this work was to try to determine if exist viable alternatives to hybrid electric vehicles and what type of alternative hybrid systems could be competitive enough in the light of rigorous hybrid vehicle requirements.

General requirement from any hybrid systems can be summarized as:

- Efficient use of the primary power source (internal combustion engine should be used in the most efficient way)
- Efficient transformation and storage of energy
- Efficient recovering and reuse of energy through regenerative braking

Besides high individual energy efficiency of the hybrid components as well as overall efficiency of the system, other important requirements include controllability and robustness of the system, reliability and especially final cost.

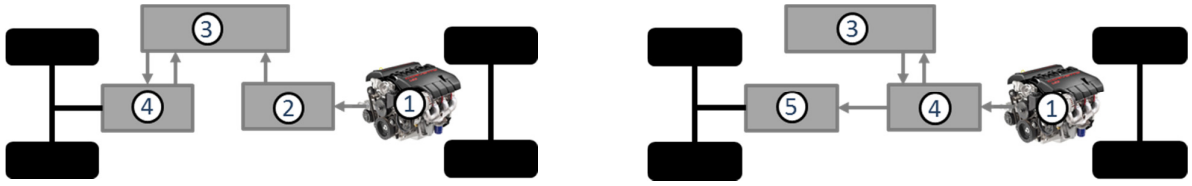

Figure 1.1 – Serial (left) and Parallel (right) hybrid vehicle configuration 1) Internal combustion engine 2) Generator (electric generator, hydraulic pump, pneumatic compressor) 3) Energy storage system (battery, hydraulic accumulator, air storage tank, high speed flywheel) 4) propulsion/generator device (electric motor generator, hydraulic motor pump, pneumatic motor compressor etc.) 5) transmission

Figure 1.1 represents two most typical hybrid powertrain layouts – serial and parallel hybrid.

In the parallel hybrid configuration, internal combustion engine (ICE) and a hybrid propulsion device are mechanically connected to a transmission. Both engine and hybrid propulsion device (electric motor generator, hydraulic motor pump, pneumatic motor compressor, etc.) can work in parallel to supply traction power to the wheel while hybrid system can be used to boost the engine when needed, perform regenerative braking in order to recharge the energy storage system or can propel the vehicle while keeping the engine turned off. In this configuration, the engine speed is cinematically coupled to the wheel and the power can be sent down the mechanical path to the wheels.

In the serial hybrid configuration, the energy produced by the engine is directly converted into some other form of energy (electrical, hydraulic, pneumatic etc.) and is used in that form to propel the vehicle. The advantage of this layout is that engine is completely decoupled from the driveline and can operate in the "sweet spot" i.e. the best efficiency region while the transmission can be completely removed from the powertrain leading to weight and cost reduction. However, this configuration suffers from energy conversion loss which can be a serious drawback.

Combination between parallel and a serial hybrid can be achieved with use of a power-split device that allows the best of both worlds - the power paths from the engine to the wheels that can be either mechanical or hybrid (energy traverses hybrid components in order to reach the wheel which leads to energy loss). In this way the power demanded by the driver is decoupled from the power supplied by the engine while maintaining the possibility to utilize mechanical energy path from the engine to the wheels. With respect to parallel and serial systems, serial-parallel systems might suffer from higher system complexity and cost.

Regarding the degrees of hybridization (i.e. power and energy storage capabilities of hybrid components), several categories of hybrid vehicle can be defined:

- Full Hybrid Vehicle – in the strict sense it is the hybrid vehicle that can utilize hybrid system to propel the vehicle while keeping the internal combustion engine turned off. All general hybrid characteristics apply for this case.
- Mild hybrid vehicle – All general hybrid characteristics apply except the fact that the hybrid system can't be used to propel the vehicle due to its limited capabilities or it can be used in extremely limited fashion.
- Power assist hybrid – hybrid system can be used in order to boost the engine when extra power is required. Further it can perform regenerative braking and start & stop engine operation.

Also, term Plug in Hybrid refers to the hybrid vehicles (or pure electric vehicles) that have the possibility to have their energy storage system recharged externally.

In this work the research activity was carried out in order to investigate conventional (electrical) & non-conventional (mechanical, hydraulic, pneumatic) hybrid systems and their impact on the vehicle fuel economy while applying an optimized cycle-independent control strategy. Selected powertrain layout in all cases is parallel hybrid with the hybrid system connected to the driveline directly between engine and the transmission.

Several new and original concepts are proposed. Innovative layout of the High Speed Flywheel Hybrid vehicle as well as Pneumatic Hybrid vehicle with exhaust gas recuperation is presented and investigated. New expansion of the standard control strategy algorithm is proposed that will take into account optimized gear shift pattern of the vehicle in order to further reduce fuel consumption.

In other words, the main objective was to demonstrate that also non-conventional hybrid layouts could (and should) be fully exploited to achieve the best possible results in terms of cycle overall fuel economy, extending and widening the mainstream hybrid perspectives of the present.

2. BASE VEHICLE MODELING AND SIMULATION

2.1 SIMULATION TOOL DESCRIPTION

In order to perform the analysis of different hybrid concepts, IAV Gmbh simulation tool "VeLoDyn 2.16.2" (Vehicle Longitudinal Dynamics Simulation) has been used as a common base platform. VeLoDyn is a Matlab/Simulink based software tool which offers a straightforward simulation of longitudinal vehicle dynamics with special considerations on the driveline. Due to its modular nature and high flexibility it can be used in order to perform not only concept studies and algorithm development, but also HIL/MIL/SIL simulations. In order to perform analysis of different hybrid systems in short time, the modular and adaptive nature of VeLoDyn was crucial since it offered the possibility of implementing different model blocks into the existing powertrain structure with little effort.

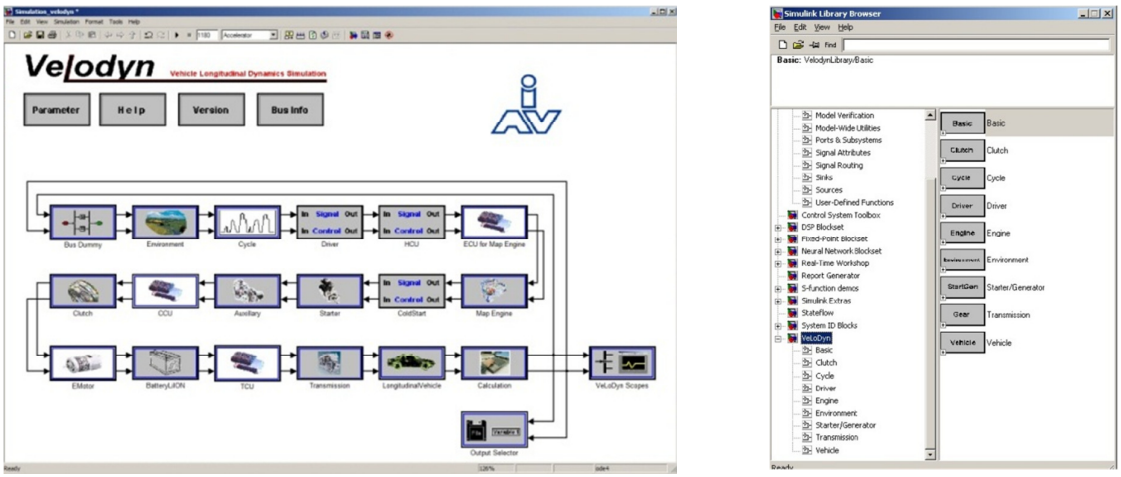

Figure 2.1.1 – VeLoDyn layout (left) and VeLoDyn Library (right)

VeLoDyn library already includes numerous blocks of different powertrain components that provided the basis for analysis presented in this work. However, in order to simulate alternative hybrid systems, new (physical) models of hybrid components had to be developed and incorporated into the VeLoDyn framework. Newly developed models included High Speed Flywheel Hybrid components (CVT and HSF), hydraulic components (Hydro-pneumatic accumulators, Hydraulic Motor Pump), pneumatic components (Pneumatic Motor Compressor, Air Storage Tank) and development of sub-control blocks of individual systems. All developed models as well as Supervisory Control Strategy block used for hybrid comparative analysis of different systems will be presented in the following chapters.

The longitudinal forces that are acting on the two-axle vehicle that is moving on the inclined road are presented in the Figure 2.2.1.

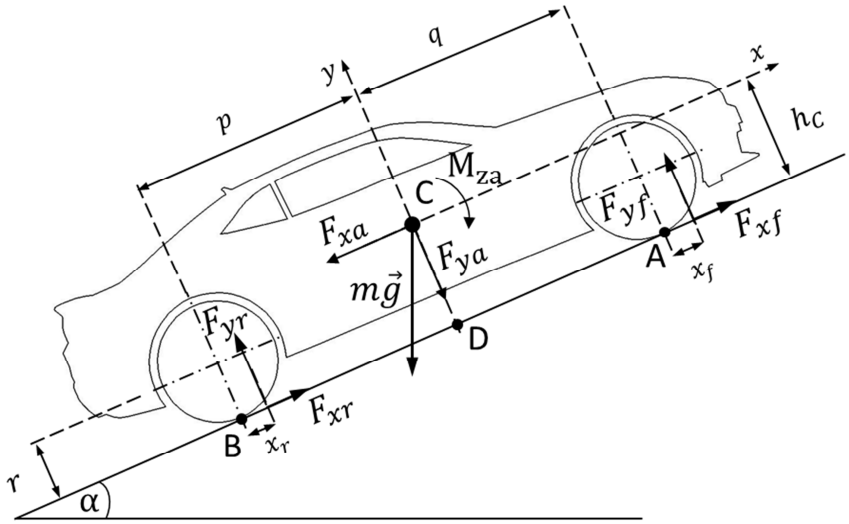

Figure 2.2.1 Forces acting on the moving vehicle on the inclined road [28]

According to 2nd Newton's law, the resulting force that is acting on the moving mass can be defined as:

$$\vec{F}_R = \sum_i \vec{F}_i = m \cdot \frac{d\vec{v}}{dt} \qquad (2.2.1)$$

In the general case, the forces that are acting on the moving vehicle include traction force ($\vec{F}_{engine}$) supplied to the driveline by the internal combustion engine or any other form of propulsion systems (i.e. electric motor etc.), aerodynamic resistance force ($\vec{F}_{aero}$), rolling resistance force ($\vec{F}_{rr}$) and braking force ($\vec{F}_{brake}$).

$$\vec{F}_R = \sum_i \vec{F}_i = \vec{F}_{engine} - \vec{F}_{aero} - \vec{F}_{rr} - \vec{F}_{brake} \qquad (2.2.2)$$

Traction force ($\vec{F}_{engine}$) is generally considered positive since it is applied in order to propel the vehicle. However, in certain cases when the internal combustion engine is in cut-off conditions and the engine clutch is closed the engine can supply negative torque to the driveline therefore acting as a brake (engine braking). Braking force of the vehicle can be related to both mechanical and regenerative braking (hybrid vehicles).

Aerodynamic drag force offers resistance to the movement of the vehicle and is a function of the vehicle speed and the aerodynamic characteristics of the vehicle and can be expressed with the following relation:

$$F_{aero} = \frac{1}{2}\rho_{air} C_d A_x (v - v_{wind})^2 \qquad (2.2.3)$$

Where $C_d A_x$ is a product of the drag coefficient and surface area of the vehicle while ρ_{air} is the air density and v_{wind} is the wind speed.

In the general case rolling resistance force F_{rr} can be expressed with simple relation as:

$$F_{rr} = f_{rr} \cdot N \qquad (2.2.4)$$

Where f_{rr} is the rolling resistance coefficient and N is the normal load supplied to the wheel.

The rolling resistance coefficient generally depends on multiple factors like the material and structure of the pneumatic, vehicle speed, terrain characteristics or temperature and pressure of the pneumatic. It is usually determined experimentally and its value can be represented by polynomial function [28] as:

$$f_{rr} = \sum_{i=1}^{n} C_i v^i \qquad (2.2.5)$$

Where v is the vehicle speed.

The existence of rolling friction lies in the fact that energy of deformation of elastic material (such as rubber) is greater than the energy of recovery [28]. During motion, wheel tire experiences repeated cycles of deformation where part of the energy used to deform the pneumatic is converted into heat and dissipated to the surroundings. This phenomenon called hysteresis is contributed the viscoelastic characteristics of pneumatic material.

On basis of the Figure 2.2.1, equilibrium of the forces in direction x and y are given in the equations (2.2.6) and (2.2.7).

$$m \cdot \frac{dv}{dt} = F_{xf} + F_{xr} - F_{xa} - mg \sin\alpha \qquad (2.2.6)$$

$$0 = F_{yf} + F_{yr} - F_{ya} - mg \cos\alpha \qquad (2.2.7)$$

Moment equilibrium [28] for the point D can be expressed with following equation:

$$F_{yf}(q + x_f) - F_{yr}(p - x_r) + mgh_c \sin\alpha - M_a + F_{xa} \cdot h_c = -m \cdot \frac{dv}{dt} h_c \qquad (2.2.8)$$

It can be considered that the traction energy supplied by the engine is primarily used in order to increase vehicle's translational kinetic energy. However, a part of that energy is lost in order to accelerate all rotational components of the vehicle (transmission shafts, wheels etc.)

On basis of the energy equation that states that total kinetic energy of the vehicle can be represented as an energetic sum of all rotational and translation components:

$$\frac{1}{2} J_{ref} \omega_e^2 = \frac{1}{2} m v^2 + \sum_i J_i \cdot \omega_i^2 \qquad (2.2.9)$$

Referred vehicle inertia on the engine crankshaft can be defined as:

$$J_{ref} = J_e + \frac{J_t}{\tau_t^2} + \frac{J_w}{\tau_t^2 \tau_d^2} + \frac{mr^2}{\tau_t^2 \tau_d^2} \qquad (2.2.10)$$

Where τ_d and τ_t stand for transmission ratio of the differential and gearbox respectively.
The main dynamic equation that defines the angular velocity of the engine crankshaft is defined as:

$$J_e \dot{\omega}_e = T_e - T_r \qquad (2.2.11)$$

Where J_e is the engine total inertia, T_e is the engine effective torque and T_r is the resistant torque applied at the engine crankshaft.

On basis of the equation 2.2.11, angular velocity of the engine crankshaft can be expressed in time domain as:

$$\omega_e = \int \frac{T_e - T_r}{J_e} dt \qquad (2.2.12)$$

And in the (crankshaft) angular domain as:

$$\omega_e = \int \frac{T_e - T_r}{J_e \omega_e} d\vartheta \qquad (2.2.13)$$

2.3 STEADY STATE MODEL VALIDATION

The main objective of this work was to model, simulate and analyze fuel efficiency and performance of different hybrid powertrain solutions that could be applied to a standard passenger vehicle. The basic vehicle powertrain layout used as a basis for hybrid analysis is represented in Figure 2.3.1, while its main specifications are given in the Table 2.3.1.

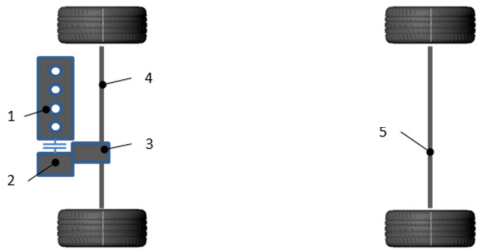

Figure 2.3.1 – Basic (conventional) vehicle powertrain layout 1-ICE 2- Automated Manual Transmission (AMT) 3-Differential 4-Front axle (semi-axle) 5-Rear axle

The base vehicle is a mid-sized vehicle that has a conventional front wheel drive powertrain with transversally positioned engine as represented in Figure 2.3.1. Power from the ICE is delivered through the 7 speed Automated Manual Transmission (AMT), differential and finally through the semi-axles to the wheels. The vehicle is equipped with a 1.4 liter direct injection turbo gasoline engine (90 kW maximal power and 200 Nm maximal torque).

The overall vehicle model includes a representation of the driver (both open-loop and closed-loop driver actions can be simulated, the latter being the typical driving cycle scenario), a simplified description of the ICE (mainly torque and fuel consumption maps), and a detailed clutch, transmission and vehicle longitudinal dynamics sub-models. Finally, VeLoDyn integrates engine, transmission, vehicle and control systems models within the very same simulation environment.

Additional energy converters were always integrated into the conventional powertrain layout shown in Figure 2.3.1, and the investigated hybrid layouts were in all cases parallel hybrid configurations, as it will be explained in detail in the following chapters.

Base vehicle specifications		
weight	[kg]	1470
Drag coefficient	[-]	0.311
Frontal area	[m^2]	2.22
Wheel radius	[m]	0.3083
Rolling friction	[-]	0.8
Overall transmission ratio 1st gear	[-]	16.69
Overall transmission ratio 2st gear	[-]	10.08
Overall transmission ratio 3st gear	[-]	6.79
Overall transmissions ratio 4st gear	[-]	4.97
Overall transmission ratio 5st gear	[-]	3.81
Overall transmission ratio 6st gear	[-]	3.07
Overall transmission ratio 7st gear	[-]	2.55
Driveline overall efficiency	[-]	0.9
Engine: 1.4l TFSI 90kW 200Nm		

Table 2.3.1 – Vehicle specifications

Base vehicle model was validated on basis of the experimental data for a set of constant vehicle speed points and for warm engine conditions. Engine speed and effective torque, as well as fuel consumption were simulated and compared to the experimental data for a series of constant vehicle speed ranging from 50-120 km/h and the results are present in the following figures.

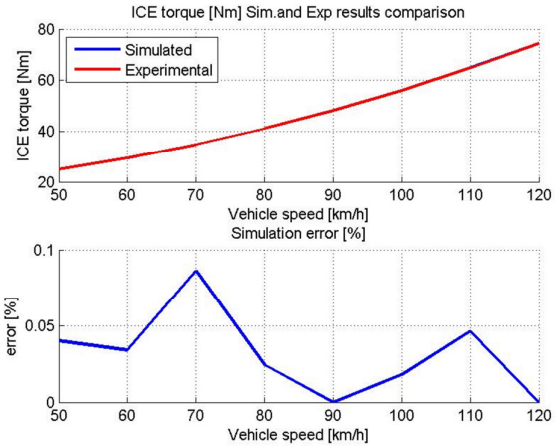

Figure 2.3.2 Comparison between simulated and experimental engine torque during steady state conditions [Nm]

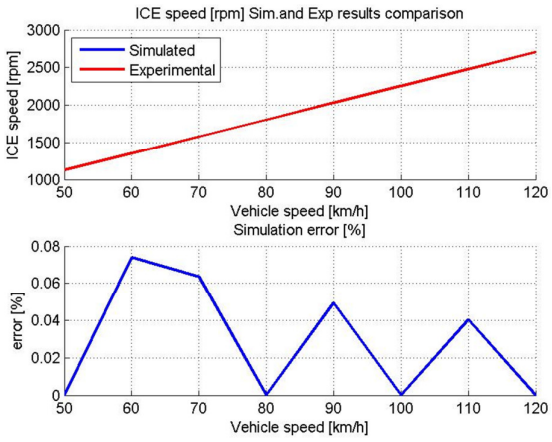

Figure 2.3.3 Comparison between simulated and experimental engine speed during steady state conditions [rpm]

As it can be seen from figures 2.3.2 and 2.3.3 simulated engine speed and torque values correspond very well to the experimental results. However, as it can be observed from the Figure 2.3.4 there is a slight difference between simulated and experimental trend of fuel consumption. This can be contributed to the fact the error was possibly committed during measurements of the engine fuel consumption on the test bench. Nevertheless, this was not of significant importance for this analysis, since the relative fuel consumption difference between base vehicle and different hybrid solutions was pursued.

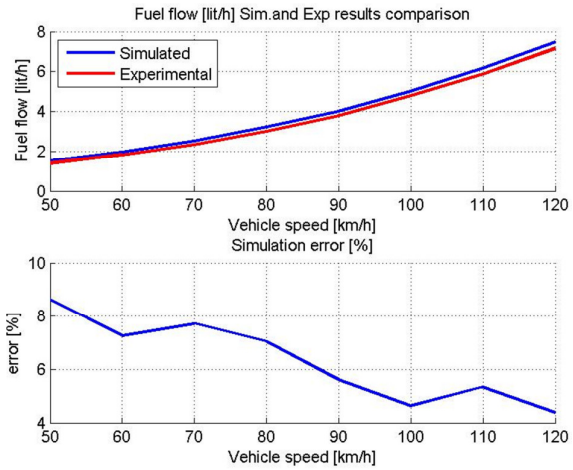

Figure 2.3.4 Comparison between simulated and experimental fuel consumption during steady state conditions [lit/h]

2.4 SIMULATION RESULTS

In order to provide a base for hybrid vehicles Fuel Economy (FE) analysis, the first simulations were performed on the standard vehicle, using the vehicle parameters given in Table 2.3.1. The results present in this chapter are for the standard vehicle without Start & Stop. Effect of engine cold start has not been taken into account both in base and hybrid vehicle simulations and the relative difference between base and hybrid vehicle was analyzed. Figure 2.4.1 represents base vehicle fuel economy results [lit/100km] for several different homologation cycles.

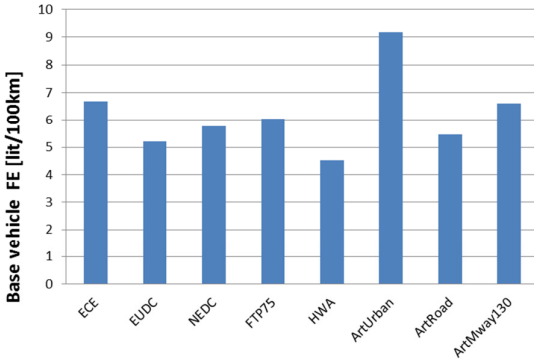

Figure 2.4.1 - Base vehicle Fuel Economy [lit/100km] during several homologation cycles

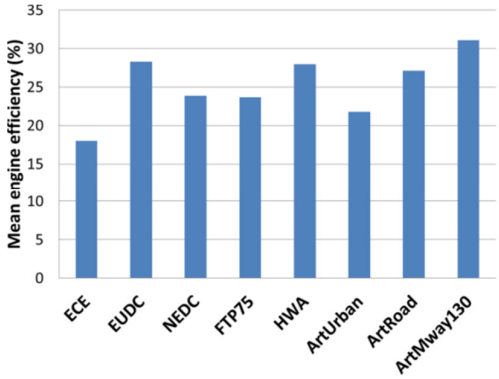

Figure 2.4.2- Mean engine efficiency for base vehicle during several homologation cycles

Figure 2.4.2 represents mean engine efficiency during different homologation cycles. As can be observed, city cycles that require part load engine operation typically result in lower mean engine efficiency (ECE 17%, Artemis Urban Cycle 22%) when compared to extra urban and motorway cycles (EUDC 28% and Artemis Motorway 130km/h 31%).

Figure 2.4.3 represents example of the distribution of engine operating points in seconds during New European Driving Cycle (NEDC), where the low engine efficiency zones (high BSFC values) are mainly related to the urban part of the NEDC cycle (engine is operated in the partial load conditions in the 0÷ 2 bar BMEP region).

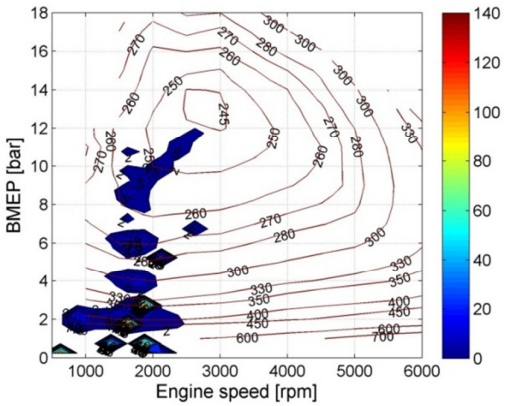

Figure 2.4.3- Distribution of ICE operating points (sec) during NEDC cycle

Figure 2.4.4 represents powertrain energetic analysis of the base vehicle during NEDC cycle where all the energies are referred to the primary AMT shaft.

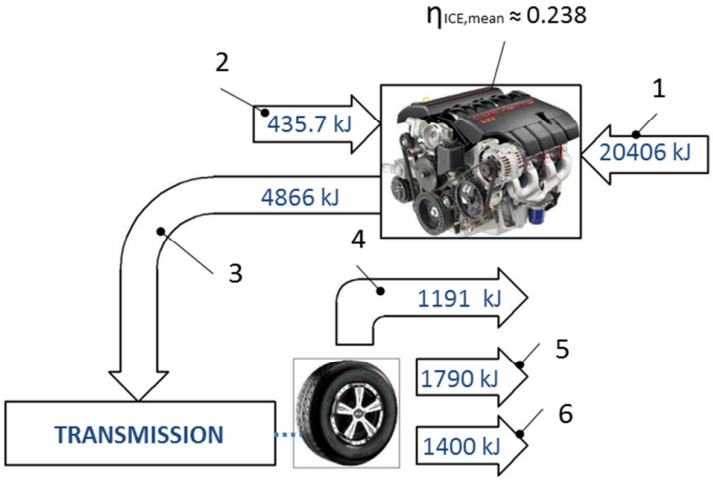

Figure 2.4.4– Base vehicle powertrain energetic analysis for NEDC cycle (all energies are referred to the primary AMT shaft axis): 1- Fuel energy input 2- Engine braking 3- Traction energy 4-Mechanical braking energy 5-Aerodynamic resistance energy 6-Rolling resistance energy

Position 1 in Figure 2.4.4 refers to the energy equivalent to the quantity of the fuel consumed during the cycle, while position 3 represents energy produced by the engine and supplied for the traction. Position 2 represents engine braking energy (cut-off conditions) while positions 4, 5 and 6 represent mechanical braking, rolling resistance and aerodynamic energy loss respectively.

As it can be observed from Figure 2.4.4, mean engine efficiency during the cycle is 23.8 % while 1191 kJ of energy is lost (into heat) due to mechanical braking and 435.7 kJ of energy is lost during engine braking. In order to improve cycle fuel economy part of braking energy could potentially be recovered by the utilization of Kinetic Energy Recovery System, stored in some form and reapplied to the driveline when requested. Also, hybrid system could be utilized in order to propel the vehicle in part load conditions (while maintaining the engine turned off) or could be utilized to perform load point shift of the engine to the zones of higher efficiency while storing excess energy produced by the energy.

3. HYBRID ENERGY MANAGEMENT STRATEGY

3.1 GLOBAL ENERGY MANAGEMENT APPROACH

Comparative analysis of alternative hybrid systems for automotive applications presented in this work was carried out for several different hybrid types:

- Hybrid Electric Vehicle (HEV)
- High Speed Flywheel Hybrid Vehicle (HSF-HV)
- Hydraulic Hybrid Vehicle (HHV)
- Pneumatic Hybrid Vehicle (PHV)

In order to provide optimal hybrid powertrain control of different hybrid systems and to maximize vehicle fuel economy in every driving condition, an advanced energy management strategy was implemented. The operating strategy was based on Equivalent Consumption Minimization Strategy (ECMS) [3, 4, 5 and 6] and the control algorithm was adapted for all hybrid cases. The ECMS that can be regarded as a cycle independent control strategy without the knowledge of driving cycle "*a priori*" therefore suitable to give fuel economy results that might occur in real world driving conditions. The implemented algorithm was robust enough to support very different hybrid systems with little re-calibration effort. Figure 3.1.1 represents layout of the control strategy operation with main control signals.

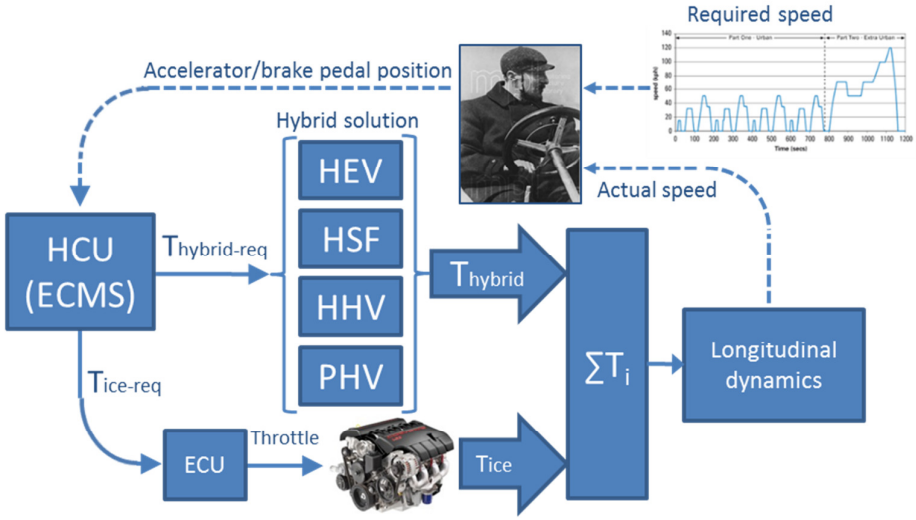

Figure 3.1.1 – Global Power Management approach in a parallel hybrid configuration for different hybrid systems analyzed in this paper (HEV, HSF, HHV and PHV)

As demonstrated in Figure 3.1.1 closed loop PID controller (that simulates driver behavior) supplies vehicle accelerator and brake pedal requests to the top-level "supervisory" Hybrid Control Unit (HCU). Hybrid Control Unit (HCU) that operates on basis of ECMS determines the optimal power split ratio between the ICE and the hybrid part of the powertrain (Figure 3.1.1 – HEV or HSF or HHV or PHV) and sends power/torque requests to the individual control units (ECU for the engine and hybrid (Electric, Hydraulic, Pneumatic, Kinematic) control unit for each hybrid system). In order to minimize fuel consumption during zero power intervals as well as during hybrid only traction, the internal combustion engine is shut down, thus inherently assuming start-stop capability.

The main task of the Hybrid Control Unit (HCU) is to determine optimal torque split ratio $u(t)$ in order to achieve minimum overall energy consumption of the whole hybrid powertrain. Power split ratio can be defined with the following relations:

$$T_{req}(t) = T_{ice-req}(t) + T_{hybrid-req}(t) \qquad (3.1.1)$$

$$T_{ice-req}(t) = \big(1 - u(t)\big) \cdot T_{req}(t) \qquad (3.1.2)$$

$$T_{hybrid-req}(t) = u(t) \cdot T_{req}(t) \qquad (3.1.3)$$

Where T_{req}, $T_{ice-req}$and $T_{hybrid-req}$ are requested torque from powertrain in order for the vehicle to follow required speed profile (driver input), requested torque from the engine, and requested torque from the hybrid part of the powertrain (HEV or HSF or HHV or PHV) respectively. Also, it has to be noted that power split factor is determined not only on the basis of driver request and "minimum hybrid energy consumption" but also taking into account the current state of engine and hybrid components (i.e. "hybrid drive only" will not be requested if the SOC value is below minimum value, or during recharging of the hybrid "battery" the requested power will not exceed engine capabilities, etc. (in this context the term battery relates not only to the electrical battery, but High Speed Flywheel (HSF), Air Storage Tank (AST) and Hydraulic accumulator as well)). Torque split factor can be analyzed for four distinct cases (Eq.3.1.4): equal to one value would imply hybrid only operation (either hybrid driving when engine is turned off or regenerative braking); when between 0 and 1 both engine and hybrid part will provide positive power to the wheels and the power repartition will be defined by power split value (this case can be regarded as hybrid "boost"); when equal to zero vehicle will perform as conventional vehicle (hybrid part of the powertrain will be inactive). For the power split values below zero, engine will perform battery recharging while the power split value $u(t)$ will define the recharging intensity. Also, minimal power split value n will be limited by the maximal available ICE or hybrid power.

$$n \le u(t) \le 1 \equiv \begin{cases} u(t) = 1 \\ 0 < u(t) < 1 \\ u(t) = 0 \\ n \le u(t) < 0, n_{min} = f\big(P_{ice,max}, P_{hybrid,max}\big) \end{cases} \qquad (3.1.4)$$

In order to determine torque split ratio $u(t)$ that will result in the minimal overall energy consumption, Equivalent Minimization Consumption Strategy is introduced. ECMS deals with the concept of a global energy function cost [6] that take into account cost of the chemical energy of the fuel and of the hybrid energy dependent only on the system variables at the current time step. Global function cost $J(t,u)$can be expressed with the following equation

$$J(t,u) = \Delta E_{chemical}(t,u) + s(SOC) \cdot \Delta E_{hybrid}(t,u) \qquad (3.1.5)$$

The main objective therefore is to resolve the instantaneous minimization problem of the global function cost with respect to different system constraints (physical characteristics of the components, driver demand, energy capacity limitations etc.). Further, Equation (3.1.5) can be expressed in terms of referred fuel consumption of the whole hybrid powertrain as [6]:

$$\dot{m}_{ref}(t,u) = \dot{m}_f(t,u) + \dot{m}_{eq}(t,u) \qquad (3.1.6)$$

Where $\dot{m}_f$ is the engine instantaneous fuel consumption and $\dot{m}_{eq}$ is the "virtual" fuel consumption that can be related to the use of hybrid energy source. Equivalent fuel consumption $\dot{m}_{eq}$ can be expressed as:

$$\dot{m}_{eq}(t,u) = \frac{s_{act}}{Q_{lhv}} \bar{\eta}_{hybrid} P_{hybrid}(t,u) \qquad (3.1.7)$$

Where P_{hybrid} is the delivered hybrid power, s_{act} is the equivalency factor that represents the cost of converting energy of the hybrid power source into equivalent fuel consumption, $\bar{\eta}_{hybrid}$ is the efficiency of the hybrid path, while Q_{lhv} is the lower heating value of the fuel. Equivalency factor has been determined by means of SOC correction function f_{SOC} that assumes a form similar to Proportional-Integral (PI) controller [5]

$$s_{act} = f_{SOC}\big(S_{batt}(t)\big)\bar{s}_{nom}(t) \qquad (3.1.8)$$

Where:

$$f_{SOC}\big(SOC_{batt}(t)\big) = \left[1 + \left(\frac{SOC_{batt,ave}(t) - SOC_{batt}(t)}{SOC_{batt,ave}(t) - SOC_{batt,min}(t)}\right)^{2n_{SOC}+1}\right] \cdot$$

$$\left[1 + \tanh\left(\frac{f_{SOC,I}(SOC_{batt}(t)}{SOC_{batt,th}}\right)^{2n_{SOC}+1}\right] \qquad (3.1.9)$$

$$f_{SOC,I}(SOC_{batt}(t) = 0.99 f_{SOC,I}(t - \Delta T) + 0.01\left(SOC_{batt,ave}(t) - SOC_{batt}(t)\right) \qquad (3.1.10)$$

Where ΔT is the ECMS sampling rate, SOC_{min} - minimum SOC value, SOC_{max}- maximal SOC value, $SOC_{batt,th}$- tolerance of the hyperbolic function, $SOC_{batt,ave}$- average SOC value.
$\bar{s}_{nom}$ represents nominal equivalency factor value and it can be defined as:

$$\bar{s}_{nom}(t) = s_{nom} + x(SOC) \qquad (3.1.11)$$

Where s_{nom} is the constant value pre-defined for the different hybrid types. In order to improve the ability of the SOC correction function f_{SOC} to deal with the cycles that have very diverse driving dynamics (i.e. real world driving conditions) and to avoid recalibration of the strategy for every specific hybrid case, additional adaptive algorithm was implemented. Charge Sustaining Adaptive Algorithm (CSAA) that worked in the closed loop monitoring of the SOC behavior during the cycle, was used to aggressively update the pre-imposed nominal equivalency factor s_{nom} value at discrete time intervals adding the correction factor x.

Clearly, the necessity of using SOC correction function to modify the equivalency factor value for "real-time" applications when the cycle in not known a priori [5] offers control simplicity and robustness but also suboptimal optimization results when compared with advanced adaptive (and predictive) algorithms [3].

Local minimum of the referred fuel consumption $\dot{m}_{ref}$ is determined by means of iterative analysis during every simulation step.

$$\dot{m}_{ref}(u,t)\big|_{min} \rightarrow ?$$

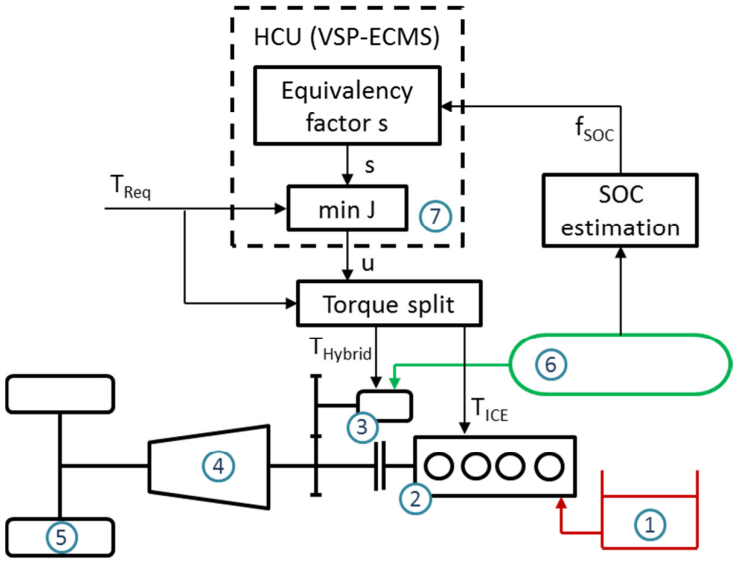

Figure 3.1.2 Implementation of the ECMS strategy

1-Fuel tank 2-Internal combustion engine 3-Hybrid propulsion device (Electric Motor Generator, Hydraulic Motor Pump, Pneumatic Motor Compressor or Continuously Variable Transmission) 4-7 speed Automated Manual Transmission (AMT) 5- Wheel 6- Energy storage system (Li-Ion battery, Hydraulic accumulator, Air Storage Tank, High Speed Flywheel) 7- Supervisory Hybrid Control Unit with VSP-ECMS

Figure 3.1.2 demonstrates basic schematic of parallel hybrid operation with ECMS. Positions 2 represent internal combustion engine and position 3 represents hybrid propulsion device (Electric Motor Generator, Hydraulic Motor Pump, Pneumatic Motor Compressor and Continuously Variable Transmission). Fuel tank is given in Position 1 while Position 6 represents Hybrid Energy Storage system (Electro-chemical battery, Hydro-pneumatic accumulator, High speed flywheel, Air storage tank). The supervisory control strategy block with input/output control signals is graphically represented in Position 7.

ECMS constraints that are taken into account during iterative search for function cost minimal are defined as:

$$P_{req}(t) = P_{ice}(t) + P_{hybrid}(t) \qquad (3.1.12)$$

$$SOC_{min}(t) \leq SOC(t) \leq SOC_{max}(t) \qquad (3.1.13)$$

$$0 \leq P_{ICE}(t) \leq P_{ICE,max}(t) \qquad (3.1.14)$$

$$0 \leq \left|P_{hybrid}(t)\right| \leq \left|P_{hybrid,max}(t)\right| \qquad (3.1.15)$$

In case of HEV, minimal and maximal State of Charge values are limited by the physical properties of the battery between 40-80% respectively. In the case of HSF however, maximal SOC value is related to the maximal permissible flywheel angular velocity while minimal SOC value is considered zero when flywheel is at standstill. Obviously ability to use full SOC range represents one of the advantages when using mechanical energy storage (flywheel) over chemical (Li-Ion

batteries). The same consideration regarding utilization of the full scale range of the SOC is valid also in the case of HHV and PHV systems.

$$(HEV)\ 0.4 \leq SOC(t) \leq 0.8 \qquad (3.1.16)$$

$$(HSF) \quad 0 \leq SOC(t) \leq 1 \qquad (3.1.17)$$

$$(HHV) \quad 0 \leq SOC(t) \leq 1 \qquad (3.1.18)$$

$$(PHV) \quad 0 \leq SOC(t) \leq 1 \qquad (3.1.19)$$

In the case of Hybrid Electric Vehicle, hybrid power is limited by the EMG and battery power limits both in motor and generator mode while in the case of High Speed Flywheel system, power during charging and discharging is limited not only by the CVT power capability but also the limits of the HSF clutch. HHV and PHV power limits are determined by the Hydraulic Motor-Pump (HMP) and Pneumatic Motor Compressor (PMC) characteristic respectively and available pressure difference at the input and output ports.

$$(HEV)\ P_{emg,min}(t) \leq P_{emg}(t) \leq P_{emg,max}(t) \qquad (3.1.20)$$

$$(HEV)\ P_{dis,max}(SOC) \leq P_{batt}(SOC) \leq P_{chg,max}(SOC) \qquad (3.1.21)$$

$$(HSF) \quad 0 \leq |P_{CVT}(t)| \leq \left|P_{CVT,max}(t)\right| \qquad (3.1.22)$$

$$(HSF) \quad 0 \leq |P_{Clutch}(t)| \leq \left|P_{Clutch,max}(t)\right| \qquad (3.1.23)$$

$$(HHV) \quad P_{HMP,min}(t) \leq P_{HMP}(t) \leq P_{HMP,max}(t) \qquad (3.1.24)$$

$$(PHV) \quad P_{PMC,min}(t) \leq P_{PMC}(t) \leq P_{PMC,max}(t) \qquad (3.1.25)$$

The ECMS can be regarded as a cycle independent control strategy with possibility for real-time applications since it has low computational complexity. Also as demonstrated in [4] it results in slightly sub-optimal results when compared to Dynamic Programming but well within acceptable limits.

Further, ECMS is highly dependent on proper calibration of equivalency factor since incorrect value will lead to non-charge sustaining behavior of the vehicle and poor performance and fuel economy. It has to be noted that Dynamic Programming approach would lead to the optimal results for a specific homologation cycle, but one of the goals of this work was to perform the analysis of the different systems in the conditions that would correspond as close as possible to the real world driving conditions when the driving cycle in not known *a priori*. Therefore it was necessary to implement the energy management strategy that will be self-sustaining and cycle independent, giving more realistic behavior of the powertrain in the diverse (and "unexpected") driving conditions.

A common occurrence when implementing ECMS is the problem that control outputs keep oscillating very quickly between sometimes very different states [6]. In these conditions, equivalent cost may have very similar values between close search intervals, leading to multiple switching to sometimes very different operating conditions [5,6]. Clearly this would lead to unacceptable powertrain behavior and could have negative influence on the passenger comfort. This phenomenon called chattering had to be addressed in order to have driveline stability and realistic operation. In order to address this problem, input signal (requested torque from the powertrain Eq. 3.1.1 that originated from the closed-loop PID controller) was subjected to low-pass filter and secondly,

hysteresis block was added to the output of the ECMS strategy in order to monitor variation of the power-split factor $u(t)$ (Eq. 3.1.4) and not to permit powertrain mode changes when change interval was below predefined time threshold.

3.2 VARIABLE SHIFT PATTERN (VSP)-ECMS ALGORITHM DESCRIPTION

As described in the previous text, the main idea behind Equivalent Consumption Minimization Strategy is to reduce global criterion to instantaneous optimization problem [3, 4, 5 and 6]. Further, the advantage of the EMCS over global optimization approach (i.e. Dynamic programming) is the possibility of real-time application on-board the vehicle. For that purpose interesting adaptive ECMS algorithm was presented in [3] in order to update the strategy parameters in function of the driving conditions. The approach relies on using Global Positioning System (GPS) (or auto regressive mathematical models) in order to predict near future driving conditions (vehicle speed and load, terrain elevation etc.) for optimal ECMS operation, minimal fuel consumption and in order to maintain SOC within the given boundaries (charge sustaining behavior).

In this work another expansion of ECMS algorithm is proposed. Variable Shift Pattern ECMS algorithm (VSP-ECMS) was developed and implemented into the ECMS framework in order to investigate impact of the optimized (variable) shift pattern on the vehicle fuel economy during standard homologation cycle (in this case all the analysis were performed on the NEDC and FTP75 cycles). The VSP-ECMS algorithm is given in Figure 3.2.1.

As described in the previous chapter, EMCS performs iterative search in order to find power split factor that will yield minimal global function cost between engine and hybrid system for given conditions. VSP-ECMS imposes utilization of another iterative search loop in order to investigate minimal function cost (and corresponding power split factors) for current as well as previous and successive gears.

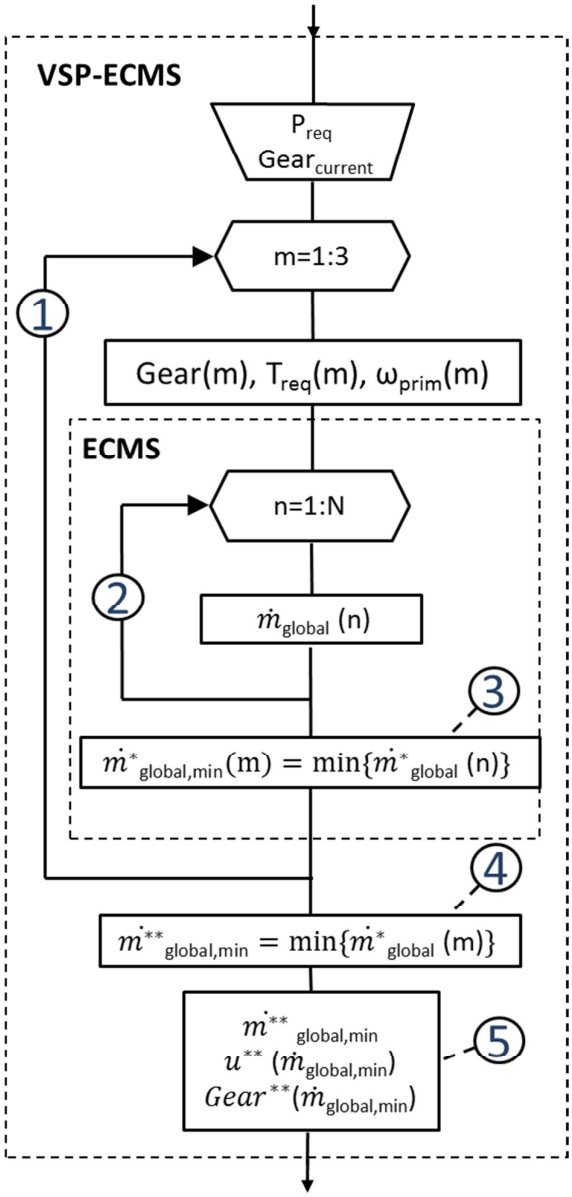

Figure 3.2.1 VSP-ECMS algorithm 1) top level iteration for previous, current and successive gears 2)ECMS iterations with search resolution n 3)Determination of minimal function cost for selected gear 4) Determination of minimal value of minimal function cost for 3 previous, current and successive gear 5) power split factor and gear output that will yield minimal global function cost

Input to the VSP-ECMS algorithm is required cycle power from the hybrid powertrain (both engine and hybrid part) and can be given as:

$$P_{req} = T_{req} \cdot \omega_{req} \qquad (3.2.1)$$

In the first step, having in mind vehicle speed and transmission ratio data, required engine speed and torque is determined with respect to the previous and successive gears as:

$$P_{req} = \begin{cases} T_{req,i-1} \cdot \omega_{req,i-1} \\ T_{req,i} \cdot \omega_{req,i} \\ T_{req,i+1} \cdot \omega_{req,i+1} \end{cases} \qquad (3.2.2)$$

Where i represents current gear.

Figure 3.2.1 position 2 represents three consecutive iterations that correspond to gears i, $i-1$ and $i+1$.

Optimal case is determined as the case with minimal global function cost as:

$$\dot{m}^{**}_{global,min} = min\{\dot{m}^{*}_{global}(m)\} \qquad (3.2.3)$$

Once the $\dot{m}^{**}_{global,min}$ is determined (Figure 3.2.1 position 4), corresponding power-split factor and suggested gear is extracted from the algorithm and forwarded as an output (Figure 3.2.1 position 5).

Position 2 and 3 in Figure 3.2.1 represent ECMS search loop as was described in previous chapter.

Several constraints have been introduces into the VSP-ECMS algorithm in order to provide correct functioning of the powertrain.

Gear shift Delay – VSP-ECMS algorithm introduces instantaneous minimization of the global function cost (both engine and hybrid part cost) in discrete time intervals (10 ms interval was selected for all simulations). In extreme cases the algorithm might instruct vehicle Transmission Control Unit (TCU) to perform very frequent gearshifts which would be clearly unacceptable. In order to avoid this behavior, gear shift delay block was added that limited minimal gear duration to 2 seconds, after which the strategy was allowed again to perform gearshift.

Minimal and maximal engine speed threshold –in order to avoid gear selection that would result with too high or too low engine speed both upper and lower engine speed thresholds were added as constraints. The lower threshold was set to 110 rad/s and upper threshold was set to 400 rad/s. If the suggested gear is beyond defined speed threshold, the proposed gear will not be inserted.

3.3 EXAMPLE OF VSP-ECMS OPERATION

Following chapter represents example of VSP-ECMS operation for a Hybrid Electric Vehicle during NEDC cycle. The results are referred to one arbitrarily selected operating point that has the following parameters:

- Requested torque from the system (at primary AMT shaft) 104.6 Nm
- Requested primary shaft speed (with respect current gear) 234.8 rad/s
- Current gear 5th
- Simulation time 978.5 s

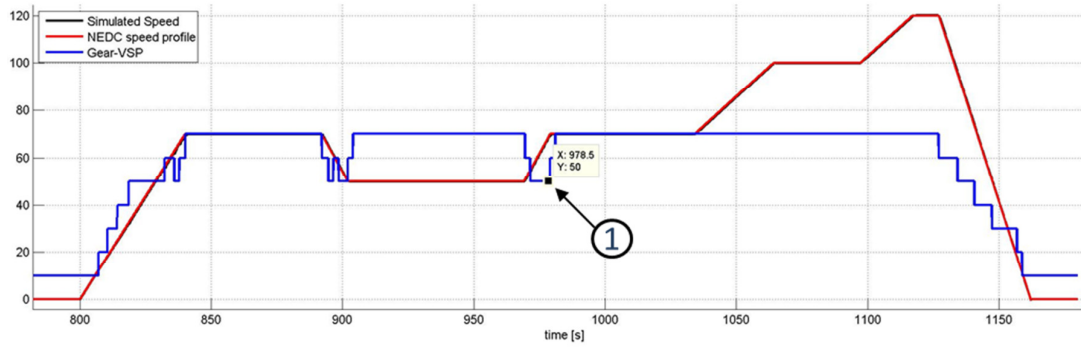

Figure 3.3.1 Simulated vehicle speed and Optimized Gearshift patent during EUDC cycle.

Figure 3.3.1 represents simulated vehicle speed profile and optimized gearshift pattern during extra urban cycle (EUDC) and position 1 gives investigated point.

As can be seen from Figures 3.3.2-3.3.5, VSP-ECMS performs three consecutive iterations over 3 gears where n=2 represents iteration for the current gear.

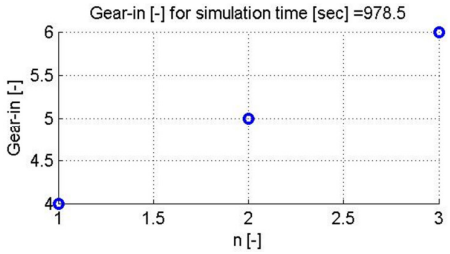

Figure 3.3.2 Investigated gears (4th, 5th and 6th)

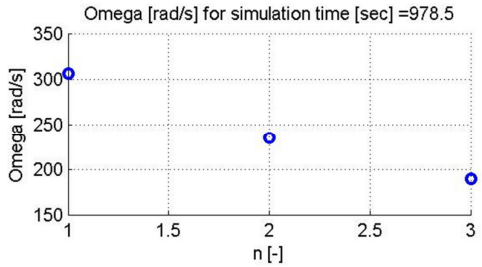

Figure 3.3.3 Primary AMT shaft speeds with respect to the gear iterations

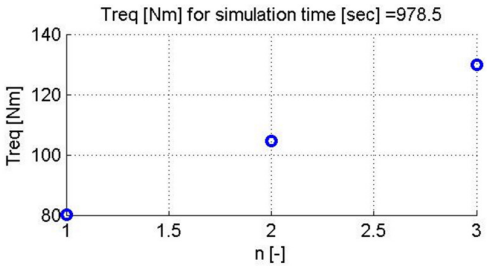

Figure 3.3.4 Torques at the primary AMT shaft with respect to the gear iterations

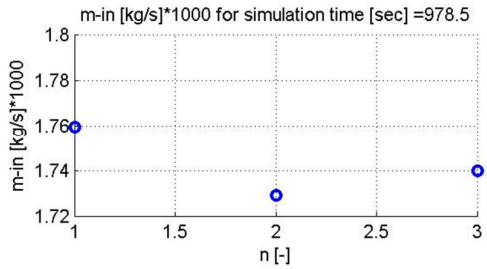

Figure 3.3.5 Minimal global energy cost with respect to the gear iterations

On the basis of the same requested power, algorithm determines requested torque (Figure 3.3.4) and requested shaft speed (Figure 3.3.3) for current, previous and successive gears as defined by Equation (3.2.2). Figure 3.3.5 and 3.3.6 represent corresponding global (minimal) function cost and power split factor for all three cases.

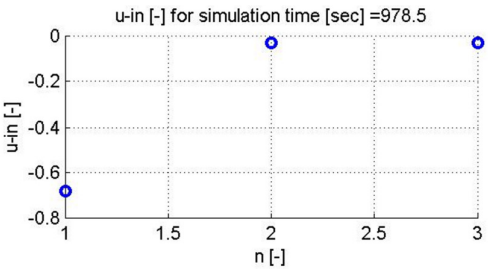

Figure 3.3.6 Power-split factor with respect to the gear iterations

On the basis of the Figure 3.3.5, minimal global function cost is found for the second iteration (i.e. current gear) and as a result, the gear will remain the same in the next simulation step.

Following figures represent trends of the Hybrid (in this case electric) function cost (Figure 3.3.7) and engine function costs (Figure 3.3.8) in the investigated simulation step for three different gears and in function of power split factor.

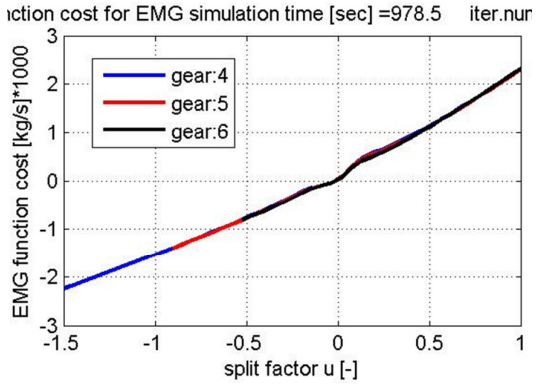

Figure 3.3.7 – Electric motor generator cost function during gear search

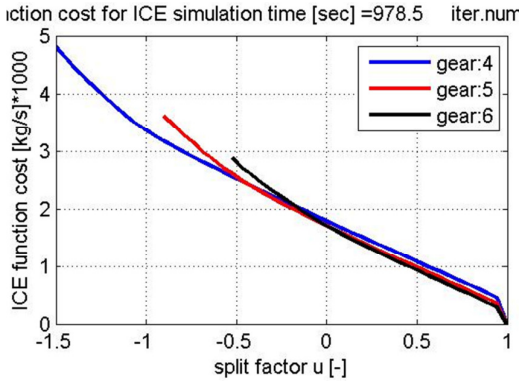

Figure 3.3.8-Internal combustion engine cost function during gear search

As can be seen from figure 3.3.8, insertion of higher gear in the examined point would lead to increase of requested (cycle) torque and decrease of the recharging capability of the engine.

$$u_{gear\ 4} < u_{gear\ 5} < u_{gear\ 6} \qquad (3.3.1)$$

Global function cost of the system for all three gears can be seen in Figure 3.3.9.

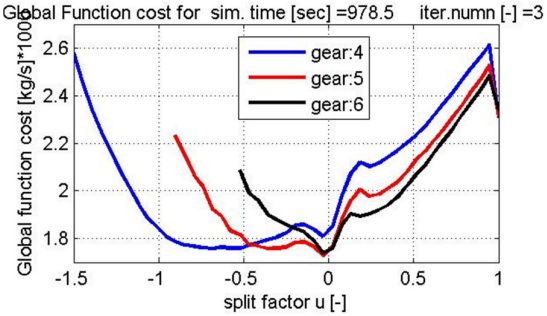

Figure 3.3.9 - Global cost functions during gear search

Result in this chapter represents only the example of the behavior of the VSP-ECMS algorithm during cycle operation. Detailed analysis was carried out for one specific Hybrid Solution (Hybrid Electric Vehicle – Case 1) in order to understand the advantage of the VSP-ECMS over standard ECMS algorithm and is presented in the following chapters.

4. HYBRID ELECTRIC VEHICLE (HEV)

4.1 ELECTRIC & HYBRID ELECTRIC VEHICLES – HISTORICAL OVERVIEW

As strange as it may seem, at the beginning of the 20th century the internal combustion engine did not dominate automotive market as it is the case today. The motorized transportation marketplace had much more versatility and was equally divided between gasoline powered vehicles, electric vehicles, hybrid electric vehicles and even steam powered vehicles.

In 1839 a Scotish inventor Robert Anderson [31] developed the first electric-powered car. Some decades later (1870), Sir David Solomon developed electric vehicle that had a light electric motor and very heavy battery [21].

At the beginning of the 20th century a number of inventors continued to develop an alternatively driven horseless carriage using electricity as a newly discovered power source. In the first decade of 20th century, electric vehicle market continued to develop rapidly and only in 1900 the American car companies made 1,681 steam, 1,575 electric and 936 gasoline vehicles [21]. According to another source, electric vehicles had a competitive share of the market and by 1904 one-third of the vehicles in New York, Chicago and Boston were purely electric [20].

Electric Vehicle Company and Baker Electrics [31] from Cleveland, Ohio were leading car producers on the market. The Electric Vehicle Company led the race to place electric taxi vehicles to the streets of major American cities. The Baker Motor-Vehicles Company specialized among others on vehicles for commercial market.

In 1900 Ferdinand Porsche, while employed at Lohner Coach Factory presented at the Paris World Exhibition a front wheel drive vehicle with a purely electrically driven wheel hub motor. Soon after followed the world's first serial hybrid electric vehicle (HEV) The Lohner-Porsche Mixte Hybrid, which used a petrol engine rotating at a constant speed to drive a dynamo, which charged a bank of accumulators. The accumulators fed current to the electric motors located in the front wheel hubs. And just shortly thereafter, Ferdinand Porsche introduced all-wheel-drive technology and the four-wheel brake system into the world of automobile production

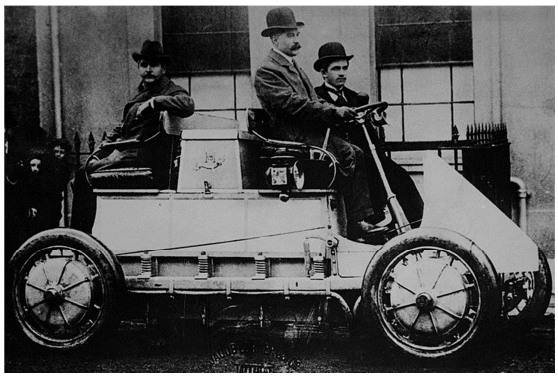

Figure 4.1.1 -The Lohner-Porsche Mixte Hybrid [31]

In 1905 H. Piper patented an electric hybrid vehicle. The vehicle used an electric motor in order to assist an internal-combustion engine during accelerations and higher speeds.

In 1915 the Woods Motor Company from Chicago presented Dual Power Vehicle [31, 21]. Unlike the Porsche's Serial HEV it had a parallel hybrid electric configuration with 4 cylinders, 12 HP internal combustion engine that was used to augment the operation of electric drive train for vehicle speeds above 25 km/h.

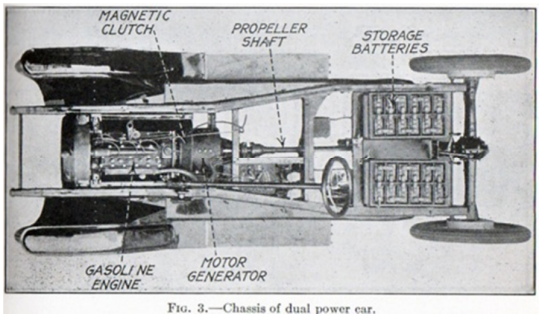

Fig. 3.—Chassis of dual power car.

Figure 4.1.2 - Dual Power Vehicle (1915-1918) by Woods Motor Company (Chicago, USA)

Internal combustion engine was used to recharge the batteries at speeds over 10 km/h but the batteries could also be recharged by regenerative braking. However, The Dual Power Car was too expensive, slow and had maintenance issues so it didn't achieve substantial commercial success.

R.M. Owen & Company of New York produced "Owen Magnetic Model 60 Touring" between 1915 and 1922. It was a full serial hybrid electric vehicle, that used 6 cylinder gasoline engine in order to run the generator that supplies electric power to the rear wheel-mounted electric motors.

Electric vehicles and electric hybrid vehicles production suffered serious decline by 1920. Development of the electric starter systems that removed the need for cranking to start-up the engine, development of the refueling infrastructure, low gasoline prices and above all longer driving range shifted the balance of power in the direction of internal combustion engines. Improvement in engine noise and emissions as well as Henry Ford's assembly line that led to decrease in production prices of vehicle powered by internal combustion engines determined the fate of electric and hybrid electric vehicles for the decades to come.

After the 1920's for the next several decades electric and hybrid electric vehicles (HEV's) were not mass produced. Hybrid vehicles piqued the curiosity only of enthusiasts, small entrepreneurs and local inventors. Since then, electric and hybrid electric vehicles were brought back in the focus whenever fossil fuel prices were increasing and growing pollution concerns were discussed. The Arab Oil crisis of the 1970's stimulated and renewed the interest of global automotive manufacturing companies for hybrid and alternative automotive technologies that would lead to fuel efficiency vehicles. The General Motors Company presented GM 512 in 1969. It was a lightweight hybrid electric vehicle that used combination of electric propulsion and a two cylinder gasoline engine [21, 22].

In 1973 Volkswagen presented its fully electric Transporter T2 that had 17kW electric motor connected to the rear wheels and was propelled by 23.8 kWh (850 kg) battery that weighed 850 kg. Soon after, VW also presented parallel hybrid electric "City taxy" that had rear mounted gasoline engine and front mounted electric motor. In 1976 VW presents first electric Golf with 20kW electric motor that served as a test platform for various electric configurations. Based on Golf platform, a volume production electric car CityStromer was presented to the market in 1981. About 100 of the models were built for energy companies in Germany [23].

In 1989 Audi presented 4WD vehicle Audi Duo, which had a front wheel drive by 2.3 liter 5 cylinder engine and an electric rear wheel drive with 12.6 HP electric motor [22].

Major milestone in hybrid electric vehicles development was the introduction of the Toyota Prius to the Japanese market in 1997. It was a full parallel-serial hybrid vehicle that had 1.5 liter in-line 4 cylinder engine that operated under Atkinson cycle and was able to produce 43 kW of power. The

powertrain also included two electric motor generators that produced 30kW and 15kW respectively and a 21kW and 1.8 kWh Nickel Metal-Hydride battery [24]. In order to couple the engine and the electric motor generators to the drivetrain the power split device was used that allowed a great deal of flexibility during operation. At any power request, the engine torque and speed could be chosen by the control strategy effectively decoupling the engine from the driveline. The powertrain operating modes included regenerative braking capability, engine on-off operation during driving and when vehicle was stopped (Start & Stop system) and pure electric driving mode. Also due to the presence of the power-split device the engine power could be sent down the mechanical path to the wheels (resembling the parallel hybrid operation) avoiding energy conversion that result in loss of efficiency [24, 25].

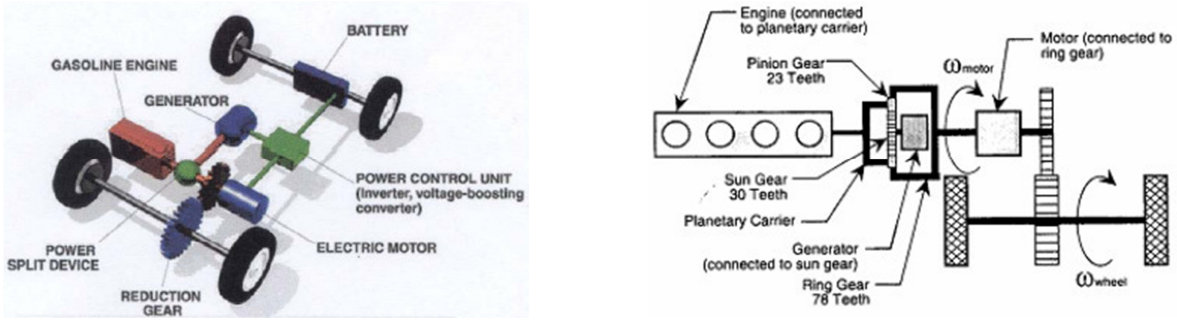

Figure 4.1.3 - The 2004 Toyota Prius Hybrid System THS-II from [25]

Several automotive companies presented electric vehicles in California including Honda's EV Plus, GM's EV1 and S-10 electric pickup, a Ford Ranger pickup, and Toyota's RAV4 EV (1997-1999). Unfortunately the programs were dropped within a few years.

Soon after the presentation of Toyota Prius, another Japanese car maker entered the market. In 1999 Honda presented to the Japanese and American market new two-door Insight, a mild parallel hybrid vehicle that featured new Honda's Integrated Motor Assist (IMA) system. The Insight was the first mass produced car in the US that won numerous awards and receives ratings of 61 mpg (3.86 lit/100km) in the city and 70 mpg (3.36 lit/100km) in the highway driving from the US Environmental Protection Agency (EPA) (1999) [31].

Figure 4.1.4 Honda Insight Powertrain layout

The Insight featured 1.0 liter 3 cylinder lean burn engine, 10 kW Motor generator (IMA) and 0.9 kWh and 10kW Nickel Metal-Hydride traction battery [24]. The IMA was positioned between engine and the transmission (Figure 4.1.4) in order to augment the engine under high load demands [24]. The systems had several benefits as regenerative braking capabilities, charging the battery (ICE load point shift) and starting and stopping the engine. Further, the engine was equipped with I-VTEC system in order to deactivate intake and exhaust valves to reduce pumping loss friction. However, fuel efficiency benefits came from engine downsizing and optimized aerodynamics and a lightweight aluminum structure of the vehicle.

Figure 4.1.5 Honda Insight engine with Integrated Motor Assist (IMA)

After the market breakthrough of the first mass produced hybrids from Toyota and Honda, almost every major automotive producer has joined the hybrid race. Many different hybrid solutions are investigated and presented to the market since the beginning of the new millennium. Also, many producers concentrate their efforts in the field of electric vehicles (Zero Emission Vehicles ZEV) and are bringing to the market interesting, environmentally friendly solutions.

Following figure represents most important milestones of Electric / Hybrid Electric Vehicles development compared to the US oil price [$/barrel] from the 1860 until 2008 [31].

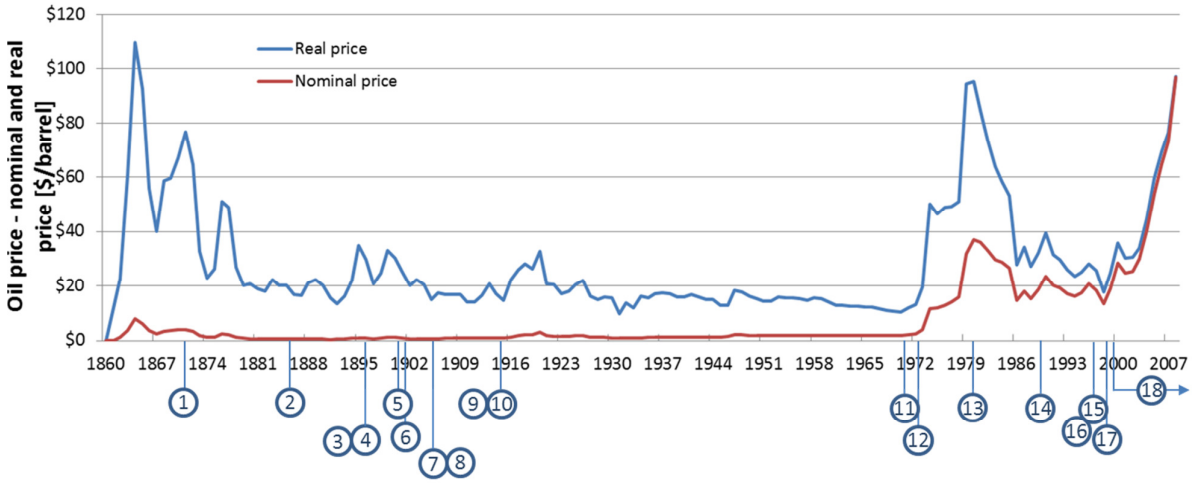

Figure 4.1.6 - US Oil price [$/barrel] from [31] and Electric / Hybrid Electric Vehicles most important milestones

Positions in Figure 4.1.6 are as follows:

1) In 1839 Robert Anderson developed the first electric-powered car. Sir David Solomon presents his electric vehicle in 1870
2) Electric-powered taxicab, using a battery with 28 cells and a small electric motor was introduced in England for the first time (1886)
3) The London Electric Cab Company began regular service using electric cars with 40-cell battery and 3 horsepower electric motor designed by Walter Bersey (1897)
4) The Pope Manufacturing Company of Hartford, Connecticut, built around 500 electric vehicles over a two-year period (1897)
5) Ferdinand Porsche developed electric carriage "System Lohner-Porsche" that appeared for the first time at 1900 Paris World Fair,
6) Ferdinand Porsche presented a 4WD series-hybrid Mixte at the 1901 Paris Auto Show,
7) H. Piper patented an electric hybrid vehicle (1905)
8) The Woods Interurban hybrid electric vehicle with interchangeable electric and engine propulsion is presented to the market (1905)
9) Woods Motor Company presented Dual Power Vehicle - a parallel hybrid electric vehicle (1915)
10) R.M. Owen & Company of New York presented “Owen Magnetic Model 60 Touring” (1915)
11) The General Motors Company presented GM 512 (1969)

12) In 1973 Volkswagen presented its fully electric Transporter T2 and parallel hybrid electric "City taxy"
13) VW presented electric car CityStromer to the market (1981)
14) Audi presents hybrid electric Audi Duo (1989)
15) Toyota Prius was introduced to the Japanese market (1997)
16) Several automotive companies presented electric vehicles in California including Honda's EV Plus, GM's EV1 and S-10 electric pickup, a Ford Ranger pickup, and Toyota's RAV4 EV (1997-1999).
17) Honda releases the first mass produced car in the US Honda Insight (1999).
18) Most major automotive producers are involved in research & development of hybrid electric and electric vehicles in order to improve fuel economy and meet the restricting CO2 emission limits.

4.2 HYBRID ELECTRIC VEHICLE (HEV) MODEL

At the end of the 20th century Japanese car manufacturers, Toyota and Honda presented to the market two hybrid electric vehicles (HEV's) that achieved substantial commercial success. Though powertrains of the both vehicles were combination of internal combustion engine and electric components (electric motor generators, batteries), there were differences regarding the level of hybridization. Toyota presented full hybrid solution with power-split system (Prius) while Honda presented mild parallel hybrid solution (Insight) with smaller size (power) electric components (electric motor/generator and batteries). Therefore goals of this work were not only to develop Hybrid Electric Vehicle model that would operate on basis of Equivalent Consumption Minimization Strategy (ECMS) and to evaluate vehicle fuel economy during different homologation cycles, but also to investigate the influence of different hybridization levels on a parallel hybrid vehicle of the same characteristics.

The hybrid electric powertrain layout that has been considered in this study is shown in Figure 4.2.1. The base vehicle is C-type passenger vehicle that has front-end transversally placed engine, 7-speed Automated Manual Transmission (AMT) and a front wheel drive. The Electric Motor-Generator (EMG) is connected directly to the primary shaft of the Automated Manual Transmission (AMT) in the parallel hybrid configuration.

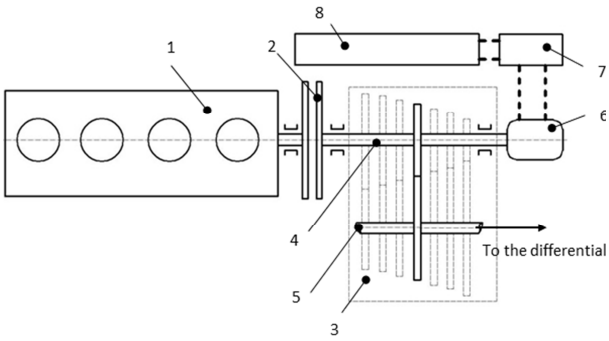

Figure 4.2.1 – HEV powertrain layout (case 1, case 2, case 3) 1-ICE 2-ICE clutch 3-Automated Manual Transmission (AMT) 4-Primary AMT shaft 5-Secondary AMT shaft 6-Electric Motor-Generator (EMG) 7-Power electronics (PE and BMS) 8-Li-Ion battery a-Power flow to the differential-front axle

This configuration offers the possibility of using either (or both) power sources (ICE and EMG) in order to provide traction, but also the possibility of recharging Li-Ion battery during traction by switching EMG functionality to generator mode. During hybrid traction (EMG only) the clutch (Figure 4.2.1 Position 2) can be opened and engine turned off in order to avoiding unnecessary friction losses. Also during braking, the engine clutch can be opened and regenerative braking can be performed by EMG, resulting in recovery of part of the vehicle kinetic energy usually dissipated into heat in conventional non-hybrid vehicles. It should be noted that regenerative braking capability is limited not only by the generator and battery maximal power capability and the State of Charge (SOC), but also by the braking force distribution between front and rear axles with respect to the vehicle deceleration.

In the case when regenerative brakes are connected only to the front wheels (as in this case) and if real world braking scenario is applied, a part of braking energy will be lost due to mechanical braking on the rear wheels. However, according to [1] if the braking deceleration is below 0.1g, in the ideal case, the braking can be performed only with regenerative brakes. Such mild decelerations correspond to all braking in ECE and almost all braking in EUDC cycle and this braking strategy has been adopted for the purpose of this work.
For the purpose of recovering maximal percentage of braking energy, the regenerative braking system should be positioned as close as possible to the wheel (as for any KERS system). In the

current configuration (Figure 4.2.1) the presence of the AMT in the energy path between wheel and EMG slightly penalizes regenerative efficiency.

For the purpose of this analysis, and considering the powertrain layout presented in the Figure 4.2.1, three separate simulations were performed regarding different HEV hybridization levels – Case 1, 2 and 3. Case 1 and 2 correspond to two realistic HEV cases already present on the automotive market, while Case 3 was added in order to perform comparative analysis of different hybrid systems (other than HEV) from the energy storage equality point of view. The HEV simulation parameters are given in the following table.

			Estimated mass [kg]
	Vehicle base mass		1470
Case 1	EMG	Hitor 50kW/440 Nm (peak)	41
		PE with booster	15.9
		Cables, connectors	8
	1.3 kWh Traction Battery	60 cell Li-Ion, V_{cell}=216 [V] m_{cell}=0.3369 [kg]	20.2
		Cables, Box, Battery Management System (BMS), Cooling	14.5
	HEV overall mass		1569.6
Case 2	EMG	Hitor 17 kW 150 Nm (peak)	22.7
		PE with booster	7.5
		Cables, connectors	8
	0.9 kWh Traction Battery	41 cell Li-Ion, V_{cell}=3.6 [V] m_{cell}=0.3369 [kg]	13.8
		Cables, Box, Battery Management System (BMS), Cooling	11.4
	HEV overall mass		1533.4
Case 3	EMG	Hitor 17 kW 150 Nm (peak)	22.7
		PE with booster	5.5
		Cables, connectors	6
	0.434* kWh Traction Battery	20 cell Li-Ion V_{cell}=3.6 [V] m_{cell}=0.3369 [kg]	6.74
		Cables, Box, Battery Management System (BMS), Cooling	8
	HEV overall mass		1519

Table 4.2.1 –Case 1, 2 and 3 HEV simulation parameters

(*) – Useful battery storage capacity of Case 3 corresponds to the energy storage capacity of the HSF and HHV cases

Electric motor generator and Li-Ion models used in order to perform the hybrid simulations were closed blocks already included inside the Library of the simulation software (VeloDyn). Therefore, existing blocks of electric components were used and the block structure will not be disclosed due to confidentiality conditions. The main electric motor generator parameters were taken from publically available data for UQM's 30 kW HiTor electric motor.

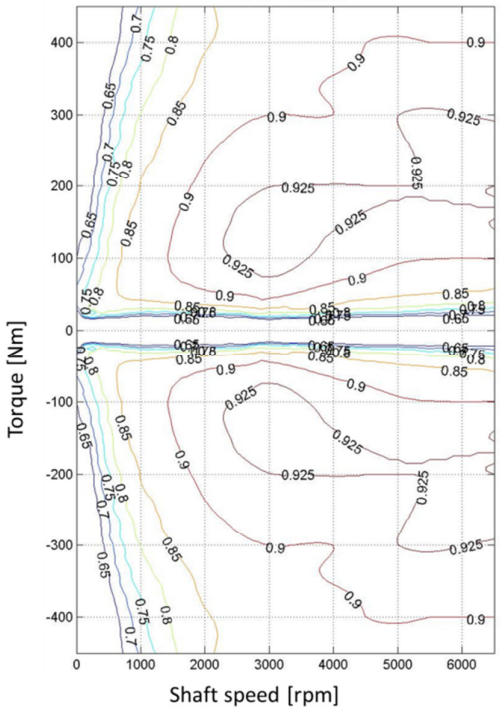

Figure 4.3.1 – Electric Motor Generator efficiency map HiTor by UQM used in the simulations [27]

Due to the absence of experimental data for different size electric motors, efficiency map for 10kW Motor Generator was created on basis of existing efficiency data from 30kW HiTor UQM motor-generator [27]. In order to carry out the scaling of the electric motor the new international standard IEC 60034-30:2008 was used.

The standard defines minimal international efficiency class of electrical machines with respect to the nominal motor power in the range from 0.75 to 375 kW and the efficiencies are divided in three classes as IE1 – standard efficiency, IE2 – high efficiency and IE3 which stands for premium efficiency.

On the basis of that considerations the scaled down machine (Table 4.3.1 – Case 2, 3) should have minimal peak efficiency of 89.45 % for IE1 class and 10kW of nominal power.

	Case 1	Case 2, 3
Rated power [kW]	30	10
peak efficiency [%]	92.50	89.45

Table 4.3.1 – Peak efficiency of 30kW HiTor and "scaled down" 10kW electric machine

Therefore correction factor that can be applied to all experimental points for 30kW HiTor machine can be determined in a simple approximation as:

$$CF = \frac{89.45}{92.50} = 0.967 \qquad (4.3.1)$$

Table 4.3.2 represent traction battery maximal discharge and charge power with respect to maximal and minimal SOC level for all three analyzed cases.

	Case 1 (1.3 kWh)		Case 2 (0.9 kWh)		Case 3 (0.434 kWh)	
	P_{dis} [kW]	P_{chg} [kW]	P_{dis} [kW]	P_{chg} [kW]	P_{dis} [kW]	P_{chg} [kW]
SOC_{max}	77.3	16	52.8	10.9	25.8	5.3
SOC_{min}	59	42.2	40.2	28.8	19.6	14

Table 4.3.2–Maximal Charge/Discharge power of three battery cases with respect to maximal/minimal SOC limits

4.4 SIMULATION RESULTS

4.4.1 NEDC CYCLE SIMULATION RESULTS

For the purpose of this analysis Hybrid Electric Vehicle simulation was performed with three different hybridization levels (Case 1, Case 2 and Case 3). All the cases refer to "full" hybrid electrical vehicle, and the pure electrical drive is allowed, but they differ from each other for different battery capacity and electric motor-generator (EMG) power (see Table 4.2.1 and 4.3.2).

The following figure represents an example of Case 1 HEV simulated speed profile over NEDC cycle, and the battery SOC trend.

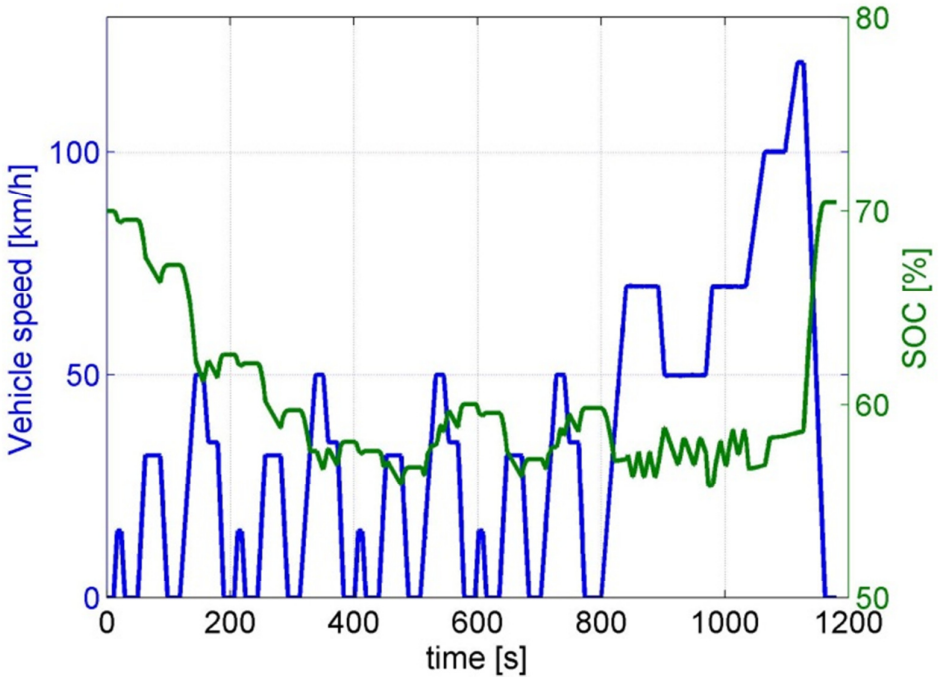

Figure 4.4.1.1 - NEDC simulated speed profile and Battery SOC trend for HEV (Case 1)

As can be observed from the Figure 4.4.1.1 control strategy operation leads to charge sustaining cycle where difference between initial and final state of charge is equal to zero ($\Delta SOC=0$). In order to evaluate fuel economy of hybrid vehicles where initial and final SOC values are not equal, correction procedure has to be applied as defined in [12]. Figures 4.4.1.2 and 4.4.1.3 represent

distribution of engine operating points over NEDC cycle. It can be observed that engine operating points have shifted to high efficiency regions (low brake specific fuel consumption values) when compared to base vehicle (Figure 2.4.3). As a result, mean engine efficiency over NEDC cycle has been increased from 0.23 for a base vehicle (Figure 2.4.4), to approximately 0.32 for all analyzed HEV cases (Figures 4.4.1.4, 4.4.1.5 and 4.4.1.6).

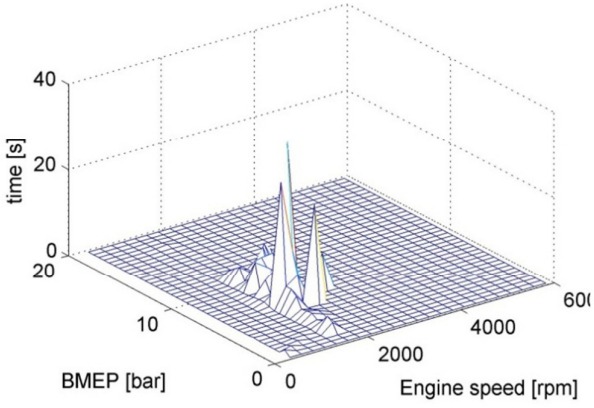

Figure 4.4.1.2- Distribution of ICE operating points (sec) during NEDC (case 1 HEV)

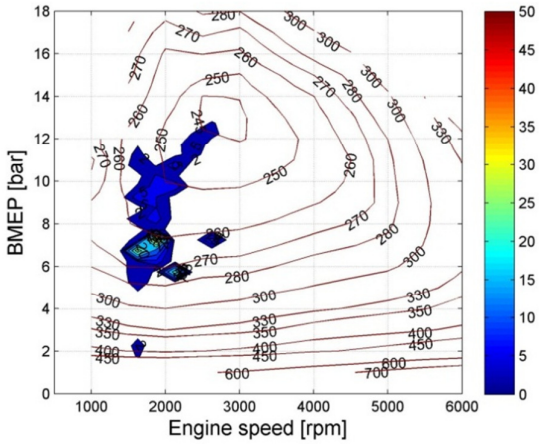

Figure 4.4.1.3- Distribution of ICE operating points (sec) during NEDC (case 1 HEV)- contour view

Following figures (4.4.1.4, 4.4.1.5 and 4.4.1.6) represent energetic analysis of HEV powertrain solutions over NEDC cycle, where all main energy fluxes can be observed. Energies represented are referred to the primary AMT axis.

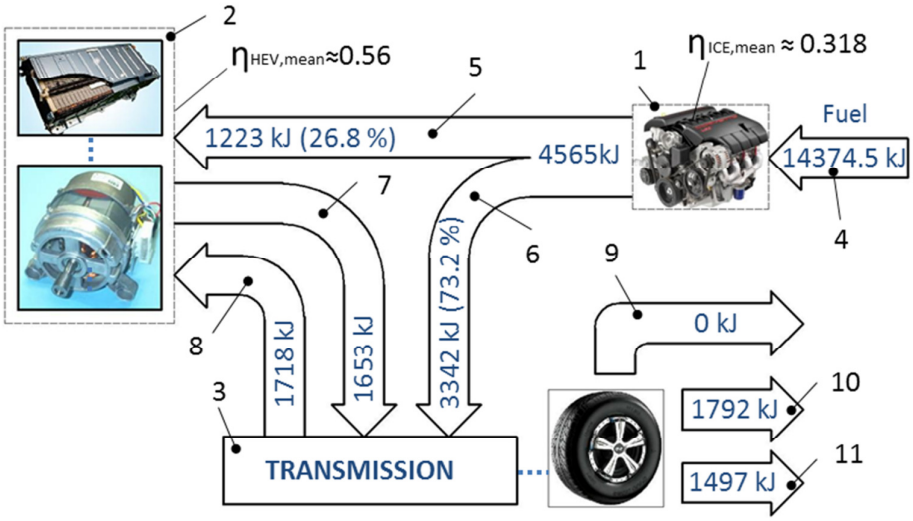

Figure 4.4.1.4 - Case 1 HEV powertrain energetic analysis for NEDC cycle (all energies are referred to the primary AMT shaft axis

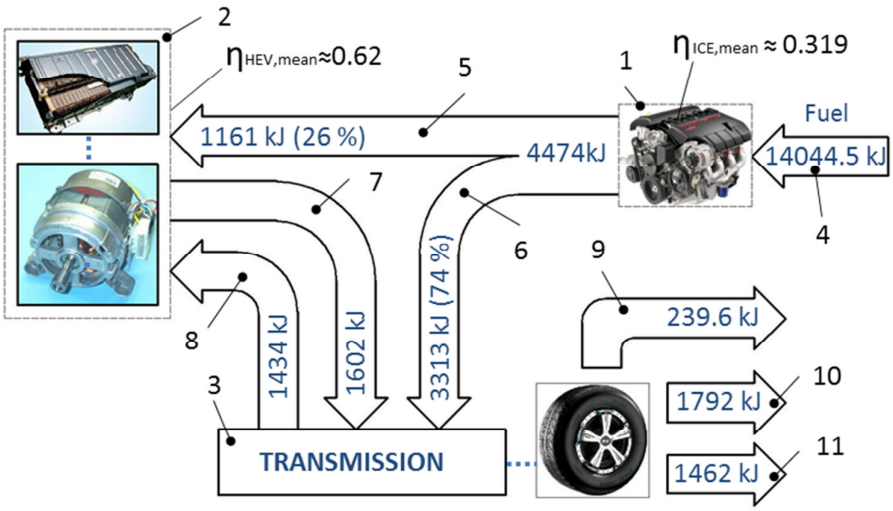

Figure 4.4.1.5 – Case 2 HEV powertrain energetic analysis for NEDC cycle (all energies are referred to the primary AMT shaft axis)

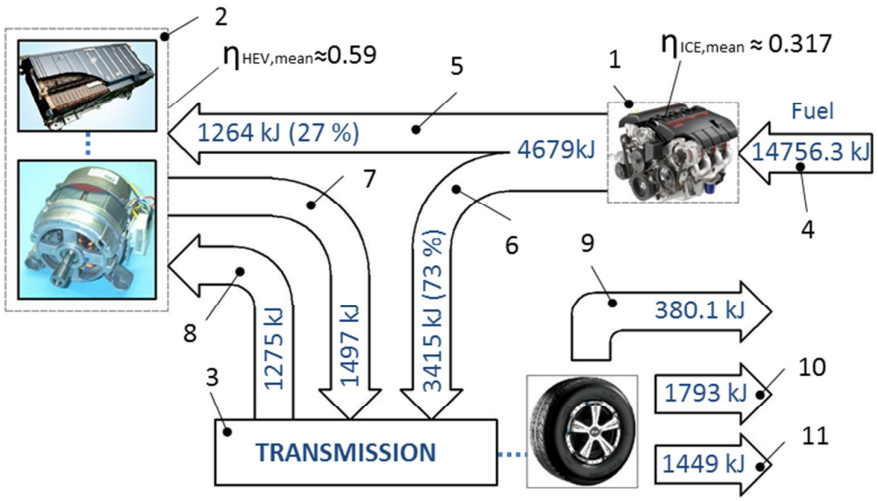

Figure 4.4.1.6 – Case 3 HEV powertrain energetic analysis for NEDC cycle (all energies are referred to the primary AMT shaft axis)

Positions in the Figures 4.4.1.4-4.4.1.6 are defined as: 1-Internal Combustion Engine 2-Hybrid powertrain part (Electric Motor Generator EMG, Li ION battery, Power electronics PE) 3- AMT transmission 4- Fuel energy consumed during the cycle 5-Direct recharging energy (from ICE to the EMG) 6-Direct traction energy (from the ICE to the transmission) 7-Hybrid electric traction energy (from the hybrid system to the transmission) 8-Regenerative braking energy (from the transmission to the hybrid system) 9-Mechanical braking energy 10-Aerodynamic resistance energy 11-Rolling resistance energy.

Mean efficiency of the hybrid part of the powertrain (Electric Motor Generator (EMG), Power Electronics (PE) and Li-Ion Battery) can be defined as:

$$\eta_{HEV,mean} = \frac{E_{OUT}}{E_{IN}} \qquad (4.4.1.1)$$

Where, E_{OUT} and E_{IN} are the energies at the output and input of the hybrid part of the powertrain respectively (in this form, equation is applicable only for the cycle that satisfies the condition $SOC_{init}=SOC_{final}$).

In general, smaller size EMG's will operate in the higher efficiency regions during the same homologation cycle which will have positive impact on the overall powertrain efficiency (Figures 4.4.1.7-4.4.1.10 represent distribution of Motor/Generator operating points during NEDC cycle for Case 1 and Cases 2).

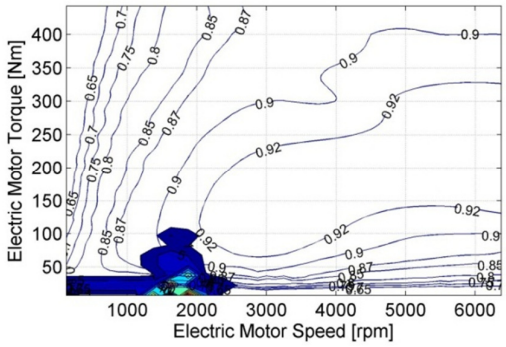

Figure 4.4.1.7 –Simulated distribution of electric motor operating points during NEDC for HEV case 1

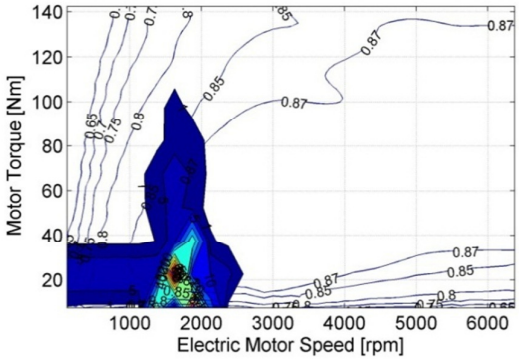

Figure 4.4.1.9 –Simulated distribution of motor operating points during NEDC for HEV case 2

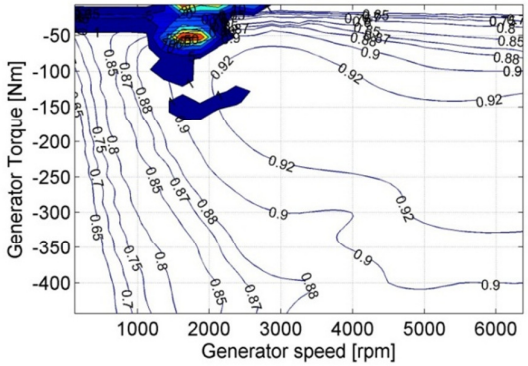

Figure 4.4.1.8 –Simulated distribution of generator operating points during NEDC for HEV case 1

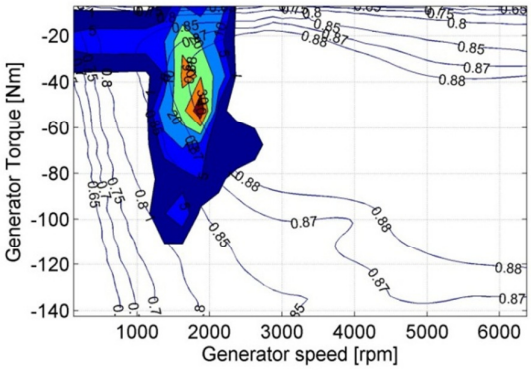

Figure 4.4.1.10–Simulated distribution of generator operating points during NEDC for HEV case 2

Also, selecting smaller EMG will negatively impact the available traction/braking power during the cycle (regenerative braking energy loss as demonstrated in the Figure 4.4.1.5-Case 2).

Battery selection is a trade-off between available power and storage capacity and the overall battery weight. Further, smaller battery power/capacity will negatively influence regenerative braking capabilities of the vehicle (as demonstrated in the Figure 4.4.1.12 – Case 3).

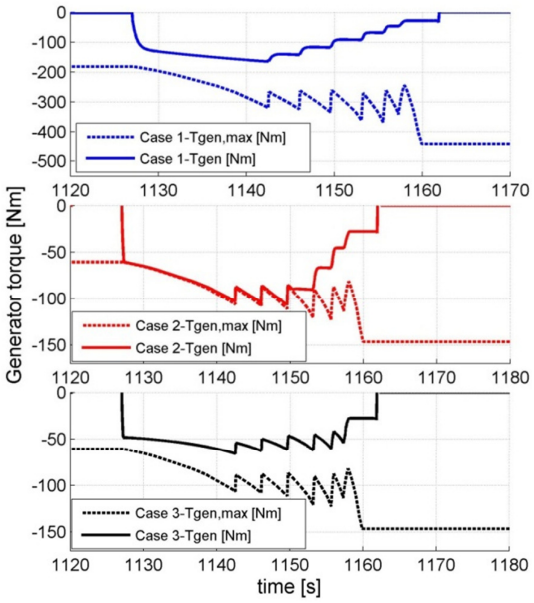

Figure 4.4.1.11 –Simulated generator (shaft) torque during EUDC braking for HEV case 1, 2 and 3

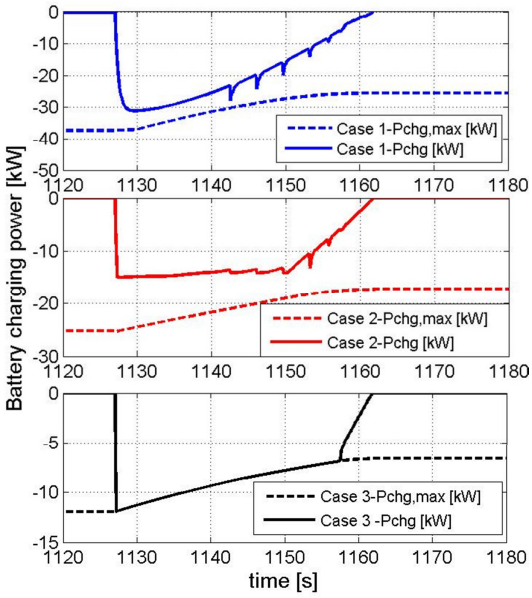

Figure 4.4.1.12–Simulated battery power during EUDC braking for HEV case 1, 2 and 3

Figure 4.4.1.13 represents simulated results of all three HEV cases during NEDC cycle. Several points can be reported: 1. in all three HEV cases, mean ICE efficiency during NEDC cycle has been increased from 0.23 (Figure 2.4.4) to above 0.3 (Figures 4.4.1.4, 4.4.1.5 and 4.4.1.6); 2. HEV Case 2 has higher Mean Hybrid efficiency with respect to the Case 1, as a result of smaller EMG (cycle based motor/generator operating points are in the higher efficiency regions). Further, Case 3 has substantial regenerative braking energy lost due to insufficient battery power capability (Figures 4.4.1.6 and 4.4.1.12).

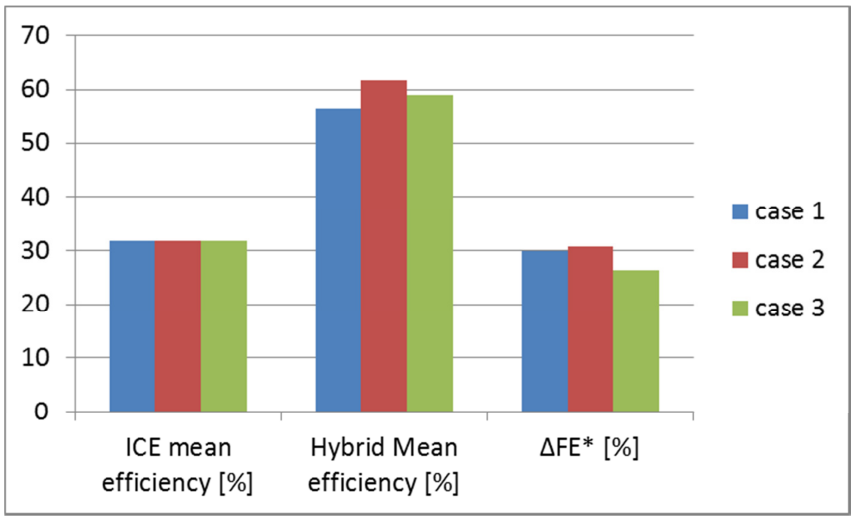

Figure 4.4.1.13– Simulated results during NEDC cycle for Case 1, Case 2 and Case 3

	ECE		EUDC		NEDC	
	FE* [lit/100km]	ΔFE* [%]	FE* [lit/100km]	ΔFE* [%]	FE* [lit/100km]	ΔFE* [%]
base vehicle	6.68	x	5.21	x	5.76	x
case 1	3.56	46.71	4.31	17.32	4.03	29.96
case 2	3.08	53.87	4.51	13.39	3.98	30.80
case 3	3.25	51.37	4.83	7.40	4.24	26.31

Table 4.4.1.1 – Simulation results for HEV (Case 1, 2 and 3)

(*) – All the results have been corrected according to ECE regulation regarding SOC balance at the end of the cycle

Figure 4.4.1.14 represents detailed energetic analysis of the hybrid part of the powertrain of the Case 1 given in Figure 4.4.1.4 position 2.

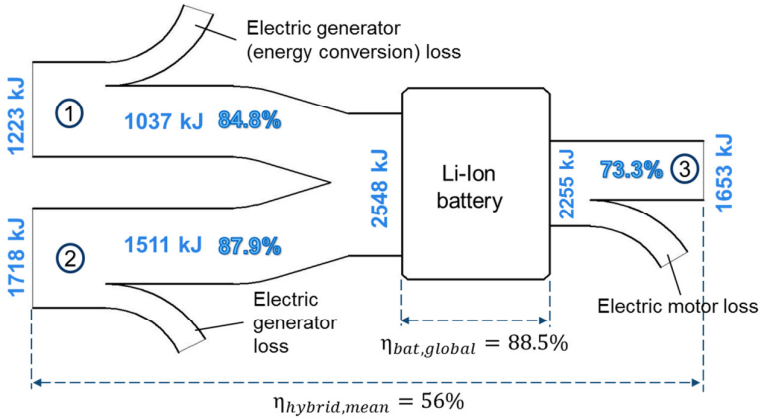

Figure 4.4.1.14–Mean NEDC cycle efficiencies of the components inside hybrid part of the powertrain (Figure 4.4.1.4 – position 2) 1- (mechanical) Recharging energy from ICE 2- (mechanical) Regenerative braking energy 3-(mechanical) HEV traction energy

Figure 4.4.1.15 represents detailed energetic analysis of the hybrid part of the powertrain of the Case 2 given in Figure 4.4.1.5 position 2.

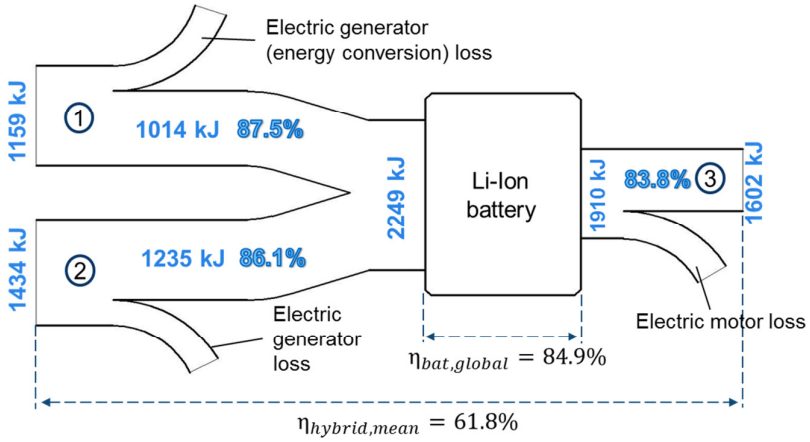

Figure 4.4.1.15–Mean NEDC cycle efficiencies of the components inside hybrid part of the powertrain (Figure 4.4.1.5 – position 2) 1- (mechanical) Recharging energy from ICE 2- (mechanical) Regenerative braking energy 3-(mechanical) HEV traction energy

After analyzing the figures 4.4.1.14 and 4.4.1.15, it can be seen that electric motor of the Case 2 operates in the zone of the higher efficiency both during regenerative braking and hybrid traction (it can be also seen graphically from the Figures 4.4.1.7-4.4.1.10). However global battery efficiency of the Case 2 is slightly lower with respect to the Case 1, as well as the generator mean efficiency. Nevertheless, higher mean electric motor efficiency during the cycle leads to higher mean cycle efficiency of the HEV Case 2 when compared to Case 1 (61.8 % when compared to 56 %).

4.4.2 VARIABLE SHIFT PATTERN (VSP)-ECMS CYCLE RESULTS

As described in the previous text (Chapters 3.2 and 3.3), VSP-ECMS algorithm was developed and implemented into supervisory Hybrid Control Unit (HCU) in order to investigate impact of the optimized (variable) shift pattern on the Hybrid Electric Vehicle fuel economy during standard homologation cycle. The VSP-ECMS control algorithm has been described in the Chapter (3.2). All presented results are based on Hybrid Electric Vehicle Case 1 during NEDC cycle, but in order to give more detailed description of the VSP-ECMS operation some results in this section are presented also for the HEV Case 2 and cycle FTP75.

Figure 4.4.2.1 and 4.4.2.2 represent battery SOC trend during NEDC cycle for HEC Case 1 that operates with Standard (STD) and Variable Shift Pattern (VSP). As it can be observed, both cycles are charge sustaining with minimal SOC variation at the beginning and end of cycle ($\Delta SOC \cong 0$).

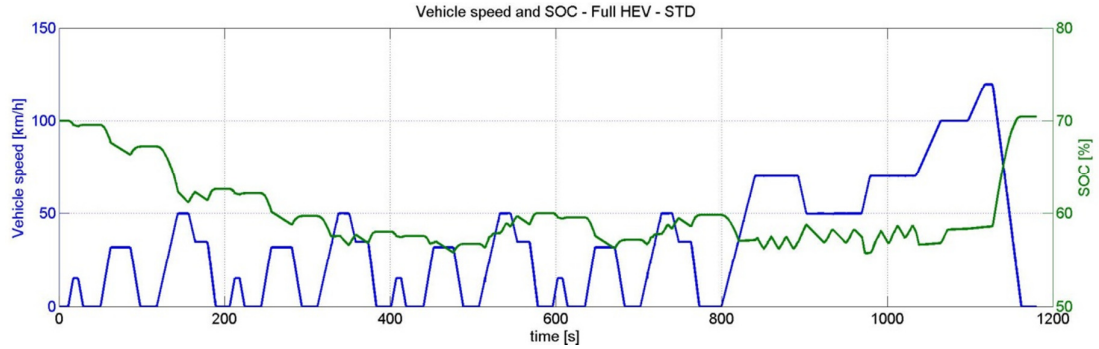

Figure 4.4.2.1 HEV Case 1– Standard Shift-pattern (STD)-ECMS

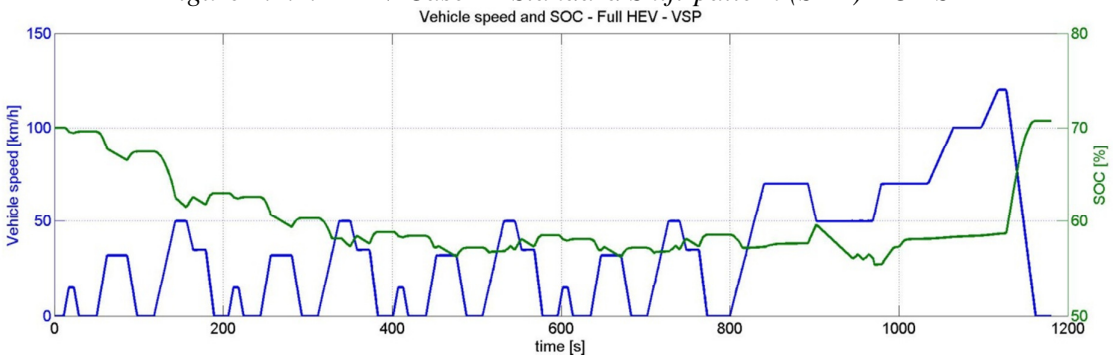

Figure 4.4.2.2 HEV Case 1– Variable Shift-pattern (VSP) - ECMS

Figure 4.4.2.3 represents comparison between standard and variable (i.e. optimized) shift pattern during NEDC cycle for HEV Case 1. It can be observed that VSP-ECMS controller tends to insert higher gears with respect to the standard shift pattern. Similar behavior of VSP-ECMS algorithm can be observed also during extract from FTP75 cycle in Figure 4.4.2.4.

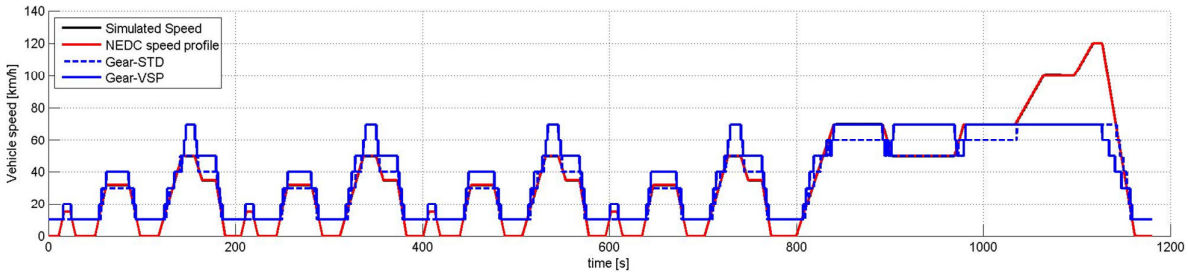

Figure 4.4.2.3 Variable Shift Pattern (VSP) Vs. Standard Shift Pattern (STD) during NEDC for HEV-Case 1- Simulated vehicle speed

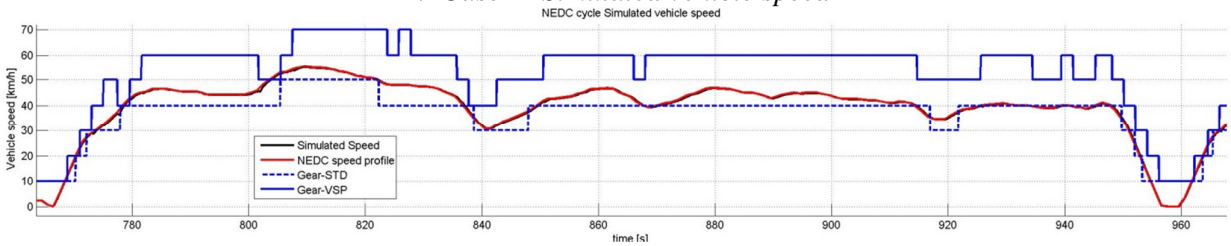

Figure 4.4.2.4 Variable Shift Pattern (VSP) Vs. Standard Shift Pattern (STD) during FTP75 cycle (HEV Case 1) - Simulated vehicle speed

As results of VSP-ECMS operation, primary AMT shaft speed (i.e. engine speed of the shaft defined in Figure 4.2.1 position 4) during the cycle is lower with respect the standard shift pattern during both NEDC and FTP75 cycles (Figures 4.4.2.5 and 4.4.2.6).

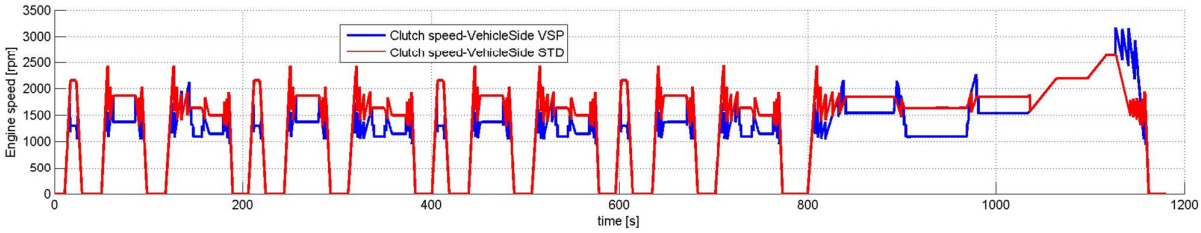

Figure 4.4.2.5 Primary AMT shaft speed (Figure 3 position 4) during NEDC for Variable Shift Pattern (VSP) Vs. Standard Shift Pattern (STD)

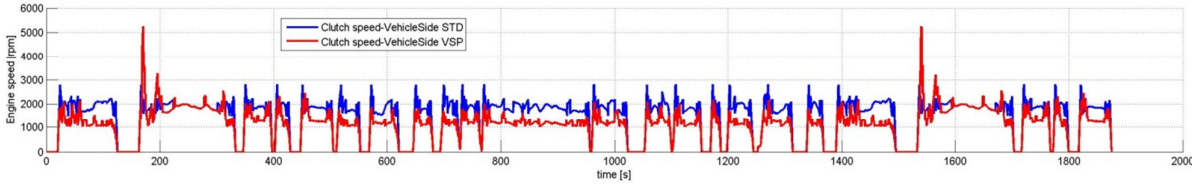

Figure 4.4.2.6 Variable Shift Pattern (VSP) Vs. Standard Shift Pattern (STD) during FTP75 cycle for HEV-Case 1

Figure 4.4.2.7 represents energetic analysis of the VSP-ECMS HEV Case 1 vehicle during NEDC cycle. If the VSP-ECMS energetic analysis is compared to STD-ECMS case (Figure 4.4.1.4) it can be observed that introduction of VSP algorithm has slightly negative effect on the mean engine (31.8% for STD and 31.15% for VSP) and mean hybrid (56% for STD and 55.6% for VSP) cycle efficiency. The quantity of regenerative braking energy remains almost the same (1718 kJ for STD and 1716 kJ for VSP). However the difference can be observed in the amount of hybrid traction energy (1653 kJ for STD and 1238 kJ for VSP) as well as the distribution of overall energy supplied by the engine. In the case of VSP vehicle, only 11.9% of total engine energy is used to recharge the hybrid system (i.e. battery) when compared to STD vehicle (26.8% used).

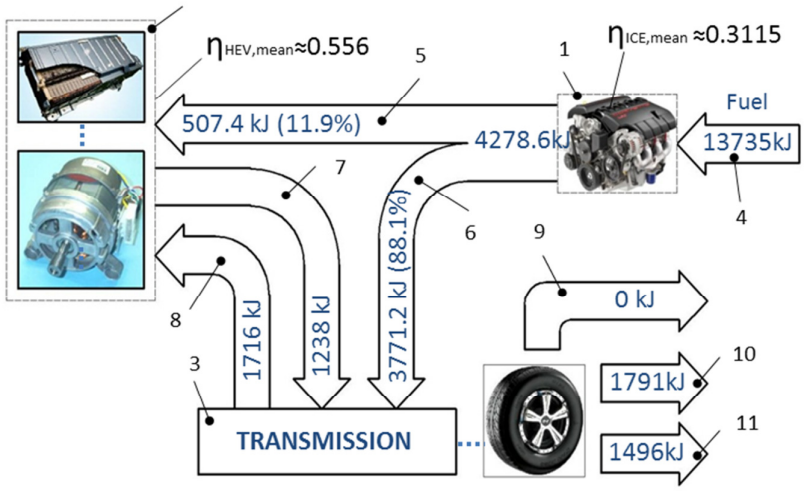

Figure 4.4.2.7 – HEV Case 1- VSP-ECMS powertrain energetic analysis for NEDC cycle (all energies are referred to the primary AMT shaft axis 1-Internal Combustion Engine 2-Hybrid powertrain part (Electric Motor Generator EMG, Li ION battery, Power electronics PE) 3- AMT transmission 4- Fuel energy consumed during the cycle 5-Direct recharging energy (from ICE to the EMG) 6-Direct traction energy (from the ICE to the transmission) 7-Hybrid electric traction energy (from the hybrid system to the transmission) 8-Regenerative braking energy (from the transmission to the hybrid system) 9-Mechanical braking energy 10-Aerodynamic resistance energy 11-Rolling resistance energy.

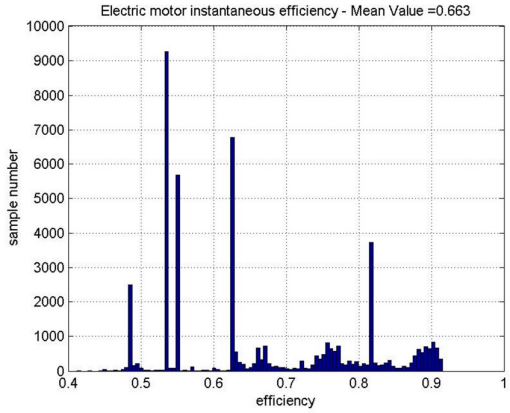

Figure 4.4.2.8 HEV Case 1 - STD E-motor instantaneous efficiency during NEDC cycle

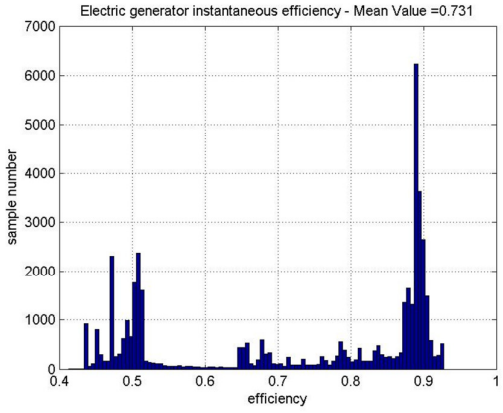

Figure 4.4.2.9 HEV Case 1 - STD Generator instantaneous efficiency during NEDC cycle

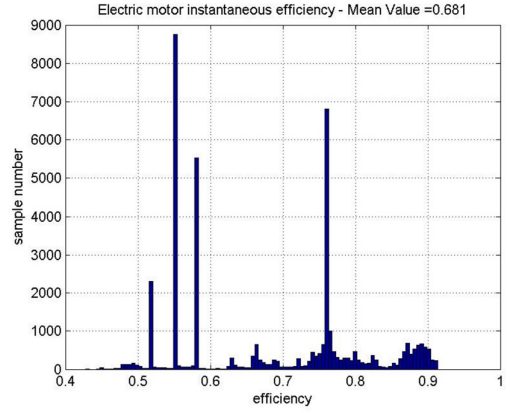

Figure 4.4.2.10 HEV Case 1 - VSP E-motor instantaneous efficiency during NEDC cycle

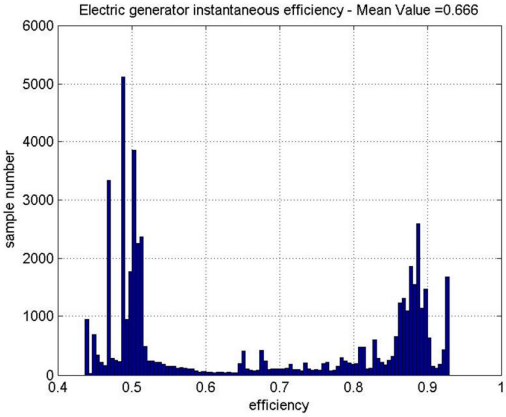

Figure 4.4.2.11 HEV Case 1-VSP Generator instantaneous efficiency during NEDC cycle

Figures 4.4.2.8 and 4.4.2.9 represent histograms of electric motor and generator efficiency during NEDC cycle with standard shift pattern, while Figures 4.4.2.10 and 4.4.2.11 represent electric motor and generator efficiency for variable shift pattern. As it can be seen, slight increase of electric motor efficiency can be observed due to the VSP operation (from 66.3% for STD to 68.1% for VSP). However substantial decrease of generator efficiency can be observed (from 73.1% for STD to 66.6% for VSP).

	ECE		EUDC		NEDC	
	FE* [lit/100km]	ΔFE* [%]	FE* [lit/100km]	ΔFE* [%]	FE* [lit/100km]	ΔFE* [%]
base vehicle	6.683	x	5.213	x	5.757	x
HEV Case 1 STD	3.56	**46.71**	4.31	**17.32**	4.03	**29.96**
HEV Case 1 VSP	3.29	**50.75**	4.17	**20.08**	3.84	**33.27**
HEV Case 2 STD	3.08	**53.87**	4.51	**13.39**	3.98	**30.80**
HEV Case 2 VSP	3.05	**54.42**	4.40	**15.65**	3.90	**32.33**

Table 4.4.2.1 – Numerical results of the STD and VSP-ECMS simulations for HEV Case 1 and 2 during NEDC cycle

(*) – All the values are corrected according to ECE directive regarding SOC

Table 4.4.2.1 represents numerical results of the STD and VSP-ECMS simulations for HEV Case 1 and 2 during NEDC cycle. All simulated fuel consumption results have been corrected for relative SOC difference in accordance with the European regulations (Method of Measuring of the Emissions of Carbon Dioxide, Fuel Consumption and the Electric Energy Consumption of Vehicles Powered by a Hybrid Electric Powertrain [12]).

	ECE	EUDC	NEDC
	ΔFE* [%]	ΔFE* [%]	ΔFE* [%]
HEV Case 1	**8.6**	**15.9**	**11**
HEV Case 2	**1**	**16.9**	**5**

Table 4.4.2.2 – Relative fuel improvement [%] over NEDC cycle with VSP-ECMS implementation

Table 4.4.2.2 represents relative fuel economy improvement [%] due to the implementation of VSP-ECMS algorithm for HEV Cases 1 and 2.

As it can be observed, VSP-ECMS leads to relative FE improvement of 8.6 % during urban cycle, 15.9 % during extra urban and 11 % during combined (NEDC) cycle for the HEV Case 1. As it was demonstrated, implementation of VSP algorithm led to the slight decrease in global hybrid and engine mean efficiency of the Case 1 vehicle (Figures 4.4.1.4 and 4.4.2.7).

However, the fuel economy improvement with VSP-ECMS algorithm can be contributed to the fact that VSP changes distribution of engine energy by lowering the percentage of energy that is used for recharging of the hybrid system. In that manner, more engine energy is “forced” down the mechanical path (Figure 4.4.1.4 and 4.4.2.7-position 6, 3771 kJ (VSP) when compared to 3342 (STD)) to the wheel. This behavior can be explained with the fact that variable gear shift pattern (VSP-ECMS) forces the engine to operate in the more efficient regions during the cycle (higher loads) while decreasing the utilization of the hybrid part (Figures 4.4.1.4 and 4.4.2.7 position 7, 1238kJ (VSP) when compared to 1653kJ (STD)) and the need to recharge the system. In this manner, energy produced by the engine is utilized for traction in the most efficiency way, without the need to suffer the energy conversions that are attributed to hybrid.

5. HIGH SPEED FLYWHEEL HYBRID VEHICLE (HSF-HV)

5.1 FLYWHEEL ENERGY STORAGE – OVERVIEW

The principle of storing energy as rotational kinetic energy inside a flywheel is a well-known concept in automotive sector. Since the very beginning, different attempts have been made in order to realize efficient flywheel energy storage system.

One amongst the first systems that appeared on the market in 1950's was the "Gyro-bus", a public transport vehicle that utilizes a high inertia flywheel as an energy storage device in order to propel the vehicle. The Gyro-bus had very limited range and needed frequent recharging stops during operation but offered an alternative solution when overhead electrification grid was not available [31].

Figure 5.1.1 – Gyro-Bus at the charging station

Figure 5.1.2 – Gyro-Bus Flywheel with Electric Motor-Generator

Unfortunately low fuel prices and high electricity prices of the period inhibited Gyro-bus to gain more important market share and to reduce manufacturing costs due to increase in sold unit numbers. Further, high inertia flywheel introduced a gyroscopic effect that resisted changes in the orientation of the vehicle, which required adaptation of the driving technique. In the recent years, technological advancements in composite materials, sealing and lubrication made possible the development of small inertial flywheels that rotate at very high speeds for different applications [29, 30, 31-39].

The idea to utilize flywheel as an energy storage device has been brought again into focus following new regulations in Formula 1 for 2009 season. Regulations allowed the implementation of the Kinetic Energy Recovery System (KERS) on board the vehicle in order to partially recover kinetic energy of the vehicle that is dissipated during frictional braking [13, 17, 29, 36]. During the race that energy could be supplied to the powertrain at driver demand (push-to-pass mode) as 60kW boost during 6.67 seconds per every lap. Regulations limited storage capacity of the system to 400kJ.

Several High Speed Flywheel concepts were proposed by different authors. Hybrid composite material flywheel with a permanent magnetic rotor attached inside the flywheel is investigated in [32]. The authors performed the structural analysis and optimization of the system in order to increase its energy density. Similar investigation was carried out in [33]. The authors describe the finite element stress and rotor dynamics analyses, along with a description of the fabrication and assembly techniques used in the construction of the rotor [33].

One interesting solution already present on the market is based on the electronically powered integral motor (carbon-fiber) flywheel. During the flywheel fabrication process a magnetic powder is mixed into the matrix composite and later on the required field configuration that forms the rotor is generated by the process of the magnetization of particles [36].

Another solution present on the market offers mechanically driven flywheel made from composite materials [29, 30]. The composite flywheel is connected to the powertrain (or directly to the wheel) by means of Continuously Variable Transmission and is able to reach very high rotational speeds ($60 \cdot 10^3$) [29].

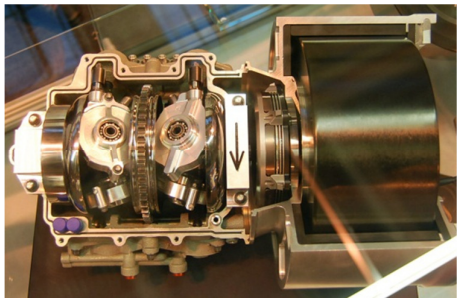

Figure 5.1.3- Mechanically driven flywheel energy storage system [29]

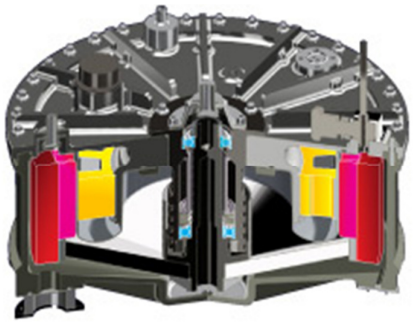

Figure 5.1.4- electrically driven flywheel energy storage system [36]

The flywheel energy storage systems have found their place also in aerospace applications. Investigations have been made into photovoltaic-flywheel power systems that could be used to replace the batteries in the spacecraft power systems [34]. The authors state that the power systems that use flywheel energy storage onboard satellites have potential of savings of 35 percent of mass, 55 percent of volume and 6.6 percent of solar array area with respect to the battery systems [34]. Other authors propose utilization of two counter-rotating flywheels for energy storage in conjunction with existing battery and power subsystem designs [35]. Also In the government sector, NASA intends to have composite flywheels in the International Space Station for energy storage [38].

5.2 FLYWHEEL ENERGY AND STRESS ANALYSIS

Utilizing HSF as energy storing device in automotive applications implies using small and light flywheels to overcome vehicle space constriction requirements and unwanted gyroscopic effects caused by rotating masses that could affect vehicle stability. Further on, low inertia flywheel needs to operate at very high angular speeds in order to be able to store significant amount of kinetic energy. As a result, materials to be used in flywheel design should be able to withstand very high stresses during operation. Kinetic energy stored in rotating flywheel can be generally determined by the following equation:

$$E_k = \frac{1}{2} J \cdot \omega^2 \qquad (5.2.1)$$

Where J is the flywheel inertia and ω is its angular velocity.
Kinetic energy of a simple reference thick-walled cylindrical tube flywheel can be evaluated as:

$$E_k = \frac{\pi \rho H (r_2^2 - r_1^2)(r_2^2 + r_1^2)}{4} \omega^2 \qquad (5.2.2)$$

Where r_1, r_2 respectively are the internal and external radii of the flywheel and H is its width.
During flywheel rotation inertial forces induce both tangential and radial stresses (Figure 5.2.1) on the flywheel material.

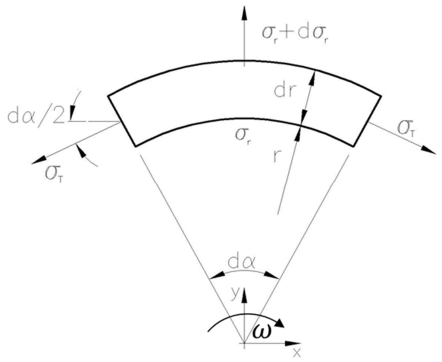

Figure 5.2.1 Radial and tangential stresses that are acting on the flywheel segment

In the case of isotropic flywheel material radial and tangential stresses that are acting on the thick-walled cylindrical tube flywheel geometry during operation can be expressed by the following equations:

$$\sigma_r = \frac{3+\nu}{8}\left(r_2^2 + r_1^2 - \frac{r_1^2 r_2^2}{r^2} - r^2\right) \cdot \rho\omega^2 \qquad (5.2.3)$$

$$\sigma_t = \frac{3+\nu}{8}\left(r_2^2 + r_1^2 + \frac{r_1^2 r_2^2}{r^2} - \frac{1+3\nu}{3+\nu} r^2\right) \cdot \rho\omega^2 \qquad (5.2.4)$$

Where ν stands for Poisson's ratio, r stands for flywheel radius and ρ is the density of the flywheel material.

Analysis of stress distribution along flywheel radius the critical stress point is considered to be at an internal flywheel radius where the failure is typically caused by tangential stress.

In the most general case, adopted flywheel material can be high strength steel or titanium, but in in order to satisfy low weight / high performance requirements, carbon-fiber composite imposes itself as the natural material of choice for high speed flywheel construction [37]. The carbon fibers are wounded in the circumferential direction giving them good resistance against tangential stress component. In the radial direction however, composite flywheels generally lack reinforcement which can be the cause for flywheel failure due to radial delamination effect [37]. Also the long term behavior of the composite flywheel is of great importance since stress and strain profiles can change with aging [37].

For safety issues flywheel has to be enclosed in the protective casing and it has to be subjected to performance and crash tests. In the case of partial or total failure of the flywheel system at high speeds, particles and debris from flywheel would have very high kinetic energy and could pose a danger to surroundings. Also in order to avoid aerodynamic losses and create excess heat inside the chamber, the flywheel has to rotate inside vacuum conditions [29, 39]. If the flywheel shaft is mechanically coupled to the rest of the driveline, special attention should be paid to sealing and lubrication components due to pressure difference between inside of the flywheel casing (vacuum) and the ambient.

Figure 5.2.2 can be used in order to graphically determine HSF kinetic energy variation with respect to the flywheel speed variation. HSF speed variation from 20k to 10k results in the kinetic energy variation of the HSF of 50kJ (Figure 5.2.2 – position a). For the same relative speed variation (of $10 \cdot 10^3$) from $60 \cdot 10^3$ to $50 \cdot 10^3$, HSF kinetic energy varies for more than 180kJ. This implies that in order to have higher available energy with respect to the same relative speed variation the operating speed of the flywheel has to be as high as possible.

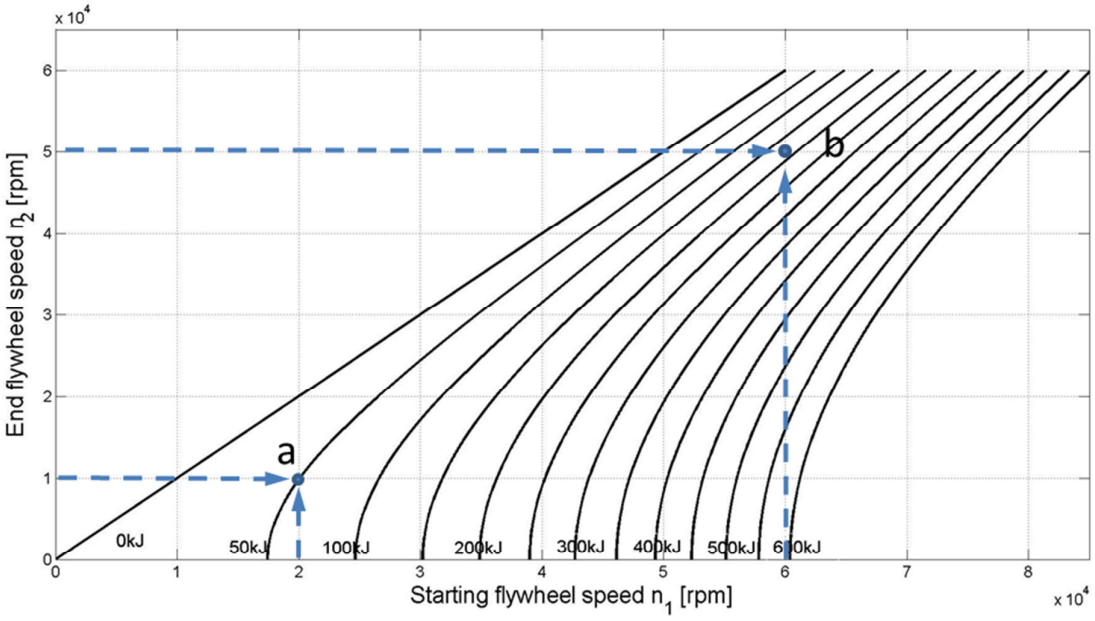

Figure 5.2.2 Flywheel kinetic energy storage capacities with respect to its speed for the flywheel inertia of 0.03 kgm^2

5.3 VEHICLE KINETIC ENERGY

Kinetic energy of the moving vehicle can be represented by a simple equation that includes kinetic energy of vehicle's both translational and rotational masses:

$$E_{k,tot} = \frac{1}{2}mv^2 + \frac{1}{2}\sum_i J_i \cdot \omega_i^2 \qquad (5.3.1)$$

Where m and v are the overall vehicle mass and speed respectively, and $\frac{1}{2}\sum_i J_i \cdot \omega_i^2$ is the overall kinetic energy of all rotational components present in the vehicle (wheels, shafts etc.). In order to obtain simple general approach in understanding the interaction between vehicle, CVT and HSF, all the considerations are done on the assumption that no losses and no external loads are acting on the vehicle and on its members.

Due to the parabolic nature of vehicle kinetic energy trend, the same overall kinetic energy change can be provided by different vehicle speed variations. Vehicle theoretical speed variation regarding a defined amount of energy that can be stored or released from the flywheel can graphically be represented in Figure 5.3.1 (it is related to single braking event).

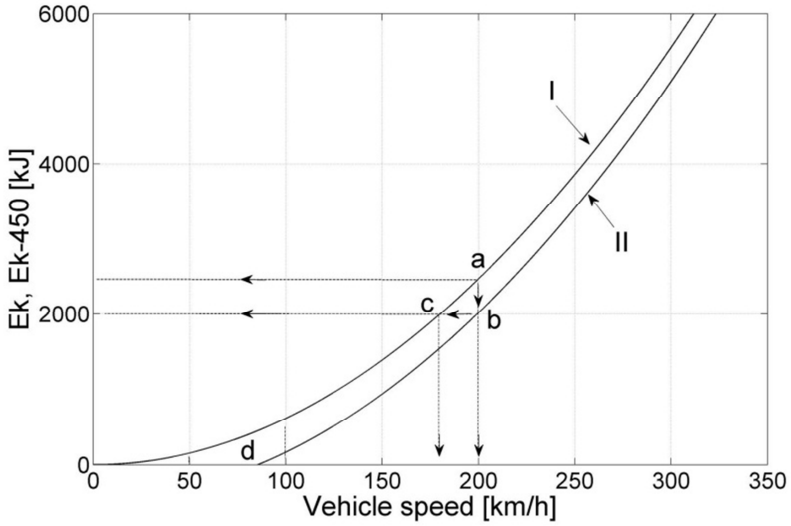

Figure 5.3.1 Vehicle kinetic energy diagram

Curve I represents vehicle kinetic energy trend related to vehicle speed (for the vehicle weight of 1600 kg). Curve II represents vehicle kinetic energy trend reduced for amount of kinetic energy that can be effectively stored in High Speed Flywheel (450 kJ). When vehicle starts regenerative braking (point a) with the vehicle running at a specified speed, the vertical line that connects curves I and II determines the maximal defined amount of energy that can be stored and remains constant for any vehicle speed. The horizontal line (from point b to point c) defines necessary vehicle speed decrease in order to provide the maximum amount of kinetic energy that is to be stored in the flywheel.

In the case of a vehicle acceleration phase with the flywheel running at its maximum speed (i.e. with 600 kJ of energy in this example) the vehicle speed at the beginning of acceleration is represented by point c. Theoretical vehicle speed increase is found moving horizontally from point c to point b and then vertically to point a. In this case it has been supposed that the IC engine

provides the energy to maintaining the vehicle speed related to point c, while the full energy recovery from the flywheel allows the vehicle to reach the speed level related to point a.

Point d represents the critical vehicle speed v_d, and if vehicle begins regenerative braking while its speed is lower than v_d, flywheel will not be fully charged, since vehicle doesn't have sufficient amount of kinetic energy.

Utilizing Figure 5.3.1, it is easy to graphically determine vehicle speed variation for defined energy amount during the flywheel charging and discharging process over whole vehicle speed range. This determined amount of kinetic energy is theoretical energy that can effectively be recovered during regenerative braking and later reapplied to the driveline. In order to create HSF Kinematic Diagram (as it will be explained later on), this energy amount is considered to be 600 kJ and it is the maximal kinetic energy that can be stored in the HSF.

5.4 HSF KINEMATIC DIAGRAM (HSF-KD)

5.4.1 HSF SYSTEM LAYOUT AND VARIANT SOLUTIONS

Objective of this work was to analyze the parallel hybrid vehicle that utilizes the high speed flywheel energy storage system. HSF system that uses mechanical connection to the driveline was selected and possible layouts were proposed and investigated. The flywheel connection to the driveline is achieved using a Continuously Variable Transmission (CVT) which acts as energy transfer device between the HSF and the driveline.

Because of the need for large transmission range between the driveline speed and the HSF speed, a "step-up" transmission (Figure 5.4.1.1 – position 10) has been added in order to allow the mechanical connection of the two systems. In order to completely decouple HSF system from vehicle driveline when necessary, a frictional clutch is added (Figure 5.4.1.1 – position 8).

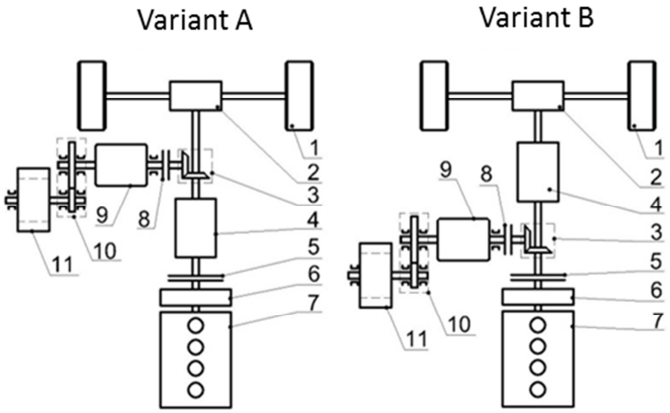

Figure 5.4.1.1 Mechanical Hybrid Vehicle Configurations 1- Wheel 2-Differential 3-"step-up" gearbox 4-AMT 5-Main clutch 6-Engine flywheel 7-ICE 8-HSF clutch 9-CVT 10-"step-up" transmission 11-HSF

Figure 5.4.1.1 shows a schematic of two possible configurations of the system and their connections to the vehicle driveline. First possibility is to connect HSF system to the secondary

gearbox shaft (Figure 5.4.1.1 - position A) that would result in input speed to the CVT being directly proportional to the vehicle speed. Other possible connection point of the HSF system would be to the primary shaft of the transmission (Figure 5.4.1.1 position B).

Comparison between solution A and B

1. **Regenerative braking** - Both variant solutions offer the possibility to perform regenerative braking of the vehicle. Variant A should provide higher efficiency of the system in braking, since gearbox (Figure 5.4.1.1 – position 4) is not included in the energy path.
2. **HSF Recharging (or ICE load point shift)** –In both cases system can be used to perform ICE load point shift when it is operating in the low load/efficiency zone. Excess energy produce by the engine, can be used to recharge the hybrid system when at low SOC values. Variant B should have more advantage since gearbox is not included in the energy path.
3. **Hybrid drive** – in both cases, engine can be shut down and disengaged from the driveline (clutch in Figure 5.4.1.1 - position 5 is opened) while HSF system can be used to provide traction to the vehicle. In this case variant A should have higher efficiency when compared to variant B, since gearbox is not included in the efficiency path.

Continuously Variable Transmission (CVT) provides continual transmission ratio change between driveline and the flywheel but its transmission range is limited [30]. CVT control provides key element in optimizing HSF system since power transferred from the vehicle driveline to HSF and back is directly related to the speed of the CVT transmission ratio variation (actuation of the CVT transmission ratio can be compared to the actuation of the throttle of the gasoline engine). The amount of energy that can be transferred per unit of time through the system impacts vehicle performance (braking and traction power on vehicle wheels).

Once the CVT transmission range reaches its limits, the utilization of the system has to be stopped without regard to the current system's State of Charge (SOC).

Main advantage of the variant B over A is the position of the gearbox between HSF system and the wheel. Though inserting gearbox in the efficiency path between HSF system and the wheel might slightly penalize the overall efficiency, advantage lies in the fact that limited CVT transmission range might be expanded by performing necessary gearshift in order to lead the input CVT shaft speed into the desired operating range (as it will be explained later on).

For the purpose of further analysis, variant B was selected (the variant A can also be considered as a particular case of the variant B, when the gearbox transmission ratio is equal to 1).

In the first approach, HSF maximal storage capacity is considered to be 600 kJ (at $60 \cdot 10^3$ rpm).

5.4.2 IDEAL ENERGY TRANSFER CHARACTERISTIC AND LUMPED INERTIA MODEL

In this chapter, main kinematic relations between HSF and drivetrain are presented and analyzed. Relations between vehicle, engine and HSF speeds for different selected gears as well as the range of the CVT transmission ratio are given graphically in the HSF Kinematic Diagram (HSF-KD). This can be useful tool in order to synthetically represent all kinematic relations in the powertrain and to guideline proper selection of HSF system parameters – CVT transmission ration, "step-up" transmission ratio and possibly to have the idea of the needed HSF inertia value.
System layout was selected as in Figure 5.4.1.1 – Variant B.

For the purpose of constructing an example of the HSF-KD, following parameters were selected:

- Vehicle mass 1600 kg
- HSF inertia 0.03 kgm^2
- Gearbox transmission ratios were taken from publicly available data for a sport car
- HSF operational range is set to be between $30 \cdot 10^3$ and $60 \cdot 10^3$ rpm

Based on equation 5.2.1, increase in flywheel rotational speed results in higher flywheel energy state. Also, flywheel maximal energy storage capacity is limited by maximum stress that flywheel material can sustain for a given rotational speed (equations 5.2.3 and 5.2.4).

The overall transmission ratio between HSF and primary AMT shaft can be expressed as:

$$\tau_{Overall} = \frac{\omega_{HSF}}{\omega_p} \qquad (5.4.2.1)$$

Overall transmission ratio can be defined as the product of the CVT transmission ratio and the transmission ratio of the "step-up" gearbox.

$$\tau_{Overall} = \tau_{CVT} \cdot \tau_{AUX} \qquad (5.4.2.2)$$

As reported previously, the "step-up" transmission is necessary to "expand" available CVT transmission ratio range in order to allow HSF, which is running at very high rotational speeds, to be coupled to the driveline.

Based on Equation (5.4.2.1), a set of constant HSF speed characteristics can be constructed. Figure 5.4.2.1 represents variation of AMT primary shaft speed (or engine speed) versus the overall transmission ratio where each characteristic corresponds to one constant value of HSF speed (and kinetic energy). Operating speed range of the HSF is set to be between $30 \cdot 10^3$ and $60 \cdot 10^3$ rpm (lines C and F in Figure 5.4.2.1). During charging and discharging process within the operating area, HSF can store or release the maximal amount of 450 kJ of kinetic energy.

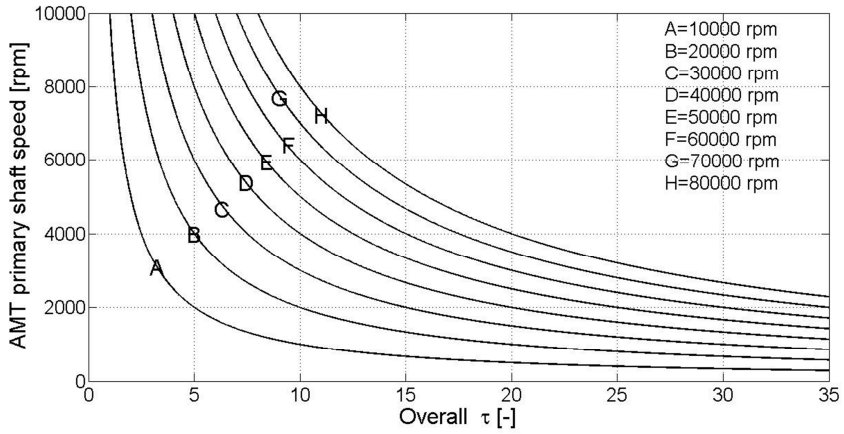

Figure 5.4.2.1 HSF constant speed characteristics

When a gear-shift is performed both AMT primary shaft engine crankshaft and input CVT shaft have to adapt their speed to the new speed of the primary AMT shaft. In the case of HSF system, speed synchronization can be performed by varying CVT transmission ratio (i.e. CVT "Tracking"), as it will be explained later on.

Figure 5.4.2.1 can be used to graphically determine overall transmission target in order to synchronize CVT and primary shaft speed.

Figure 5.4.2.2 gives graphical representation of two lumped inertias to which the system can be reduced. If all vehicle inertia is referred to the primary AMT shaft axis (Figure 5.4.2.2 – position 1) and HSF system inertia is referred to the HSF axis (Figure 5.4.2.2 – position 2), energy transfer process between HSF and the vehicle can be determined as described in the following.

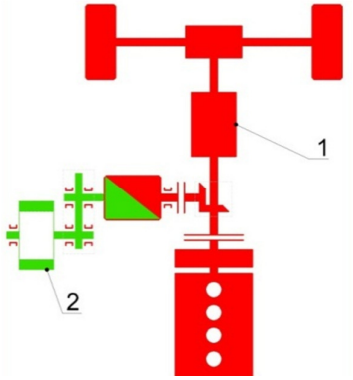

Figure 5.4.2.2 Vehicle inertia referred to primary AMT axis (1) and HSF inertia referred to HSF axis (2)

Total vehicle inertia (Figure 5.4.2.2) can be determined as:

$$J_{ref,p} = J_{cksf} + \frac{J_{transm}}{\tau_{GB}^2} + \frac{J_w}{\tau_{GB}^2 \tau_{DIFF}^2} + \frac{M_v R_w^2}{\tau_{GB}^2 \tau_{DIFF}^2} \qquad (5.4.2.3)$$

Where J_{cksf}, J_{transm}, J_w are the inertiae of the IC engine crankshaft, transmission and vehicle wheels while τ_{GB}, τ_{DIFF} stand for gearbox and differential transmission ratios.

Vehicle speed can be determined as:

$$V = R_w \cdot \omega_w \qquad (5.4.2.4)$$

Where R_w is wheel radius and ω_w is the wheel angular velocity.

In order to define the trends that describe the behavior of the system in Figure 5.4.2.1 during energy transfer operations, the ideal case (no energy losses) is considered in the following paragraphs. If the energy losses during the transfer between the vehicle and the HSF are not taken into consideration, the total kinetic energy of all the vehicle's translational and rotational masses remains constant during the transfer process, as stated by equation (5.4.2.5):

$$\sum_i E_{K_i}^{(start)} = \sum_i E_{K_i}^{(end)} = C_1 \qquad (5.4.2.5)$$

The power transfer between the flywheel and the vehicle depends only on the derivative of the flywheel kinetic energy, which is equal to an opposite variation of the total vehicle inertia kinetic energy, as stated by Eq. (5.4.2.6).

$$P_{CVT} = \left|\frac{d}{dt}\left(\frac{J_{ref,p}\omega_p^2}{2}\right)\right| = \left|-\frac{d}{dt}\left(\frac{J_{HSF}\omega_{HSF}^2}{2}\right)\right| \qquad (5.4.2.6)$$

As a consequence, the instantaneous power transfer depends on the CVT transmission ratio variation, and the energy flow (acceleration and braking of the vehicle by the HSF system) may be managed by controlling the very same parameter. The power transferred by the CVT device can in fact be determined as the time derivative of system's kinetic energy, as shown in equation (5.4.2.6):

Combining equations (5.4.2.1) and (5.4.2.6) the power transferred by the CVT device can be expressed as:

$$P_{CVT} = J_{HSF}\left(\omega_p\dot{\omega}_p\tau_{Overall}^2 + \omega_p^2\tau_{Overall}\dot{\tau}_{Overall}\right) \qquad (5.4.2.7)$$

Based on kinetic energy relations (5.4.2.5), it is possible to determine primary AMT shaft speed in relation to the inertia of the different parts of the system and overall transmission ratio.

$$\omega_p = \sqrt{\frac{2 \cdot C_1}{J_p + J_{HSF}\tau_{overall}^2}} \qquad (5.4.2.8)$$

A graphical representation of equation (5.4.2.8) is given in Figure 5.4.2.3. Trend line that connects two different constant HSF speed characteristics can be defined as energy transfer characteristic from and to the HSF. During regenerative braking for example, HSF is storing energy and as a result its speed is increasing, while at the same time referred vehicle inertia is decreasing. This process is followed by the CVT transmission ration variation (a_1 to b_2 in Figure 5.4.2.3).

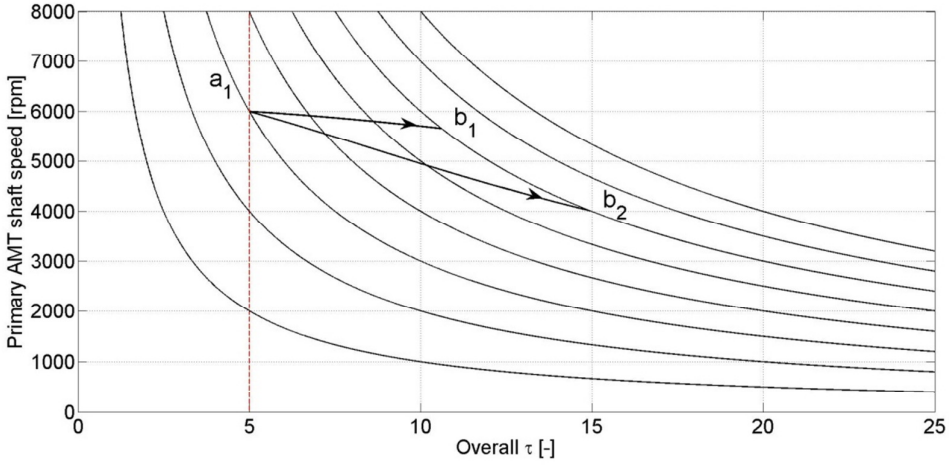

Figure 5.4.2.3 Flywheel energy transfer characteristic during regenerative braking

With respect to different values that the total vehicle inertia can assume because of different possible inserted gears (equation 5.4.2.3), the lines referred to the same energy transfer present different trends that can be drawn utilizing equation (5.4.2.8). In Figure 5.4.2.3, the line connecting points a_1 and b_1 relates to the case where vehicle total inertia is referred to the highest gear.

If the vehicle's AMT is set to the lower gear, but with the same starting primary AMT shaft speed as in the highest gear (Figure 5.4.2.3 – position a_1), for the equal energy transfer as with highest gear inserted, the energy transfer characteristics will present itself with a lower trend (Figure 5.4.2.3 – from a_1 to b_2).

Therefore, for each selected gear the referred inertia of the vehicle varies between a minimal and maximal value. As a result, the energy transfer trend with same starting point will have decreasing gradient while moving from lower to higher gears.

5.4.3 HSF-KD EXAMPLE

A graphical synthesis of the behavioral dependencies of the main components of the whole system can be represented in Figure 5.4.3.1, where different plots are linked together. The particular orientation of the plots, in order to share common axis between them, allows following the behavior of each single component (considering also its physical limits) of the whole system during an energy transfer operation between the vehicle and the HSF.

Subplot 1 in Figure 5.4.3.1 presents vehicle kinetic energy versus vehicle speed previously described in Figure 5.3.2. Subplot 2 presents the well-known vehicle transmission characteristic that evaluates primary AMT shaft speed versus vehicle speed with respect to different gears. Subplot 3 presents a set of constant HSF characteristics with respect to engine speed and overall HSF system transmission ratio change, previously explained in Figures 5.4.2.1 and 5.4.2.3. Subplot 4 in the lower right side of Figure 5.4.3.1 represents the vehicle kinetic energy variation during energy transfer (i.e. regenerative braking or acceleration) related to the overall transmission ratio variation.

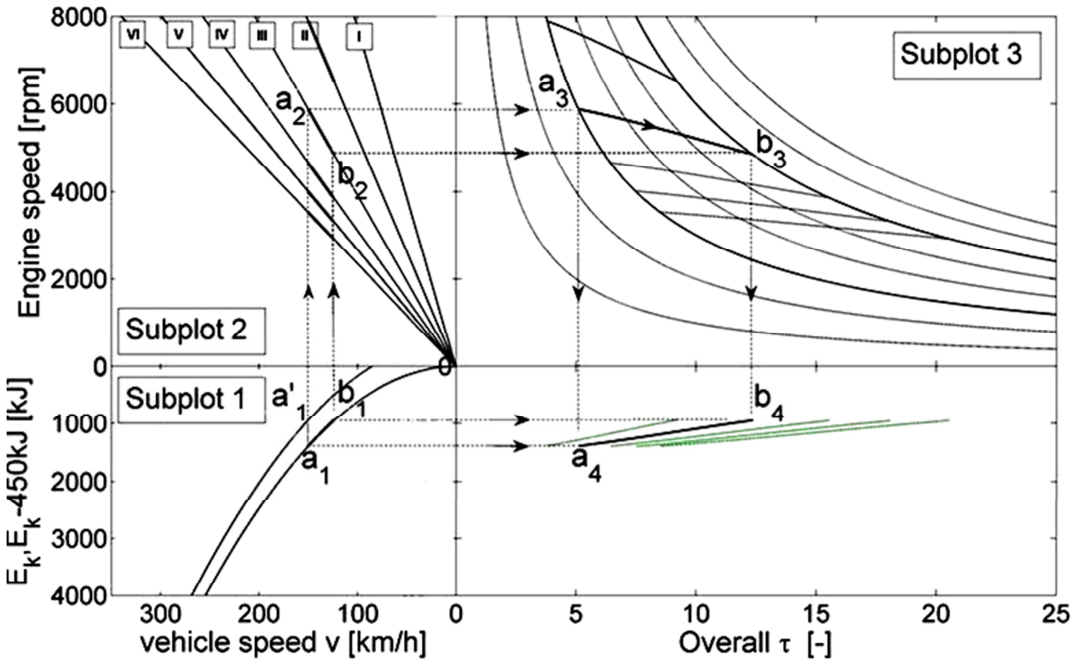

Figure 5.4.3.1 High Speed Flywheel Kinematic Diagram (HSF-KD)

Figure 5.4.3.1 gives an example of the interaction between vehicle and HSF system during one regenerative braking event in which vehicle speed is decreased for exactly the energy amount needed to fully charge the HSF. As an example, it has been considered that a regenerative braking is beginning when the vehicle speed is at 150 km/h, in third gear. The starting point in the three subplots can be located as follows: in subplot 1, knowing the vehicle speed allows to locate point a_1. Point a_2 can be located by drawing a vertical line from point a_1 to the line related to third gear in subplot 2, thus determining the primary AMT shaft speed (i.e. engine speed). As it can be observed, for the selected starting vehicle speed of 150 km/h, the possible gears for regenerative braking may vary from 2 to 6, while gear 1 is out of range for utilization (due to maximal engine speed threshold).

Drawing then a horizontal line from point a_2 to the curve related to the minimum speed ($30 \cdot 10^3$ rpm) for the HSF in subplot 3, the point a_3 can be located. This point represents HSF speed at the beginning of braking and it corresponds to total HSF energy of 150 kJ.

End of regenerative braking can be graphically determined in subplot 1 by drawing a vertical line from point a_1 to secondary kinetic energy curve at point a_1'. The difference in terms of energy between two vehicle kinetic energy curves is exactly 450 kJ for all the vehicle speeds. The horizontal line from a_1' to b_1 represents vehicle speed decrease that corresponds to vehicle kinetic energy "transfer" of 450 kJ during braking. Points b_2 and b_3 in subplots 2 and 3 represent end of regenerative braking in gear 3. In point b_3 HSF has reached its maximum speed of $60 \cdot 10^3$ rpm and has overall kinetic energy of 600 kJ. Therefore, during HSF speed increase from $30 \cdot 10^3$ to $60 \cdot 10^3$ rpm, HSF system has effectively stored 450 kJ of braking energy. Based on any energy transfer characteristic determined in previously described manner (in our case trend from a_3 to b_3), optimal overall HSF transmission ratio can be graphically determined from Subplot 3. Therefore, a proper selection of the CVT and "step-up" transmission ratio is the first step in successful coupling of vehicle-gearbox-engine-flywheel system.

5.4.4 TRANSMISSION RANGE SELECTION CRITERIA AND MAXIMAL UTILIZATION RANGE OF THE HSF SYSTEM

Overall transmission ratio (CVT and "step-up" transmission) has to be within a well specified range that depends on the mechanical limits of the system. For this reason in the following Figure 5.4.4.1 - subplot 3, two vertical lines have been introduced in order to highlight the range selection criteria for the overall transmission ratio of the system.

If during regenerative braking or accelerating event CVT reaches its transmission ratio limit, HSF has to be disconnected from the driveline and braking or acceleration should be continued using conventional frictional brakes or engine. Since it is not possible to have infinitely large transmission ratio of the CVT, it is necessary to optimize the transmission ratio range for every possible driveline configuration. Therefore, physical limits of the HSF transmission system (CVT and "step-up") dictate the operational range of the system.

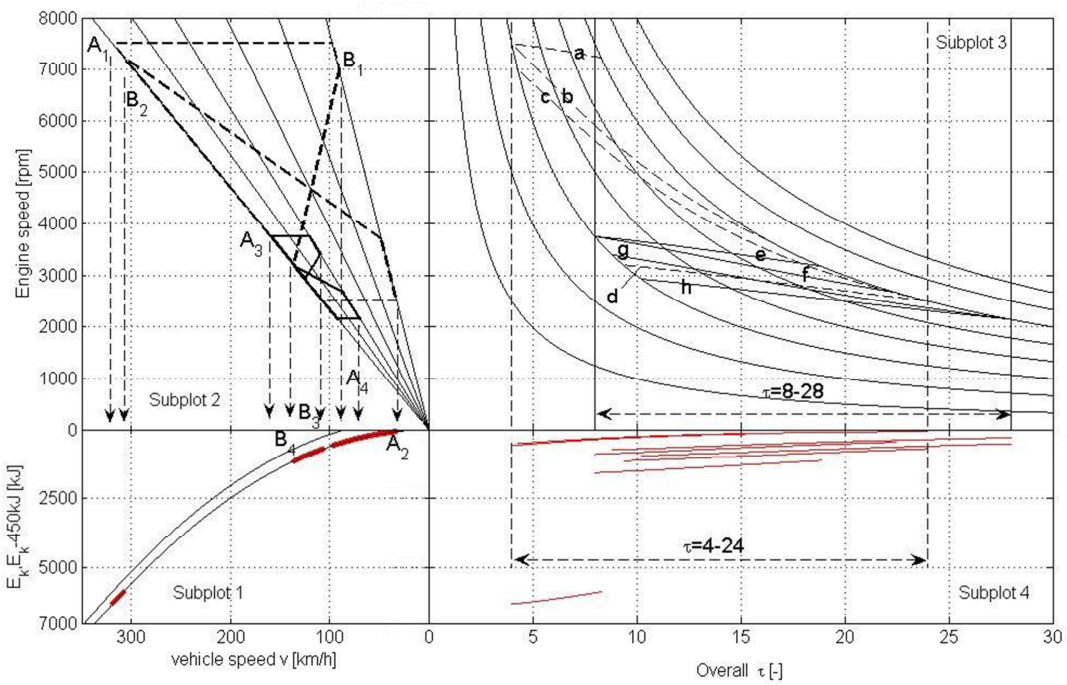

Figure 5.4.4.1 HSF-KD – effect of proper and improper selection of the overall transmission range

Maximal HSF utilization area is represented in Subplot 2 (Figure 5.4.4.1) for two different overall transmission ranges, $\tau = 4 \div 24$ and $\tau = 8 \div 28$. HSF energy transfer characteristics for both situations are given in Subplot 3. Subplot 3 presents energy transfer trends for regenerative braking or accelerating related to overall transmission range limits. If the regenerative braking starts at minimal HSF speed and overall transmission ratio from 4 to 24 in sixth gear, the two boundary energy transfer conditions can be represented with lines a and d. In the same way during vehicle acceleration in sixth gear starting from maximal HSF speed limit, the boundary energy transfer trends can be represented by lines a and d. During regenerative braking and accelerating with same conditions but in first gear energy transfer trend can be given by lines b and c in Subplot 3. Utilizing the set of curves a, b, c and d in Subplot 3, it is possible to define the maximal utilization range for regenerative braking and accelerating given in Subplot 2 (dashed line polygons) for predefined overall transmission ratio from 4 to 24. For overall transmission ratio range 8 to 28 the maximal utilization range (solid line polygons in Subplot 2) has been determined using the previously described method based on set of lines e, f, g and h in Subplot 3. During HSF operation in the first case ($\tau = 4 \div 24$) points A1 and B1 represent maximal and minimal vehicle speed

values that provide maximal utilization of the HSF system. If vehicle starts braking within A1-B1 speed range, HSF will be fully charged at the end of process. During HSF discharging process, maximal utilization area is given by points A2 and B2. If vehicle starts accelerating within speed boundaries A2-B2, all available energy stored in the HSF will be fully transferred to vehicle driveline.

For selected transmission range $\tau = 8 \div 28$ maximal HSF utilization area for regenerative braking is given by point A3 and B3 in Subplot 2. Vehicle acceleration range is given by A4-B4. Based on Figure 5.4.4.1, it can be determined that the size of maximal utilization area during vehicle braking and accelerating is defined by the overall transmission ratio. Therefore, proper selection of the transmission range is necessary to maximize efficiency of system.

Also, the vehicle should be able to utilize the HSF system both in urban driving and motorway driving conditions. If the HSF system is optimized for utilization on the motorway and HSF operating range is increased in order to provide high energy storage capacity of the HSF device, the system might suffer due to improper transmission range selection during urban driving conditions. In that case, the operational range of the HSF has to be lowered in order to maintain coupling of the HSF system to vehicle driveline (Figure 5.4.4.2). In this way HSF operating range has been lowered but at the expense of reducing maximal HSF energy storage capacity.

Therefore, same KERS configuration can be utilized in both driving scenarios, resulting in the different control settings regarding HSF operating range.

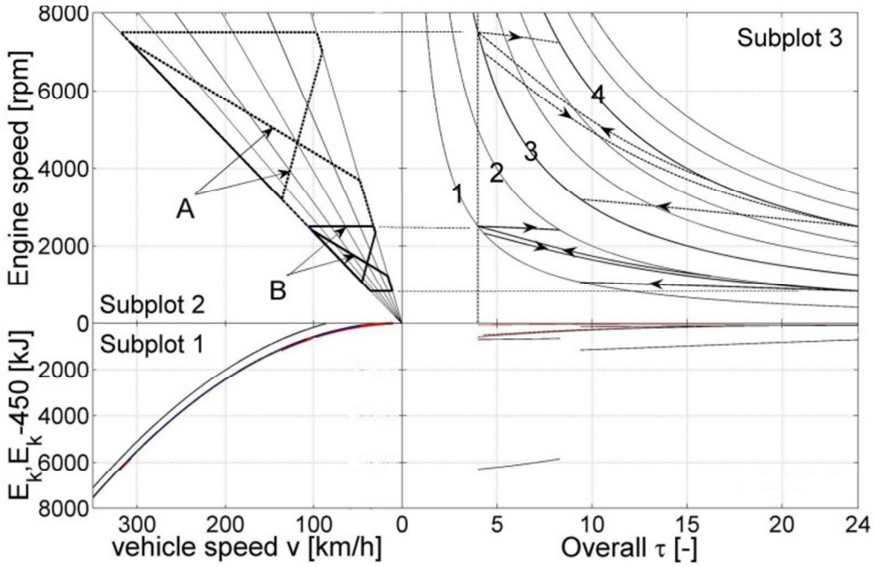

Figure 5.4.4.2 HSF-KD– HSF system utilization at urban (B) and high speed (A) driving conditions

Area A in Subplot 2 in Figure 5.4.4.2 represents maximal utilization area for regenerative braking and accelerating during high speed driving conditions. HSF operating range is between $30 \cdot 10^3$ and $60 \cdot 10^3$ rpm (lines 3 and 4 in Subplot 3). Area B in Subplot 2 represents maximal utilization area for regenerative braking and accelerating during urban driving conditions. HSF operating range is between $10 \cdot 10^3$ rpm (line 1 in Subplot 3) and $20 \cdot 10^3$ rpm (line 2 in Subplot 3).

5.5 HIGH SPEED FLYWHEEL HYBRID VEHICLE (HSF-HV) MODELING AND SIMULATION

5.5.1 VEHICLE LAYOUT AND DESCRIPTION

Quite all of the investigated HSF energy storage systems for automotive applications were generally directly coupled to the wheels or final shafts of the transmission system, having in mind mainly KERS applications and neglecting the possibility of positively influencing the internal combustion engine operation [11, 13, 14, 17 and 36]. The HSF system proposed and investigated in this work represents an original and natural evolution of the simple flywheel-based KERS system into a fully integrated hybrid HSF solution, able not only to store part of the vehicle kinetic energy during braking and release it back to the driveline when requested, but also to perform load point shift of the internal combustion engine to the area of higher efficiency.

The final layout of the hybrid HSF vehicle that has been investigated in simulation is shown in Figure 5.4.1.1– variant B and in more detail in Figure 5.5.1.1. The HSF is coupled to the driveline at the primary shaft of the AMT gearbox by frictional clutch. This layout offers the possibility to turn off ICE when suitable, and to utilize only HSF system to provide traction power (hybrid drive mode), to perform HSF recharging when required (ICE load point shift), or to provide additional power to the driveline during traction (HSF boost). During vehicle braking, when the kinetic energy of the conventional vehicle would be dissipated into heat by mechanical brakes, the HSF system can be used to recuperate and store the braking energy (the HSF system takes the role of a Kinetic Energy Recovery System (KERS)). Further, it has to be noted that since the HSF system is connected to the primary AMT shaft (and effectively only to the front axle), the braking force distribution between front and rear axle has to be taken into account. As a result, a part of braking energy may still be dissipated by vehicle brakes on the rear axle. However, for mild decelerations below 1m/s^2 it can be considered that all braking can be performed only using regenerative brakes [1]. With respect to the standard KERS application, a negative aspect of this layout is the lower HSF system efficiency during regenerative braking since AMT efficiency has to be taken into account (the ideal position of the system in order to maximize regenerative braking would be to place HSF system as close as possible to the wheels, thus minimizing mechanical losses). A simplified layout of the HSF system is given in Figure 5.5.1.1.

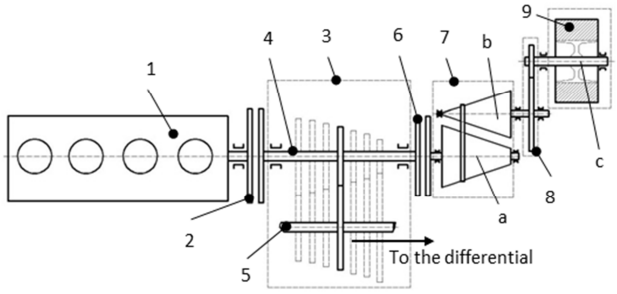

Figure 5.5.1.1 – HSF Hybrid system powertrain layout (section) 1-ICE 2-Main clutch 3-Automated Manual Transmission (AMT) 4-Primary AMT shaft 5-Secondary AMT shaft 6-HSF clutch 7-Continuously Variable Transmission (CVT) 8-"Step-up" transmission 9-High-Speed Flywheel (HSF) a-CVT input shaft b-CVT secondary shaft c-High-Speed Flywheel shaft

HSF system consists of a High Speed Flywheel (Figure 5.5.1.1 – position 9), a Continuously Variable Transmission (CVT) (Figure 5.5.1.1 – position 7), and additional transmission system (Figure 5.5.1.1 – position 8). The HSF system is connected to the driveline by frictional clutch (Figure 5.5.1.1 – position 6). CVT offers continuous transmission ratio change between driveline

and the flywheel, and it facilitates energy transfer from the driveline to the HSF and backwards, by variation of its transmission ratio. The CVT power transfer is directly related to the CVT transmission ratio and its derivative, which therefore represent a key control parameters of the system. It has to be noted that position 7 in Figure 5.5.1.1 represents only a simplified graphical representation of the CVT transmission system and not its physical model (this intuitive schematic of two conical pulleys connected by a transmission belt has been adopted just in order to provide more comprehensible explanation of the system functionality). During regenerative braking, CVT transmission ratio is controlled in order to increase HSF rotational speed and to store the energy into HSF system, while decreasing the driveline speed and resulting in vehicle deceleration. In the same way, moving CVT transmission ratio in opposite direction will result in HSF kinetic energy release, and in positive traction power provided to the vehicle. In order to couple the primary shaft and HSF that have very high speed difference, a "step-up" transmission with constant gear ratio had to be added (Figure 5.5.1.1-Position 8). The following table shows the main parameters used for the purpose of the HSF simulation.

Simulation parameters		
Flywheel		
estimated mass	[kg]	8 (including shaft)
material	[-]	Carbon-fiber
inertia	[kgm^2]	0.05
dimensions	[mm]	Ø230xØ100x100
maximal speed	[rpm]	~48000
maximal energy storage	[kJ]	625
efficiency (speed loss)	[% per min]	2-4
CVT		
Max. Power/Torque	[kW]	86 kW* / 170 Nm*
estimated mass	[kg]	14
mean efficiency	[-]	~0.9 (*)
transmission ratio	[-]	0.4-2.4
CVT shaft inertia (input/output)	[kgm^2]	0.005/0.005
"Step-up" transmission		
estimated mass	[kg]	5
efficiency	[-]	~0.95
transmission ratio	[-]	10
Overall system		
Estimated system weight	[kg]	40

Table 5.5.1.1 – HSF simulation parameters

(*) – To be confirmed with the CVT supplier

5.5.2 HSF-HV MATHEMATICAL MODEL

HSF system can be mathematically described with following equations (5.5.2.1, 5.5.2.2, 5.5.2.3) where the equations are referred to CVT input shaft (Figure 5.5.1.1-position a), secondary CVT shaft (Figure 5.5.1.1-position b) and flywheel shaft (Figure 5.5.1.1-position c) respectively.

$$J_a\dot{\omega}_a = T_6 - T_{CVTa} \qquad (5.5.2.1)$$

$$J_b\dot{\omega}_b = T_{CVTb} - T_{AUXb} \qquad (5.5.2.2)$$

$$J_c\dot{\omega}_c = T_{AUXc} - R \qquad (5.5.2.3)$$

Where T_6 is the torque through the HSF clutch, R stands for mechanical loss torque due to friction in the flywheel bearings, and it can be represented with the following equation 5.5.2.4 (it has to be noted that it is considered that the HSF is rotating in a vacuum-sealed chamber, and therefore aerodynamic losses due to very high peripheral flywheel speed ($v_{max} \cong 1150\, m/s$) are not present).

$$R = k_f\omega_c \qquad (5.5.2.4)$$

Where k_f $[Nm(rad/s)^{-1}]$ stands for friction coefficient.

Further, relations between angular velocities and accelerations of HSF shafts can be expressed in the following manner:

$$\omega_b = \tau_{CVT}\omega_a \qquad (5.5.2.5)$$

$$\dot{\omega}_b = \dot{\tau}_{CVT}\omega_a + \tau_{CVT}\dot{\omega}_a \qquad (5.5.2.6)$$

$$\omega_c = \tau_{AUX}\omega_b \qquad (5.5.2.7)$$

$$\dot{\omega}_c = \tau_{aux}\dot{\omega}_b \qquad (5.5.2.8)$$

In HSF charging mode, the torques that are acting on the HSF shafts can be defined as:

$$T_{CVTa} = \frac{T_{CVTb}\tau_{CVT}}{\eta_{CVT}} \qquad (5.5.2.9)$$

$$T_{AUXb} = \frac{T_{AUXc}\tau_{AUX}}{\eta_{AUX}} \qquad (5.5.2.10)$$

In HSF discharging mode, the torques that are acting on the HSF shafts can be defined as:

$$T_{CVTa} = \eta_{CVT}T_{CVTb}\tau_{CVT} \qquad (5.5.2.11)$$

$$T_{AUXb} = \eta_{AUX}T_{AUXc}\tau_{AUX} \qquad (5.5.2.12)$$

Where τ_{CVT} and τ_{AUX} represent transmission ratio of CVT and additional transmission (Figure 5.5.1.1 - positions 7, 8 respectively), while η_{CVT} and η_{AUX} represent their mechanical efficiencies. Based on previous equations, the torque that is acting on the primary CVT shaft can be expressed in function of $\dot{\tau}_{CVT}$ and $\dot{\omega}_a$ as follows (only in charging mode):

$$T_{CVTa} = \frac{\tau_{CVT}\dot{t}_{CVT}\omega_a}{\eta_{CVT}}\left(J_b + \frac{J_c\tau_{AUX}^2}{\eta_{AUX}}\right) + \frac{\tau_{CVT}^2\dot{\omega}_a}{\eta_{CVT}}\left(J_b + \frac{J_c\tau_{AUX}^2}{\eta_{AUX}}\right) + \frac{\tau_{CVT}}{\eta_{CVT}}\frac{R\tau_{AUX}}{\eta_{AUX}} \qquad (5.5.2.13)$$

It can be noted that incoming torque on the primary CVT shaft can be represented by three separate torques: torque due to CVT transmission ratio variation $T_{\dot{\tau}}$, HSF system acceleration torque $T_{\dot{\omega}}$, and frictional loss torque T_R.

$$T_{CVTa} = T_{\dot{\tau}} + T_{\dot{\omega}} + T_R \qquad (5.5.2.14)$$

In the case of steady state HSF operation ($\dot{\omega}_a = 0$), when the system is engaged (HSF clutch is closed) and the CVT transmission ratio remains constant ($\dot{\tau}_{CVT} = 0$), the torque transmitted from the HSF system to the primary AMT shaft consists only of mechanical loss torque *R* reduced to primary shaft (equation 5.5.2.15)

$$T_{CVTa} = \frac{\tau_{CVT}}{\eta_{CVT}}\frac{R\tau_{AUX}}{\eta_{AUX}} \qquad (5.5.2.15)$$

Based on previous considerations, HSF system layout can be simplified as shown in the following Figure 5.5.2.1, where position 1 represents referred inertia of the system to the primary CVT shaft.

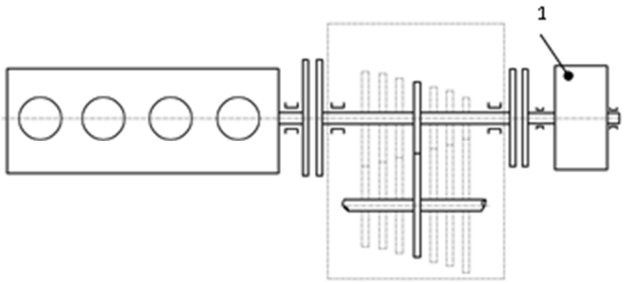

Figure 5.5.2.1 – HSF Hybrid system Powertrain simplified layout 1-Referred HSF system inertia to the primary AMT shaft axis

The main differential equation in this case can be expressed as:

$$J_{ref}\dot{\omega}_a = T_6 - \bar{T}_{CVTa} \qquad (5.5.2.16)$$

Where $\bar{T}_{CVTa} = T_{\dot{\tau}+}T_R$, and the equivalent inertia can be expressed by the following equation.

$$J_{ref} = J_a + \frac{\tau_{CVT}^2}{\eta_{CVT}}\left(J_b + \frac{J_c\tau_{AUX}^2}{\eta_{AUX}}\right) \qquad (5.5.2.17)$$

In the conditions when the system clutch (Figure 5.5.1.1-position 6) is open and the system is decoupled from the powertrain, the CVT control strategy has been developed in order the do a continuous transmission ratio change of the CVT with the objective to reach, in each time step, the following condition:

$$\omega_a = \omega_p \qquad (5.5.2.18)$$

Where ω_p is the speed of the primary AMT shaft. This maneuver can be designated as CVT "tracking". In this manner, when request for closing of the clutch is issued, the energy loss due to speed difference of the clutch plates is minimized since the speed of the primary CVT shaft is

matched to the primary AMT shaft speed. During CVT tracking, differential equation of primary CVT shaft speed in function of CVT transmission ratio variation and its speed can be expressed as:

$$A\dot{\omega}_a + B\omega_a = C \qquad (5.5.2.19)$$

Where A, B and C are given as:

$$A = J_a + \tau_{CVT}^2 \eta_{CVT}(J_b + J_c \tau_{AUX}^2 \eta_{AUX}) \qquad (5.5.2.20)$$

$$B = \dot{\tau}_{CVT}\tau_{CVT}\omega_a \eta_{CVT}(J_b + J_c \tau_{AUX}^2 \eta_{AUX}) \qquad (5.5.2.21)$$

$$C = R\tau_{AUX}\eta_{AUX}\tau_{CVT}\eta_{CVT} \qquad (5.5.2.22)$$

Dependence of the CVT and auxiliary transmission efficiencies on the direction of the energy flux from and to the flywheel have to be taken into account (as defined by equations 5.5.2.9-12) also when defining equation 5.5.2.19. Once the primary CVT shaft speed and acceleration are determined, remaining kinematic characteristics can be defined on the basis of equation (5.5.2.5-8).

Further, in order to provide smooth dynamic transition during coupling of the HSF system to the powertrain, beside speed equality condition (equation 5.5.2.18) another dynamic condition has to be satisfied as given by equation (5.5.2.23).

$$J_p\dot{\omega}_p = J_{ref}\dot{\omega}_a \qquad (5.5.2.23)$$

Where $J_p, \dot{\omega}_p$ represent the moment of inertia and the acceleration of the primary AMT shaft, while $J_{ref,}\ \dot{\omega}_a$ represent HSF-referred inertia and acceleration of the primary CVT axis.

The energy inside HSF system is stored in the form of rotational kinetic energy and it can be expressed by the following equation:

$$E_k = \frac{1}{2}J_{ref}\omega_a^2 \qquad (5.5.2.24)$$

Further, by knowing the maximum permissible flywheel rotational speed (Table 5.5.1.1), the State of Charge (SOC) of the complete HSF can be determined as:

$$SOC = \frac{E_{k,act}}{E_{k,max}} \qquad (5.5.2.25)$$

Where $E_{k,act}$ represent actual energetic content of the HSF system. Therefore, a SOC value equal to zero would suggest that HSF system is at standstill ($\omega_c = 0$), and SOC equal to one would suggest that flywheel has reached its maximum speed (5000 rad/s), and therefore its maximum energy content.

If the HSF system is considered separately from the driveline (Figure 5.5.1.1 – positions 7, 8, 9) mean efficiency of the system can be defined as:

$$\eta_{HSF,mean} = \frac{E_{OUT}}{E_{IN}} \qquad (5.5.2.26)$$

Where E_{OUT} and E_{IN} are the output and input energies to the system.

Equation (5.5.2.26) is valid only in the case when there is equality between the SOC at the beginning and the end of considered interval (ΔSOC=0). In the opposite case, mean efficiency equation can be expressed as:

$$\eta_{HSF,mean} = \frac{E_{OUT} + \Delta E_{HSF} \cdot \eta_{dis,mean}}{E_{IN}} \qquad (5.5.2.27)$$

Where $\Delta E_{HSF} = E_{HSF,Final} - E_{HSF,initial}$ the energy is difference of the storage system i.e. High Speed Flywheel at the end and the beginning of the cycle and $\eta_{dis,mean}$ is the mean discharge efficiency of the system.

5.5.3 NEDC CYCLE SIMULATION RESULTS

The following paragraphs present the main results for HSF hybrid simulation over NEDC cycle. Figure 5.5.3.1 represents simulated vehicle speed and SOC value during the cycle.

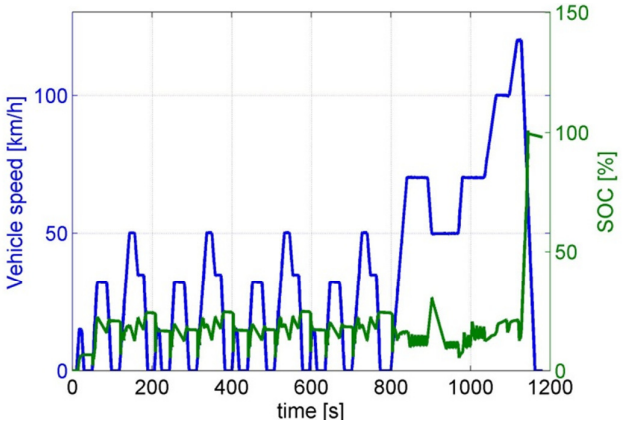

Figure 5.5.3.1 - NEDC simulated speed profile and SOC trend for HSF hybrid vehicle

Figures 5.5.3.2 and 5.5.3.3 represent distribution of engine operating points during NEDC cycle. Once again, majority of engine operating points have shifted to higher efficiency region when compared to the base vehicle.

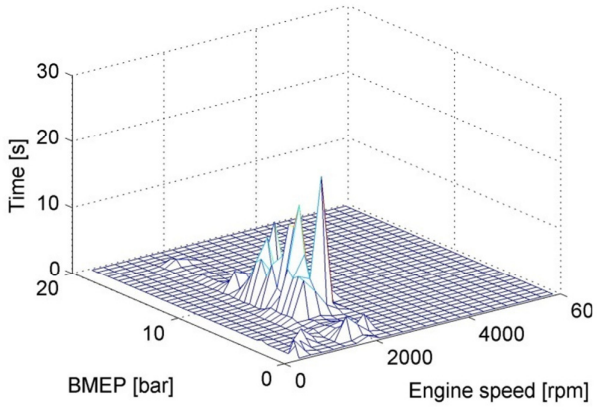

Figure 5.5.3.2- Distribution of ICE operating points (sec) during NEDC cycle

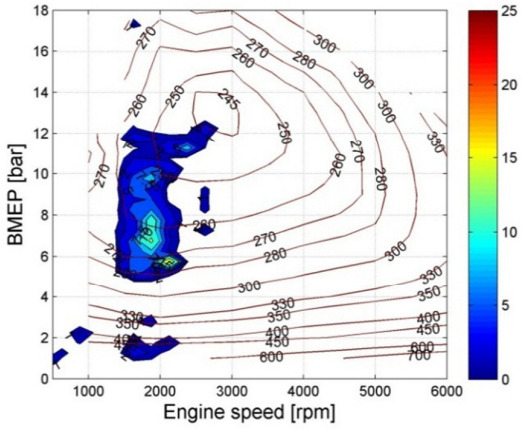

Figure 5.5.3.3 - Distribution of ICE operating points (sec) during NEDC cycle

Figure 5.5.3.4 represents CVT transmission ratio variation during the cycle.

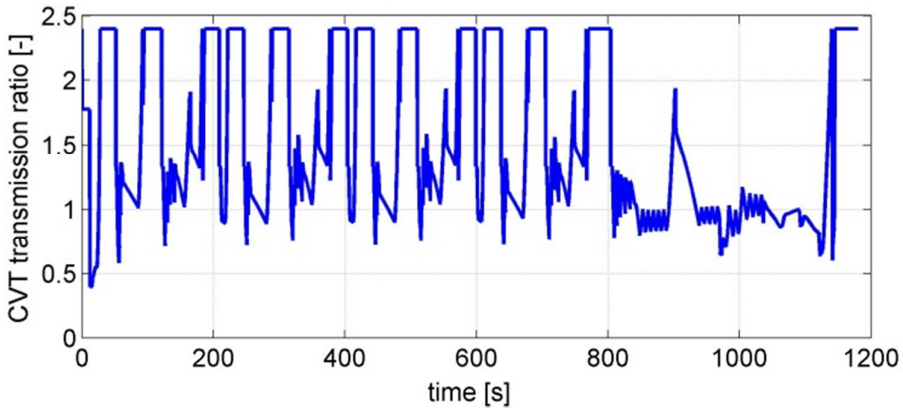

Figure 5.5.3.4 – CVT transmission ratio variation during NEDC cycle

Figure 5.5.3.5 represents energy distribution during the NEDC cycle. Even with relatively high value of the kinetic energy lost to the mechanical braking, high mean efficiency of the hybrid part of the powertrain can be observed due to high energy conversion efficiency of the system.

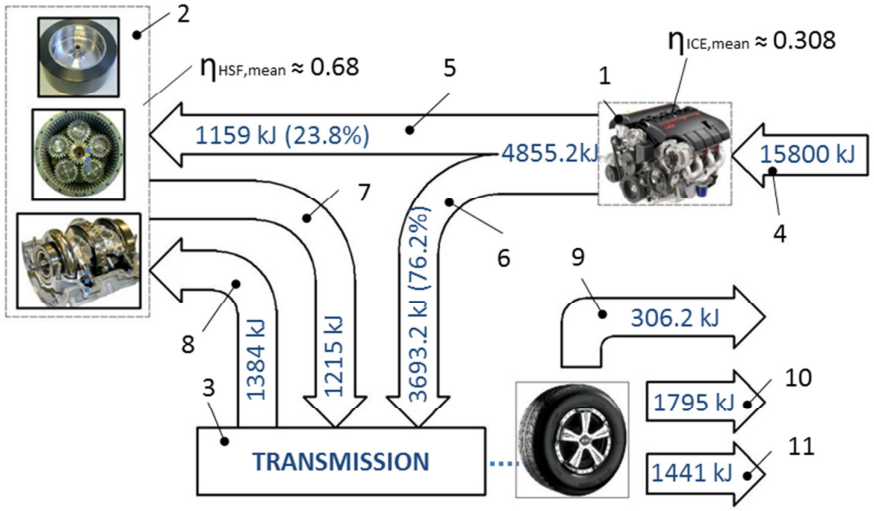

Figure 5.5.3.5 – HSF powertrain energetic analysis for NEDC cycle (all energies are referred to the primary AMT shaft axis): 1-Internal Combustion Engine 2-Hybrid powertrain part (High Speed Flywheel, CVT, additional transmission) 3- Vehicle transmission 4- Fuel energy consumed during the cycle 5-Direct recharging energy (from ICE to the HSF) 6-Direct traction energy (from the ICE to the transmission)7-Hybrid traction energy (from the hybrid system to the transmission) 8-Regenerative braking energy (from the transmission to the hybrid system)9-Mechanical braking energy 10-Aerodynamic resistance energy 11-Rolling resistance energy

It has to be noted that mean HSF efficiency calculation ($\eta_{HSF,mean}$) as ratio between output and input energies to the system is valid only in the case when SOC difference is equal at the beginning and end of the cycle ($\Delta SOC=0$). In order to define mean HSF system efficiency in the case when $\Delta SOC\neq 0$ (Equations 5.5.2.26, 5.5.2.27), the energy difference has to be added (or subtracted in the case of $\Delta SOC<0$) to the output energy value (considering also the discharge efficiency of the HSF system.

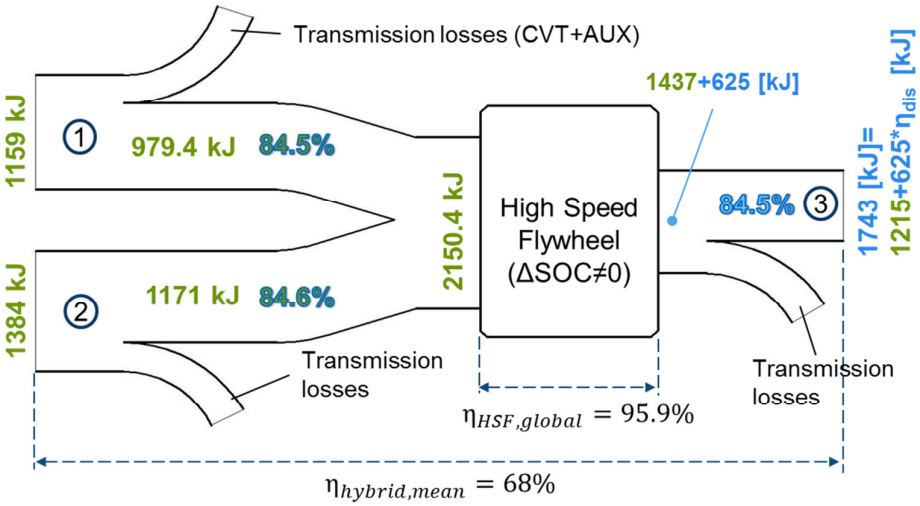

Figure 5.5.3.6 Mean NEDC cycle efficiencies of the components inside hybrid part of the powertrain (Figure 5.5.3.5 – position 2) 1-(mechanical) Recharging energy from ICE 2-(mechanical) Regenerative braking energy 3-(mechanical) HSF traction energy

Figure 5.5.3.6 represents mean cycle efficiency of the components inside hybrid powertrain part (CVT and "step-up" transmission (AUX) and HSF) during NEDC cycle. Since initial SOC value of the HSF-HV simulation is lower than its final value, this difference has to be taken into account. Positions 1 and 2 represent mechanical energy input to the hybrid system – recharging and regenerative braking energy respectively. Position 3 represents calculated mechanical energy output of the hybrid system. This output value (position 3 – 1743 kJ) is calculated under assumption that all excess energy stored in the HSF is discharge until condition is satisfies:

$$SOC_{init,NEDC} = SOC_{final,NEDC} \text{ or } \Delta SOC_{NEDC} = 0$$

Figure 5.5.3.7 represents the behavior of the braking controller during regenerative braking. Utilization of the HSF system is limited by the transmission range of the CVT [11, 13, 17], and once CVT range reaches its maximum transmission limit (Table 5.5.1.1), the HSF system has to be disengaged. This negative characteristic of the system can be responsible for a substantial energetic loss during regenerative braking, when CVT reaches its maximum transmission limit (τ_{cvt}=2.4) and conventional mechanical brakes have to be applied while HSF SOC is still below its maximum value. In order to overcome this problem, a special braking controller has been implemented into the model in order to perform gear downshift during braking and to bring the speed of the primary AMT shaft to acceptable CVT transmission ratio range. In this manner, AMT is used to augment the CVT transmission range and maximize HSF system performance. The operation of braking controller is explained in more detail in the following Figure.

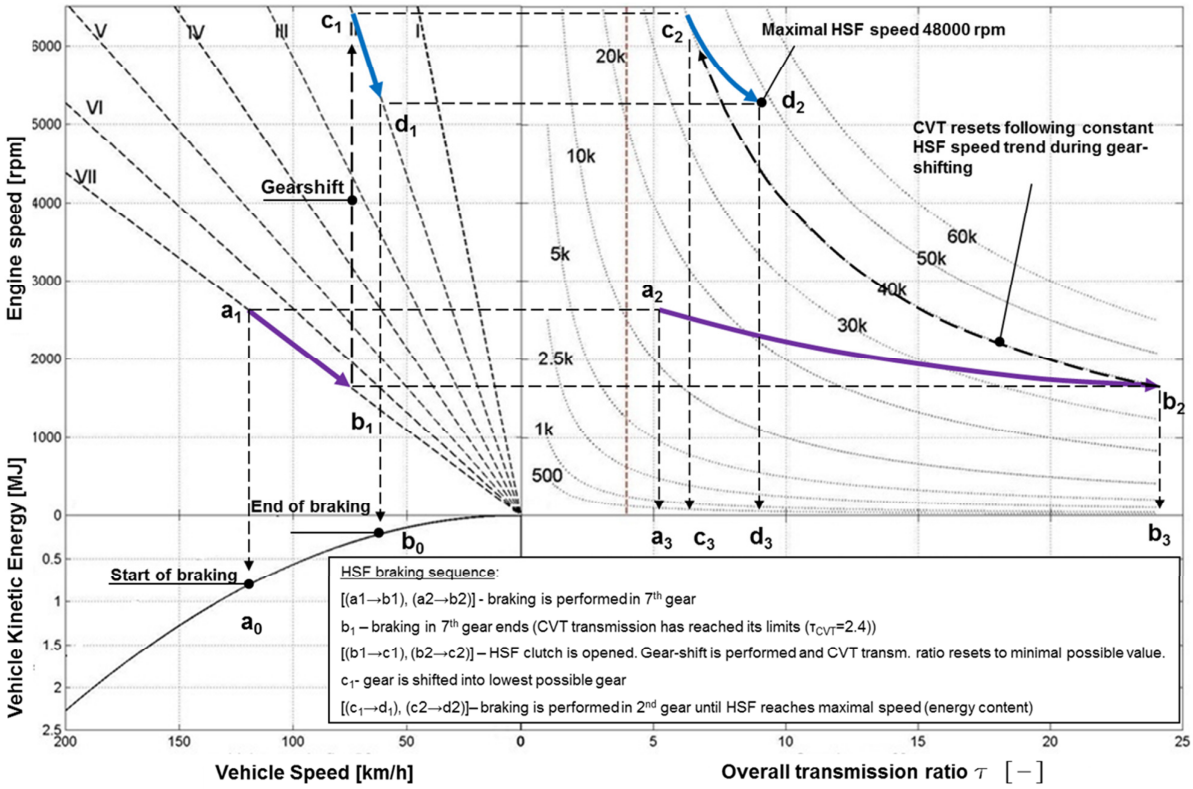

Figure 5.5.3.7– HSF braking controller operation - gear downshift during regenerative braking

Kinematic relations diagram (HSF-KD) between HSF components and the vehicle driveline is given in Figure 5.5.3.7 as explained in [11]. Figure 5.5.3.7 represents braking event at the end of EUDC cycle (braking from 120 km/h to zero), and it graphically explains operation of braking controller. Regenerative braking begins in points a_0, a_1 and a_2 in the corresponding graphs (Figure 5.5.3.7). The first part of regenerative braking in 7th gear ends in points b_1 and b_2 when CVT transmission ratio reaches its maximal value (point b_3). At that point HSF system clutch opens, and gear downshift is performed while selecting lowest possible gear that corresponds as close as possible to minimal CVT transmission ratio value (points c_1 and c_2). Simultaneously with downshift, CVT "tracking" is performed in order to synchronize the clutch speeds of the HSF part and the primary AMT shaft as designated by trend between points b_2 and c_2 (it has to be noted that following the constant flywheel speed trend during "tracking" is possible only in ideal case where no losses within the HSF system are present – in real conditions "tracking" will impose certain energetic loss of the HSF system as defined by equation (5.5.2.19)). Once both operations are completed (downshift and "tracking"), the clutch can be closed and regenerative braking can be continued in 2nd gear until CVT reaches its maximum limit for the second time (points d_2 and d_3).
In the described manner, braking controller is able to expand CVT transmission range utilizing vehicle AMT transmission while increasing energetic recuperative potential of the HSF system during braking.

Table 5.5.3.1 gives numerical results of HSF-HV simulations during NEDC cycle. Since there is a difference between initial and final SOC value during the cycle, both uncorrected and corrected results are given in the following table.

	ECE		EUDC		NEDC	
	FE [lit/100km]	ΔFE [%]	FE [lit/100km]	ΔFE [%]	FE [lit/100km]	ΔFE [%]
base vehicle	6.68	x	5.21	x	5.76	x
HSF (*)	3.67	45.10	4.90	5.85	4.44	22.7
HSF (**)	3.04	54.57	4.29	17.7	3.82	33.5

Table 5.5.3.1 – Simulation results for HSF Hybrid vehicle

(*) – Uncorrected FE results (SOC_{final}=SOC_{max}) (if the HSF system is considered as a Short Term Energy Storage System)
(**) – All the results have been corrected according to ECE regulation regarding SOC balance at the end of the cycle

6. HYDRAULIC HYBRID VEHICLE (HHV)

6.1 HYDRAULIC HYBRID SYSTEMS FOR AUTOMOTIVE APPLICATIONS

The hydraulic power technology is wide spread in automotive sector and mainly utilized for moving machinery and off vehicle road applications (i.e. constructive machinery, refuses trucks, forklifts, military vehicles, telehandlers etc.). It is mature and environment friendly technology with components that are easily serviceable and with relatively low manufacturing costs. Also, hydraulic power systems are robust, conventional materials and processes are used during their fabrication and they can operate even in very harsh conditions and over full range of climatic conditions. Fast response valves and advanced electronic valve actuation, high round trip efficiency of the hydraulic accumulators (~95%) very high specific power of the systems as well as high peak efficiency of hydraulic pumps and motors (~93%) certainly make hydraulic systems competitive with other hybrid systems for automotive applications.

However, technical challenges still remain. Hybrid components have high packaging requirements, hydraulic accumulator systems have low specific energy and are heavy. Also proper sealing of high pressure hydraulic lines onboard the vehicle has to be maintained as well as keeping noise generated by hydraulic pumps or motors at acceptable levels.

Researchers have shown high interest in the recent years to evaluate the feasibility of using hydraulic technology for smaller and commercial vehicles in all possible hybrid configurations – series, parallel or series-parallel combination (power-split).

In 1980's one of the first parallel hydraulic hybrids was launched on the market by Parker Hannifin [48] for urban city busses in Stockholm (Figure 6.1.1 – left side). It was called Cumulo Brake Energy Drive (CBED) and it included variable displacement bent axis pump-motor and a hydro-pneumatic accumulator storage system coupled in the parallel configuration with the rest of the powertrain [52]. Some years later, the same manufacturer presented the serial hydraulic hybrid configuration called Cumulo Hydrostatic Drive (CHD) for use in refuse trucks [48, 52]. Serial CHD configuration can be seen in Figure 6.1.1 – right side.

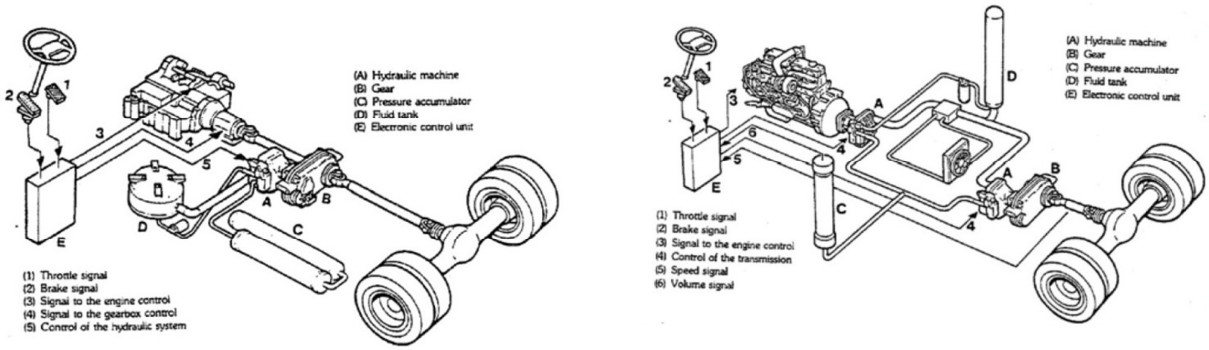

Figure 6.1.1 Cumulo Brake Energy Drive (CBED) on the left Cumulo Hydrostatic Drive (CHD) on the right 1) Throttle signal 2) Brake signal 3) Signal to the engine control 4) Control of the transmission 5) Speed signal 6) Volume signal a) Hydraulic machine b) Gear 3) Accumulator d) Fluid tank e) Electronic control unit

Also several add-on solutions for kinetic energy recuperations (i.e. KERS systems) in parallel hybrid configuration were present to the market. Hydraulic Launch Assistant (HLA) developed by Eaton corp. [53] is suited for vehicles that operate at stop & go duty cycles (refuse trucks) and it offers the possibility to recover most of the kinetic energy usually dissipated during mechanical

braking and reapplying that energy to the powertrain during acceleration. Also, regenerative braking system with similar functionality called Regenerative Drive System (RDS) was introduced by Permo-drive [51].

Considerable research effort into hybrid vehicle propulsion has been carried out by U.S. Environmental Protection Agency (EPA) in corporation with several industrial partners [10, 50, 54]. A series of demonstration hydraulic parallel and series vehicles were presented. Ford Expedition demonstrational SUV was announced and displayed to the public in 2004 SAE World Congress in Detroit, Michigan. It included full serial hydraulic hybrid configuration with diesel engine [54]. In 2006, EPA announced that it has been working on the development of the world's first series hydraulic hybrid urban delivery vehicle [50, 54].

Hydraulically driven UPS truck was showcased at the International Fluid Power Exposition in Las Vegas, stressing the need for utilizing the alternative source of power - the fluid power.

Figure 6.1.2 full serial Hydraulic Hybrid Urban Delivery Vehicle developed by EPA [54]

In the series UPS hybrid vehicle configuration, the mechanical drive train is removed, and the vehicle is powered purely by hydraulics (Figure 6.1.2). The engine is directly coupled to a hydraulic "engine" pump, which is connected to the accumulator and rear drive pump motor. A clutch decouples the engine allowing on/off engine operation. This architecture not only allows the engine output power not to match load demand, but also the engine speed doesn't need to match wheel speed, allowing for optimal engine management. Also, the hybrid system is capable to perform regenerative braking while storing energy as pressure inside hydro-pneumatic accumulator.

The Artemis Intelligent Power Ltd presented hydraulic hybrid transmission based on Digital Displacement Technology® [54] and prototype car was presented.

A full hydraulic hybrid transmission named "Hydrid" was presented in [7, 8]. The hydraulic powertrain includes in-wheel hydraulic motors, hydraulic transformers for variable traction control and a common pressure rail with hydraulic accumulators for power management and energy recuperation [8]. Research effort is made in order to improve the specific power and energy capabilities as well as individual efficiencies of hydraulic components. High efficiency (~98% at [7, 8]) and low noise variable displacement hydraulic pumps and motors are developed featuring new designs and operating principles (multi-piston "floating cup") that result in almost constant torque output and low friction at low rotational speeds [7, 8].

Despite the growing research effort carried out in the recent years in the field of hydraulic hybrids, there are few or none commercial products currently present on the market. Size and complexity seems to limit these systems to special vehicle applications (city busses, refuse trucks etc.) leaving

area of the passenger cars generally unaffected. Adding hydraulic system to small or medium size automobile would result in relatively high weight increase which would offset some of the hybridization benefits. However, "low cost" hydraulic hybridization might represent a viable compromise in order to confront CO_2 emissions especially in developing countries (BRIC countries) where high prices of hybrid electric vehicle limit large scale market expansion.

6.2 HYDRAULIC COMPONENTS MODELING AND SIMULATION

6.2.1 HYDRAULIC ACCUMULATOR MATHEMATICAL MODEL

Hydraulic power systems use hydraulic fluids (oil) in order to convert hydraulic into mechanical energy and vice versa. However, hydraulic fluid is essentially non-compressible and therefore cannot store energy [10].

In order to store and release energy in hydraulic storage system, a hydro-pneumatic accumulator is used [9, 10]. The energy is stored by compressing a gas (usually nitrogen) (Figure 6.2.1.1– position 2) by the incoming oil to the accumulator (Figure 6.2.1.1 – position 5). The gas is stored inside a movable barrier (such as rubber-bladder, metal-lined plastic bag etc.) - (Figure 6.2.1.1– position 1) that separates the gas from the oil and keeps it inside the accumulator.

In order to increase the thermal capacity of the nitrogen charge and to reduce the heat losses, flexible open-celled foam is added to the nitrogen [9, 10, 40 and 41].

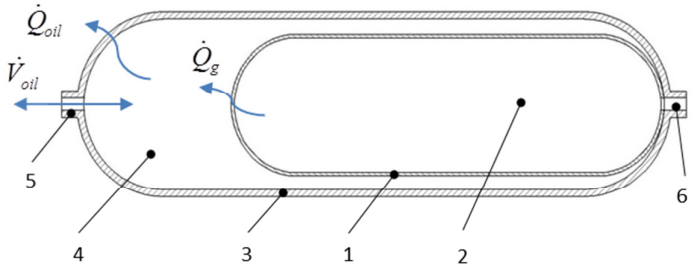

Figure 6.2.1.1– Hydraulic Accumulator model 1-Elastic Bladder wall 2-Nitrogen gas and polyurethane foam 3- Accumulator wall 4-Hydraulic fluid (Oil) 5-Oil input/output port 6- Nitrogen charging port

In order to define thermo-dynamical model of the hydro-pneumatic energy storage system, simple geometry accumulator was adopted (Figure 6.2.1.2).

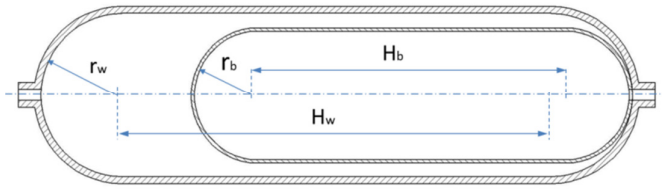

Figure 6.2.1.2–Hydraulic Accumulator geometry

Hydro-pneumatic accumulator consists of accumulator (shell) wall and movable bladder barrier that keeps the nitrogen gas. Bladder volume can be defined with the following equation on basis of Figure 6.2.1.2.

$$V_b = \frac{4}{3} r_b^3 \pi + r_b^2 \pi H_b \qquad (6.2.1.1)$$

Further, ratio between length and radius of the bladder can be introduced as:

$$a_b = \frac{H_b}{r_b} \qquad (6.2.1.2)$$

After simplification that ratio between length and radius of the bladder is constant during operation ($a_b = cons$), with the help of the equations (6.2.1.1) and (6.2.1.2), radius of the bladder r_b (Figure 6.2.1.2) can be defined as

$$r_b = \sqrt[3]{\frac{V_b}{\pi\left(\frac{4}{3} + a_b\right)}} \qquad (6.2.1.3)$$

Also, bladder surface area can be defined as:

$$A_b = 4 r_b^2 \pi + 2 r_b \pi H_b \qquad (6.2.1.4)$$

And taking into account previous equation, bladder surface area can be defined as:

$$A_b = 2\pi \left(\frac{V_b}{\pi\left(\frac{4}{3} + a_b\right)} \right)^{\frac{2}{3}} (2 + a_b) \qquad (6.2.1.5)$$

Accumulator shell wall surface area (6.2.1.6) and volume (6.2.1.7) for gas bladder can be defined as previously:

$$A_b = 4 r_w^2 \pi + 2 r_w \pi H_w \qquad (6.2.1.6)$$

$$V_b = \frac{4}{3} r_w^3 \pi + r_w^2 \pi H_w \qquad (6.2.1.7)$$

The governing energy conservation equation for the inert nitrogen gas inside the bladder can be expressed as:

$$m_g \frac{du}{dt} = -p_g \frac{dv}{dt} - m_f c_f \frac{dT}{dt} - k A_b \left(T_g - T_{oil}\right) \qquad (6.2.1.8)$$

Where m_g and m_f are nitrogen gas and foam mass respectively, k is the global heat transfer coefficient, T_g and T_{oil} are nitrogen and oil temperatures respectively, c_f is the specific heat capacity of the foam and A_b is the bladder wall surface area.

In order to define pressure of the trapped nitrogen inside the accumulator, Benedict-Webb-Rubin equation of state for real gas can be used [2]:

$$p_g = \frac{RT}{v} + \frac{\left(B_0 RT - A_0 - \frac{C_0}{T^2}\right)}{v^2} + \frac{(bRT - a)}{v^3} + \frac{a\alpha}{v^6} + \frac{\left[c\left(1 + \frac{\gamma}{v^2}\right) e^{-\frac{\gamma}{v^2}}\right]}{v^3 T^2} \qquad (6.2.1.9)$$

Where equation coefficients are $a = 0.15703387, A_0 = 136.0474619, b = 2.96625 \cdot 10^{-6}$

$B_0 = 0.001454417$, $c = 7.3806143 \cdot 10^{-5}$, $C_0 = 1.0405873 \cdot 10^{-6}$, $\alpha = 5.7863972 \cdot 10^{-9}$, $\gamma = 6.7539311 \cdot 10^{-6}$.

Differential equation that determines the nitrogen temperature can be defined as:

$$\left(1 + \frac{m_f c_f}{m_g c_v}\right)\frac{dT}{dt} = -\frac{1}{c_v}\frac{dv}{dt}\left[\frac{RT}{v}\left(1 + \frac{b}{v^2}\right) + \frac{1}{v^2}\left(B_0 RT + 2\frac{C_0}{T^2}\right) - \frac{2c\left(1 + \frac{\gamma}{v^2}\right)\cdot e^{-\frac{\gamma}{v^2}}}{T^2 v^3}\right] - \frac{\left(T_g - T_{oil}\right)}{\tau} \qquad (6.2.1.10)$$

Where

$$\tau = \frac{m_g c_v}{k A_b} \qquad (6.2.1.11)$$

Equation (6.2.1.11) represents nitrogen gas time constant [9, 40 and 41]. In order to increase the round-trip efficiency of the accumulator, it is proposed to add elastomeric foam to the gas side of the accumulator which results in the increase of thermal capacity of the nitrogen [9, 10, 40 and 41].

Furthermore, oil temperature inside the hydraulic system can be determined from the following equation that takes into account heat exchange between hydraulic oil and nitrogen, ambient and dissipated heat from mechanical friction of the hydraulic motor pump (HMP). It can be expressed as:

$$m_{oil} c_{v,oil} \frac{dT_{oil}}{dt} = k_b A_b\left(T_{N_2} - T_{oil}\right) - k_w A_w (T_{oil} - T_{amb}) + \dot{Q}_{HMP} \qquad (6.2.1.12)$$

Where k_b and k_w are global coefficient of heat transfer for oil and nitrogen and nitrogen and ambient respectively, and they are defined as (Figure 6.2.1.1):

$$k_b = \frac{1}{\frac{1}{h_{N_2}} + \frac{S_b}{\lambda_b} + \frac{1}{h_{w,oil}}} \qquad (6.2.1.13)$$

$$k_w = \frac{1}{\frac{1}{h_{w,oil}} + \frac{S_w}{\lambda_w} + \frac{1}{h_{w,amb}}} \qquad (6.2.1.14)$$

Hydraulic fluid (oil) temperature was monitored during the simulation in order to determine necessity of the oil heat exchanger in the hydraulic circuit.

The State of Charge (SOC) of the hydraulic accumulator was defined on the basis of the ratio between instantaneous volume of the fluid inside the accumulator and the maximal accumulator (shell) volume [2]. The SOC was linearly dependent on the variation of the ratio of volumes.

$$SOC = SOC(r) \qquad (6.2.1.15)$$

$$SOC(r_{max}) = SOC_{max} \qquad (6.2.1.16)$$

And

$$SOC(r_{min}) = SOC_{min} \qquad (6.2.1.17)$$

While the ratio r was defined as:

$$r = \frac{V}{V_{max}} \qquad (6.2.1.18)$$

During hydraulic accumulator operation, maximal and minimal ratio was selected between 0.5 and 0.1 respectively and it corresponded to maximal and minimal SOC value.

$$0.1 \leq r \leq 0.5 \qquad (6.2.1.19)$$

Initial State of Charge of the hydraulic storage system was defined as parameter needed to initialize the simulation and initial ratio was defined in the following manner:

$$r_{init} = r_{min} + \frac{(r_{max} - r_{min})(SOC_{init} - SOC_{min})}{SOC_{max} - SOC_{min}} \qquad (6.2.1.20)$$

$$V_{N_2,init} = V_{max} - r_{init} \cdot V_{max} \qquad (6.2.1.21)$$

Where V_{max} is the maximal accumulator (shell) volume.

The hydraulic system for hybrid vehicle stores hydraulic energy inside High Pressure Accumulator (HPA) but has to have additional vessel in order to store the hydraulic fluid when it is not in the HPA. This additional vessel operates at significantly lower pressures than HPA just in order to provide sufficient inlet pressure for the hydraulic pump to avoid cavitation [10]. In the further text, this reservoir of hydraulic fluid will be designated as Low Pressure Accumulator (LPA).

Following table gives specifications of the High Pressure (HPA) and Low Pressure Accumulators (LPA) used in Hydraulic Hybrid Vehicle simulations.

item	unit	HPA	LPA
Nitrogen mass (m_{N_2})	[kg]	5.5	0.3
Foam mass (m_f)	[kg]	5	5
Pre-charge/maximal pressure	[MPa]	13/44	0.5/ 0.95
Weight	[kg]	91.7*	22

Table 6.2.1.1 – High Pressure Accumulator (HPA) and Low Pressure Accumulator (LPA) (reservoir) specifications (*) - with hydraulic fluid

6.2.2 HYDRAULIC MOTOR PUMP (HMP) MODELING AND EFFICIENCY

In order to convert hydraulic into mechanical energy and vice versa, axial piston variable displacement Hydraulic Motor Pump (HMP) has been used. The HMP is connected to the High pressure (HPA) and Low Pressure Accumulators (LPA). During pumping operation, mechanical energy has to be supplied to the HMP shaft in order to increase HPA pressure and to transport hydraulic fluid from LPA to the HPA. During motor operation, HMP converts hydraulic energy into mechanical and supplies it to the powertrain, following a pressure decrease in the HPA. Hydraulic fluid flow can be continuously regulated by changing the displacement of the HMP. Therefore, ideal (leak free) volumetric flow rate can be defined as [9]:

$$Q_i = x \cdot \omega \cdot D \qquad (6.2.2.1)$$

Where x $[-]$ is the displacement factor of the Hydraulic Motor Pump, ω $[\frac{rad}{s}]$ - angular velocity and displacement per radian D $[\frac{m^3}{rad}]$.

Ideal (frictionless) torque at HMP shaft is given as [9]:

$$T_i = x \cdot \Delta p \cdot D \qquad (6.2.2.2)$$

Where Δp is the pressure difference across the machine.

In order to investigate losses of the hydrostatic machines many mathematical models based on modified Wilson's hydraulic pump theory were developed [42-47]. According to [47] the overall efficiency of the hydrostatic machine can be defined as:

$$\eta_o = \eta_V \cdot \eta_{hm}$$

Where η_V and η_{hm} are volumetric and hydro-mechanical efficiencies of the machine respectively.

Volumetric efficiency is defined as the ratio between actual of theoretical pump flow available to do useful work and it can be contributed to several factors [47]:

- Laminar and turbulent leakage losses through the clearances of the machine due to pressure gradients
- Compressibility of the hydraulic fluid
- Presence of dead volume

Based on [9] volumetric efficiency for the hydraulic pumps and motors can be defined as:

$$\eta_{V,pump} = \frac{Q_a}{Q_i} = 1 - \frac{C_s}{|x|S} - \frac{\Delta p}{\beta} - \frac{C_{st}}{|x|\sigma} \qquad (6.2.2.3)$$

$$\eta_{V,motor} = \frac{Q_i}{Q_a} = \frac{1}{1 + \frac{C_s S}{|x|} + \frac{\Delta p}{\beta} + \frac{C_{st}}{|x|\sigma}} \qquad (6.2.2.4)$$

Where β is the oil bulk modulus of elasticity [Pa], and S and β are dimensionless numbers [9].

Hydro-mechanical or torque efficiency of the machine represents ratio between actual and ideal torque and is related to three basic forms of friction [9, 42, 43 and 47]:

- Dry (coulomb) friction – described as being proportional to the load (pressure)

- Viscous friction – proportional to the viscosity and speed of operation

- Hydrodynamic friction – i.e. seal friction

Based on [9] torque efficiency for the hydraulic pumps and motors can be defined as:

$$\eta_{t,pump} = \frac{T_i}{T_a} = \frac{1}{1 + \frac{C_v S}{|x|} + \frac{C_f}{|x|} + C_h x^2 \sigma^2} \qquad (6.2.2.5)$$

$$\eta_{t,motor} = \frac{T_a}{T_i} = 1 - \frac{C_v S}{|x|} - \frac{C_f}{|x|} - C_h x^2 \sigma^2 \qquad (6.2.2.6)$$

In order to identify the efficiency maps of the variable displacement machines over whole range of operation and for different operating conditions, coefficient loss model approach was implemented. The methodology on basis of theoretical considerations defines a set of equations and a set of coefficients which are evaluated with experimental data using multi-variable least squares regression [47].

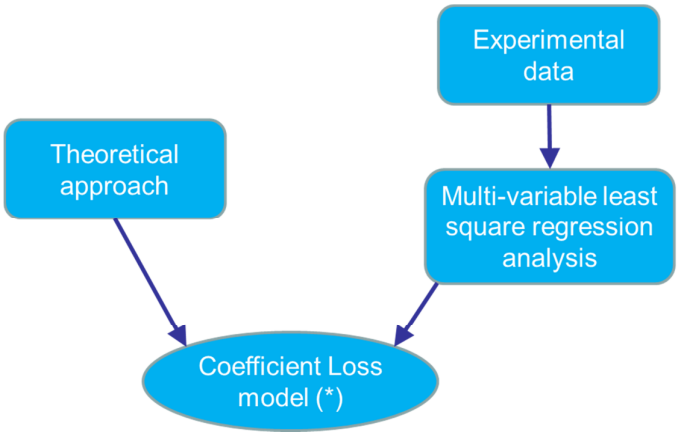

Figure 6.2.2.1 Coefficient loss model flowchart [47]

Coefficient loss model is based on constant value of fluid viscosity, can be used for in-line and bent axis piston machines and also can be used for fixed and variable displacement machines [47]. Figure 6.2.2.1 represents flow chart of implemented model. On the basis of the operational parameters of the motor or pump – speed, displacement and pressure difference between inlet and outlet ports, model can determine actual volumetric flow and torque at the HMP shaft as well as torque and volumetric efficiency of the machine.

Figure 6.2.2.2 Coefficient loss model inputs and outputs

Figures 6.2.2.3 and 6.2.2.4 represent example of volumetric and hydro-mechanical efficiency for a hydraulic motor of 118.6 cm^3/rev. Both figures have been created on the basis on [47].

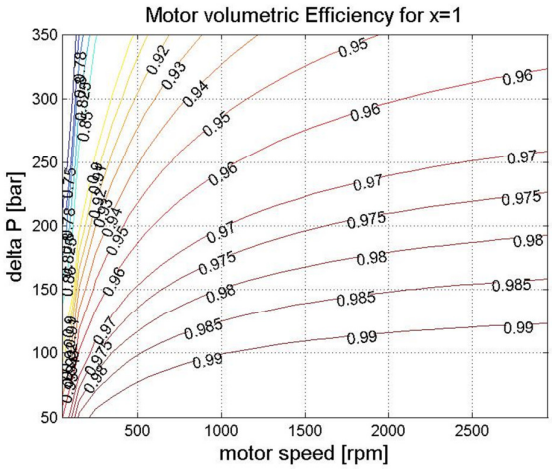

Figure 6.2.2.3.Volumetric efficiency for a hydraulic motor SMV-24 with displacement of 118.6 cm^3/rev

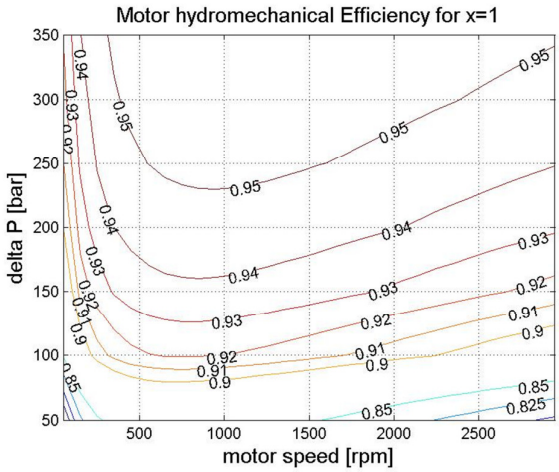

Figure 6.2.2.4 Torque efficiency for a hydraulic motor SMV-24 with displacement of 118.6 cm^3/rev

In the general case, global efficiency of the variable displacement Hydraulic Motor Pump is a function of three parameters – load, speed and the displacement. An example of efficiency maps and actual effective (shaft) power for one bent-axis hydraulic pump (V11-110) and motor (V11-110) build on the basis of [47] are given in Appendix II. Both machines have equal displacement of 110 cm^3/rev.

6.2.3 MODELING LOSSES IN HYDRAULIC CIRCUITS

In order to develop high fidelity simulation of the hydraulic circuit, concentrated and distributed pressure drop losses have also been taken into account. Pressure drop losses are calculated on basis of selected characteristics of the lines (High Pressure Line (HPL) and Low Pressure Line (LPL)) as described in the following.

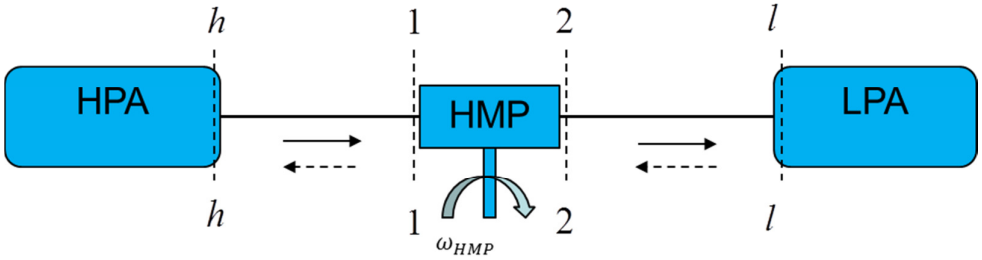

Figure 6.2.3.1 – Simplified hydraulic circuit layout

Figure 6.2.3.1 represents simplified hydraulic circuit layout with two distinct sections:

- High pressure section between High Pressure Accumulator (HPA) and Hydraulic Motor Pump (HMP) designated as $h - 1$
- And low pressure section between Hydraulic Motor Pump (HMP) and Low Pressure Accumulator (LPA) designated as $2 - l$

During motor operation, fluid is discharged from section h to section l. Vice versa, during pumping operation fluid is transported from section l to section h of the circuit.

Pressure drop between sections h and 1 that takes into account concentrated (HPA entry loss) and distributed losses in the hydraulic lines can be expressed as:

$$\Delta p_{1h} = \frac{\rho v_{1h}^2}{2}\left(\xi_h + \lambda_h \frac{L_{1h}}{D_{1h}}\right) \qquad (6.2.3.1)$$

Analogically, pressure drop between sections 2 and l is:

$$\Delta p_{2l} = \frac{\rho v_{2l}^2}{2}\left(\xi_l + \lambda_l \frac{L_{2l}}{D_{2l}}\right) \qquad (6.2.3.2)$$

Therefore, pressure drop across the hydraulic motor during discharging can be defined as:

$$\Delta p_{dis} = p_{HPA} - p_{LPA} - \Delta p_{1h} - \Delta p_{2l} \qquad (6.2.3.3)$$

And pressure drop across hydraulic pump during charging:

$$\Delta p_{chg} = p_{HPA} - p_{LPA} + \Delta p_{1h} + \Delta p_{2l} \qquad (6.2.3.4)$$

Hydraulic fluid also exchanges heat with the ambient through wall of the hydraulic lines, but these losses were disregarded due to relatively low fluid temperature during operation and low expected impact on the accuracy of the results.

6.3 HYDRAULIC HYBRID VEHICLE (HHV) SIMULATION RESULTS

6.3.1 HHV POWERTRAIN LAYOUT AND CHARACTERISTICS

The parallel Hydraulic Hybrid powertrain consists of engine and hydraulic pump motor added in parallel configuration to the primary shaft of the AMT (Figure 6.3.1.1). The hydraulic pump motor is an axial piston variable displacement type machine and it is connected to the High Pressure Accumulator (HPA) and Low Pressure Accumulator – reservoir (LPA). The pressure difference between the high and low-pressure accumulator is transformed into mechanical power at the Hydraulic Motor Pump (HMP) shaft and is transmitted to the driveline during traction. During recharging and regenerative braking, HMP operates in pumping mode in order to increase the pressure difference between the accumulators and effectively store the energy. Power distribution between the internal combustion engine and secondary energy converter part is governed using the same control law as for the HEV, HSF and PHV systems. HMP efficiency maps have been taken from [7].

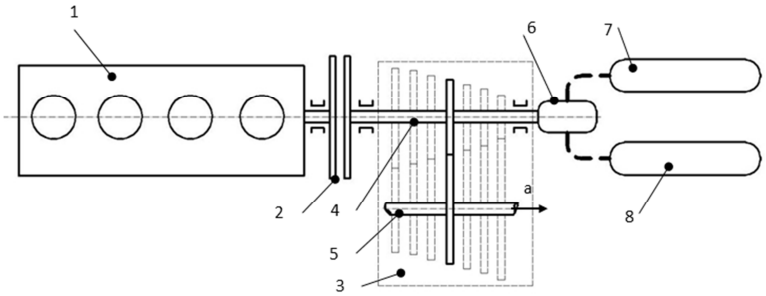

Figure 6.3.1.1 – Hydraulic Hybrid Vehicle (HHV)Powertrain simplified layout 1-ICE 2-ICE clutch 3-Automated Manual Transmission (AMT) 4-Primary AMT shaft 5-Secondary AMT shaft 6-Hydraulic Motor-Pump (HMP) 7-High pressure Accumulator (HPA) 8-Low pressure Accumulator (LPA) a-Power flow to the differential-front semi-axle-wheel

Table 6.3.1.1 represents HHV system description and the main simulation parameters.

Hydraulic Motor Pump: Axial piston type		
displacement per revolution	[cc/rev]	45
Max power (at 44MPA, 4000rpm)	[kW]	125
weight	[kg]	15
High Pressure Accumulator (HPA)		
volume total	[lit]	69
pre-charge press	[MPa]	13
max charge press	[MPa]	44
Maximal Energy content (SOC=1)	[kJ]	625
Weight (with oil included)	[kg]	91.7
Low Pressure Accumulator (LPA)		
volume total	[lit]	69
Pre-charge press	[MPa]	0.5
max charge press	[MPa]	0.95
Weight	[kg]	22

Hydraulic fluid		
type: High grade mineral oil -Group III (with high viscosity index)		
weight	[kg]	33.5
Hydraulic lines		
High Pressure Line (HPL)	diameter	1"
Low Pressure Line (LPL)	diameter	1.25"
weight	[kg]	6.6
HHV overall mass	[kg]	1605.6

Table 6.3.1.1 – HHV simulation parameters

6.3.2 NEDC CYCLE SIMULATION RESULTS AND ENERGETIC ANALYSIS

The HHV simulations were performed on different homologation cycles in order to determine the fuel economy benefits of the selected hybrid powertrain configuration. Full results are disclosed for NEDC cycle and include complete powertrain energetic analysis. Following figure represents HHV simulated speed profile over NEDC cycle and HPA SOC value.

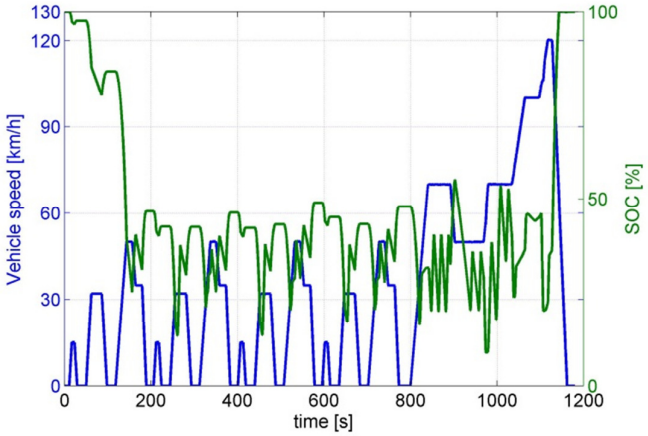

Figure 6.3.2.1 - NEDC simulated speed profile and hydraulic accumulator SOC trend for HHV

The Figures 6.3.2.2 and 6.3.2.3 displays distribution of ICE operating points during NEDC cycle. It can be noted that engine operating points of HHV have been shifted to the regions of lower brake specific consumption values with respect to base vehicle resulting in the higher fuel conversion efficiency of the engine.

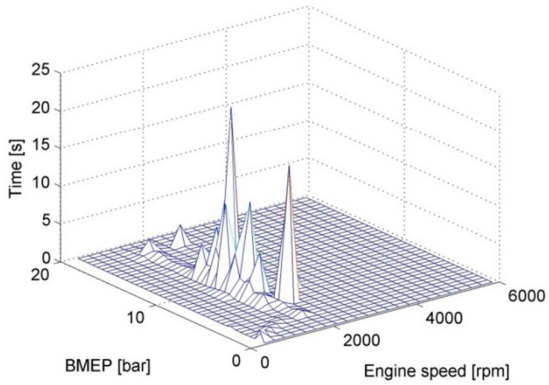

Fig 6.3.2.2 Distribution of ICE operating points (sec) during NEDC cycle

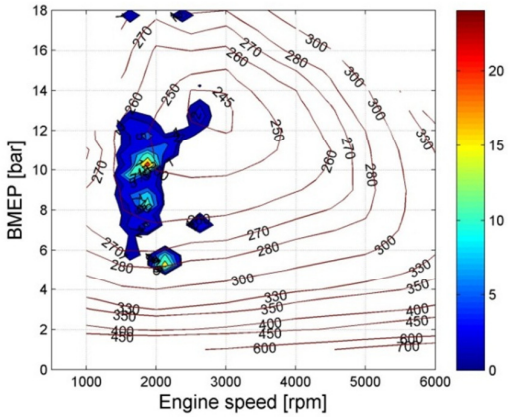

Figure 6.3.2.3 - Distribution of ICE operating points (sec) during NEDC cycle - contour views

Due to the effect of engine load point moving the mean engine efficiency during NEDC cycle has been increased from 0.23 (Figure 2.4.4) to approximately 0.32 (Figure 6.3.2.7). Figures 6.3.2.4 and 6.3.2.5 represent instantaneous efficiency of the Hydraulic Motor/Pump (HMP) during NEDC cycle.

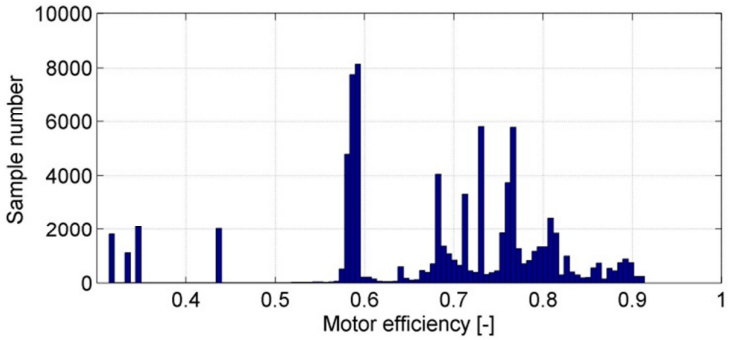

Figure 6.3.2.4– Instantaneous Hydraulic Motor efficiency over NEDC cycle

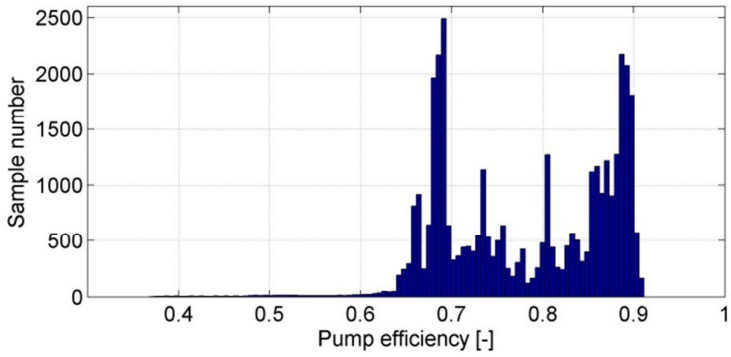

Figure 6.3.2.5 – Instantaneous Hydraulic Pump efficiency over NEDC cycle

Figure 6.3.2.6 represents displacement factor histogram of the HMP during NEDC cycle. Positive values are related to motor operation while negative values are related to pumping operation of the HMP.

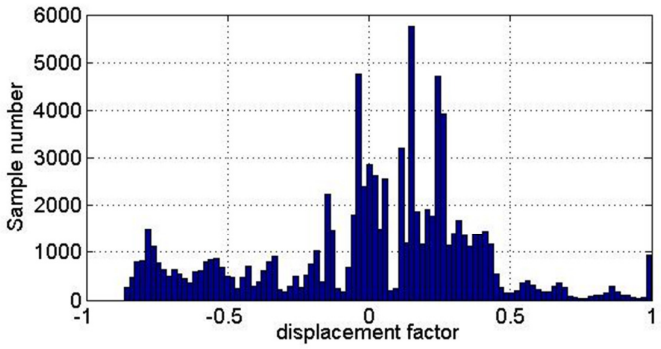

Figure 6.3.2.6 - HMP displacement factor during NEDC cycle

The energetic analysis represented in the Figure 6.3.2.7 was carried out in order to determine the amount and distribution of all energies within the powertrain. Energies represented in Figure 6.3.2.7 are referred to the primary AMT axis. The overall energy of the engine is divided into two parts – direct (mechanical) traction energy to the wheels and the energy used to recharge the Hydraulic Accumulator in low SOC conditions (Figure 6.3.2.7 – positions 5,6). During low loads (when engine efficiency is also low) hydraulic system will provide traction (Figure 6.3.2.7 – position 7), in accordance with SOC availability. Braking is performed in regenerative mode always when possible, limited not only by HMP power potential and maximum permissible SOC value (Figure 6.3.2.7 – position 8), but also by required vehicle deceleration. Positions 9, 10 and 11 represent mechanical braking energy, aerodynamic resistance energy and rolling friction energy, respectively.

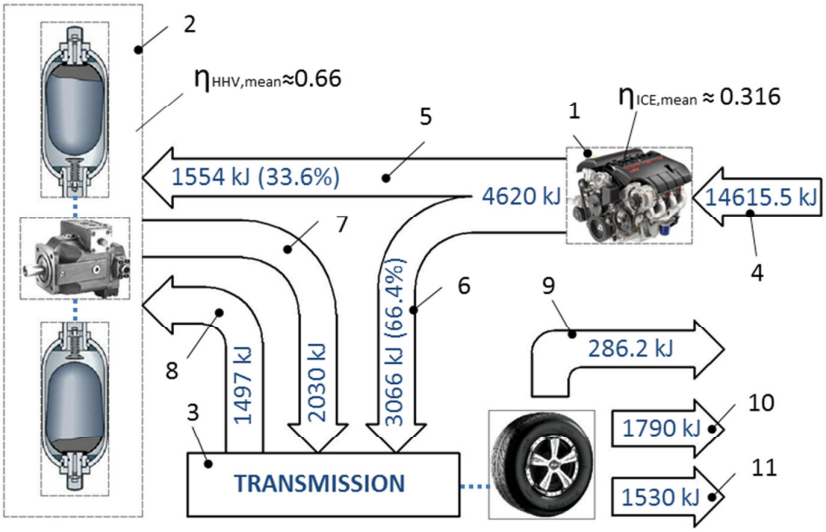

Figure 6.3.2.7 - HHV powertrain energetic analysis for NEDC cycle (all energies are referred to the primary AMT shaft axis): 1-Internal Combustion Engine 2-Hybrid powertrain part (Hydraulic Motor Pump HMP, High and Low pressure accumulators HPA, LPA) 3- Vehicle transmission 4-Fuel energy consumed during the cycle 5-Direct recharging energy (from ICE to the HMP 6-Direct traction energy (from the ICE to the transmission)7-Hybrid traction energy (from the hybrid system to the transmission) 8-Regenerative braking energy (from the transmission to the hybrid system)9-Mechanical braking energy 10-Aerodynamic resistance energy 11-Rolling resistance energy

Based on Figure 6.3.2.7, mean engine efficiency can be determined as ratio of energy produced and the energy introduced by the fuel. Mean efficiency of the hydraulic part of the powertrain can be

determined as ratio of energy output and the energy introduced during recharging and regenerative braking (in accordance with the ΔSOC≠0 correction). Based on energetic analysis it can be observed that a substantial part of braking energy is lost due to insufficient energetic storage capacity (Figure 6.3.2.7 position 9).

The simulation was performed with initial SOC values of 100% and has resulted in "neutral" SOC balance during NEDC cycle (ΔSOC=0). Fuel economy results (FE*) given in Table 6.3.2.1 represent fuel economy values that have been corrected for different initial and final SOC values [12] for a given cycle (Urban and Extra Urban part).

	ECE		EUDC		NEDC	
	FE* [lit/100km]	ΔFE* [%]	FE* [lit/100km]	ΔFE* [%]	FE [lit/100km]	ΔFE [%]
base	6.68	x	5.21	x	5.76	x
HHV	3.16	52.67	4.76	8.62	4.17	27.57

Table 6.3.2.1 – Simulation results for HHV Hybrid vehicle

(*) – All the results have been corrected according to ECE regulation regarding SOC balance at the end of the cycle

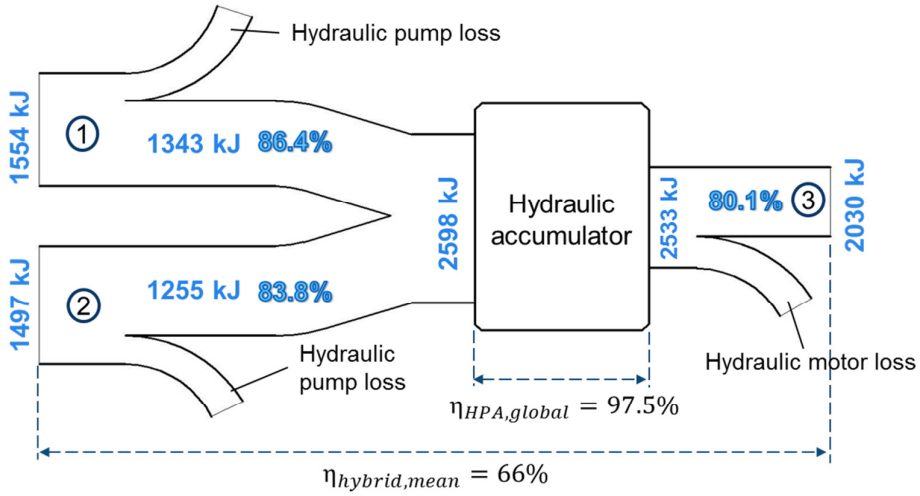

Figure 6.3.2.8- Mean NEDC cycle efficiencies of the components inside hybrid part of the powertrain (Figure 31 – position 2) 1- (mechanical) Recharging energy from ICE 2- (mechanical) Regenerative braking energy 3-(mechanical) HHV traction energy

Figure 6.3.2.8 represents analysis of mean hybrid cycle efficiency. Position 1 represents recharging portion of the engine energy while position 2 represent energy from the regenerative braking. Position 3 represents traction energy supplied to the vehicle by the hybrid system.

7. PNEUMATIC HYBRID VEHICLE (PHV)

7.1 INTRODUCTION TO COMPRESSED AIR VEHICLES AND ENERGY STORAGE SYSTEMS

As strange as it may seem from modern perspective, pneumatic propulsion systems for vehicles and moving machinery have been present long before modern systems, as we know them today.

The first idea of using compressed air engine comes from Denis Papin (1647 - 1712), a French physicist, mathematician and inventor. His pioneering invention of steam digester (steam cooker) that was used to extract fat from bones [31] in the high pressure steam environment inspired the development of the steam engine later on.

The first compressed air vehicle was constructed by two Frenchman, Andrund and Tessie du Motay in 1840 (Figure 7.1.1). It was designed to run on rails, it had air storage pressure of 17 atmospheres and was capable of carrying up to eight passengers. This vehicle was tested with a success, but the idea was not pursued any further. Also, they contemplated of applying storage system of 60 atmospheres and heating of the air during three stage expansions [56].

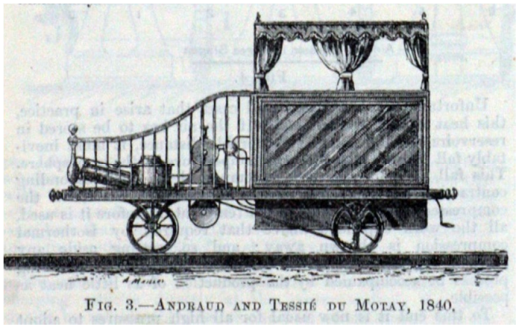

Figure 7.1.1 The first compressed air vehicle constructed in 1840 by Andrund and Tessie

Thirty years later the idea of using compressed air as means of propulsion was revived by Louis Mékarski, a French engineer and inventor of Polish origin. The Mékarski air engines were used in trams and locomotives for public transport in 1872 in several cities in France and USA as an alternative to horse-powered or steam-powered trams. It included single stage engine while the front of the engine carried a tank which could be refilled with compressed air at every station. The engine was also equipped with a system that would add heat to the air during expansion and this represented important advance in terms of pneumatic engines [57].

Numerous locomotives were manufactured and a number of regular lines were even opened up (the first in Nantes in 1879). Mékarski system tram networks were also built in other towns in France: Vichy (1895), Aix-les-Bains (1896), La Rochelle (1899), and Saint-Quentin (1901).

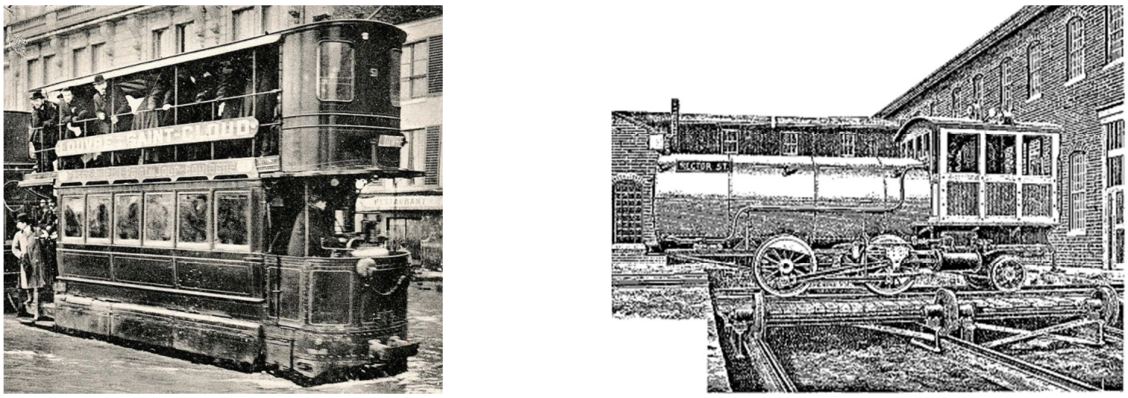

Figure 7.1.2 – Air powered trams in public transport service from 1879 constructed by Louis Mékarski (left) and Compressed Air Locomotive by Hardie (1892)

In 1892 Robert Hardie presented one stage expansion engine air powered locomotive to the streets of New York that had more advanced reheating system than Mékarski engine. A new feature was regenerative braking capability i.e. using pneumatic motor as a compressor during braking in order to recover braking energy and increase range of the vehicle [58].

One of the first commercially successful air cars was built by Charles B. Hodges in 1896. It included two-stage expansion engine with inter-heating between the stages. Hundreds of these locomotives were sold to coal-mining companies in the eastern U.S. due to the fact that these locomotives produced no heat or spark and therefore were invaluable for mining operations where gas explosions were always a danger.

In the decades to come, pneumatic locomotives became widespread in mining operations through Europe (Germany, France, Belgium), with increasing number of expansion stages [58].

In 1926, Lee Barton Williams from the US invented an automobile that used both gasoline combustion and compressed air in order to run the engine. The engine would have been started and run on gasoline, but at vehicle speeds above 16 km/h the fuel supply would be cut-off, and the engine would be run on compressed air only [59].

Between 1970's and 1980's several inventors competed to present to the market their "air car" solutions. Inventor Joseph P. Troyan designed the air powered flywheel in a closed system. Also in the same period Willard Truitt presented his air car invention.

An experimental model of the compressed air car was built by Sorgato of Italy in January 1975. It could run at 30 mph for approximately 2 hours. In 1976 in Vacaville, California, Ray Starbard invented a compressed air truck [58, 59].

In 1979, Terry Miller invented Air Car One which only cost him $1,500 to build [58]. He patented his car that ran on compressed air.

Presently, various individual inventors and companies still pursue the dream of developing efficient and affordable compressed air vehicles as a viable pollution free city transport solution. Recently, French company MDI founded by Guy Nègre in 1991 has been working on development of lightweight air powered urban city vehicle [60], as well several city car versions. In 2007, Tata Motors introduced the MDI CityCat developed by Guy Nègre as the first commercial air car. As of 2009, two more models of MDI air cars have been showcased.

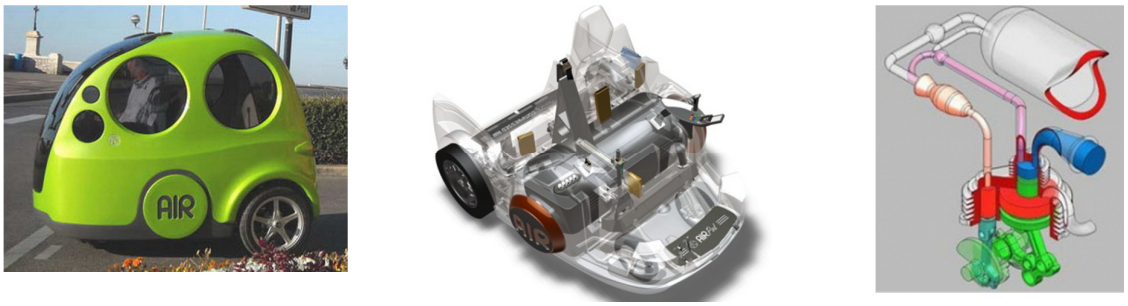

Figure 7.1.3 MDI zero emission air powered vehicle "AirPod" – from left to right – concept vehicle, chassis and powertrain, operating principle of Dual- energy engines (Compressed air and energetic adjuvant)

In the case of MDI air car, ambient air is compressed and stored in the 175 liter vehicle's tank at pressure of 35 MPa. During traction, the compressed air is fed to the expansion machine through

the pressure reducer and external combustion chamber which is added in order to heat the compressed air before starting the expansion process. The combustion process is continuous and not related to the engine's cycle. The expansion machine consists of a charge cylinder and an expansion cylinder (Figure 7.1.3). The feeding of the charge cylinder is performed at constant pressure and temperature while expansion of the volume of air created by the charge cylinder is carried out in the expansion cylinder. The manufacturer promises large vehicle range (220 km), fast recharging time of 1.5 minutes and low cost of 0.5 €/100km.

Most of the previously mentioned vehicles used only stored compressed air as means for propulsion. However in the recent years, many alternative hybrid pneumatic solutions were investigated.

Basic idea behind another interesting pneumatic hybrid concept presented by Guzzella [70-72] is to use the internal combustion engine not only for combustion, but also as a pump and a pneumatic motor.

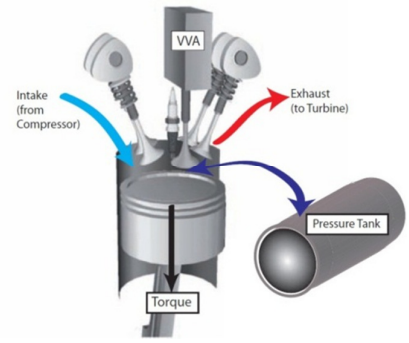

Figure 7.1.4 – Pneumatic Hybrid Engine [70-72]

During vehicle braking, ICE would operate as pneumatic compressor (in 2 or 4 stroke mode) in order to compress the intake air inside a 20 liter vessel. Upon request, this air can be used in pneumatic motor mode to drive the vehicle or to reduce turbo lag effect during engine transients. Authors state that when compared to a naturally aspirated engine with the same rated power, the downsized and supercharged hybrid pneumatic engine can save as much as 32% of the fuel [72].

Similar concept of using internal combustion engine as a compressor during vehicle deceleration was presented by Trajković [73, 74].

Beside the applications in automotive sector, it should be mentioned that interest in compressed air energy storage in increasing in order to match intermittent renewable energy with customer demand, as well as to store excess electric energy in the grid during night and day cycles [67-69]. Compressed air energy storage (CAES) is a promising method for energy storage, with high efficiency and environmental friendliness. Ambient air is compressed isothermally inside large underground storage tanks (underground caverns or man-made vessels).

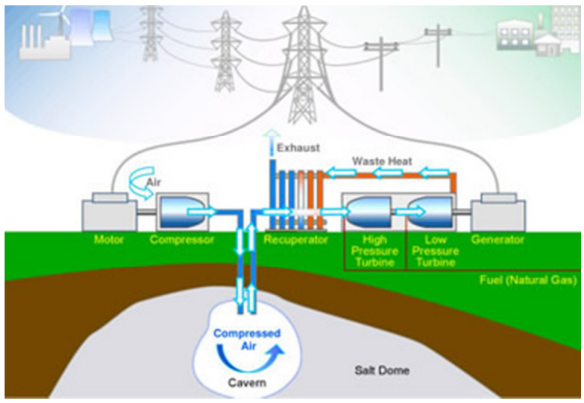

Figure 7.1.5 – Compressed Air Storage System (CAES)

Dissipated heat during compression can be used for residential heating, which can contribute to overall efficiency improvements. In addition, compressed air systems can be used for both power generation and cooling load. When needed, compressed air can be expanded isothermally in turbine that is coupled with electric generator that will supply electrical energy to the grid. During expansion process heat is added to the air by burning fuel (Figure 7.1.5).

The idea of constructing and introducing to the market efficient air compressed vehicle is very tempting. The air-powered vehicle would emit pure air to the ambient and could be very valuable in improving air quality in modern polluted cities. Also, air is not flammable, air compression technology is relatively simple and environmentally friendly, production and maintenance cost of such car would also be very low, refueling could be easily done at home and above all, air is free of charge.

However, a series of negative aspects hinders faster development of air compressed vehicles. First of all, low specific energy of compressed air storage represents considerable disadvantage. At 20°C a 300 Liter tank filled with compressed air at 300 bar holds only 51 MJ of energy (equivalent to approximately 1.3 liters of gasoline) [61]. The Plug-to-Wheel efficiency of compressed air vehicle is relatively low (less than 40%) since energy path suffers from several energy conversions [61]. In order to improve overall efficiency, compression and expansion process should be as close as possible to isothermal process [61] which would imply using heat exchangers during multi-stage compression and expansion. This might not be possible when having in mind tight packaging requirements of the modern vehicles. Also, if the starting air temperature during expansion is bellow certain threshold, low discharge temperature could cause generation of ice from water vapors in the expansion machine or in the exhaust ducts. It should be stated that this drawback in certain cases might be advantageous when air-conditioning is required. If the air is not reheated during expansion process, it might be necessary to completely dehydrate the air during compression in order to protect the pneumatic motor from inner icing.

7.2 PNEUMATIC HYBRID VEHICLE MODELING

7.2.1 PNEUMATIC HYBRID VEHICLE LAYOUT AND MAIN CONTROL PARAMETERS

Following chapter explains Pneumatic Hybrid Vehicle layout and gives detailed models of powertrain components. The parallel Pneumatic Hybrid powertrain includes engine and Pneumatic Motor Compressor (PMC) added in parallel configuration to the primary shaft of the AMT (Figure 7.2.1.1). The Pneumatic Motor Compressor is a two stage variable displacement piston machine that can operate in both compressor and pneumatic motor modes. The PMC is connected to the high pressure Air Storage Tank (AST) that acts as energy storage system (Figure 7.2.1.1 – position 8). In order to increase the overall efficiency of the system, AST has been conveniently placed downstream of the engine exhaust manifold in order to recuperate part of the exhaust gas energy (as it will be explained later on).

The PHV has similar operational characteristics to previously analyzed hybrid cases (HEV, HSF and HHV). Power distribution between the internal combustion engine and secondary energy converter part is governed using the same control law as for the HEV, HSF and HHV systems.

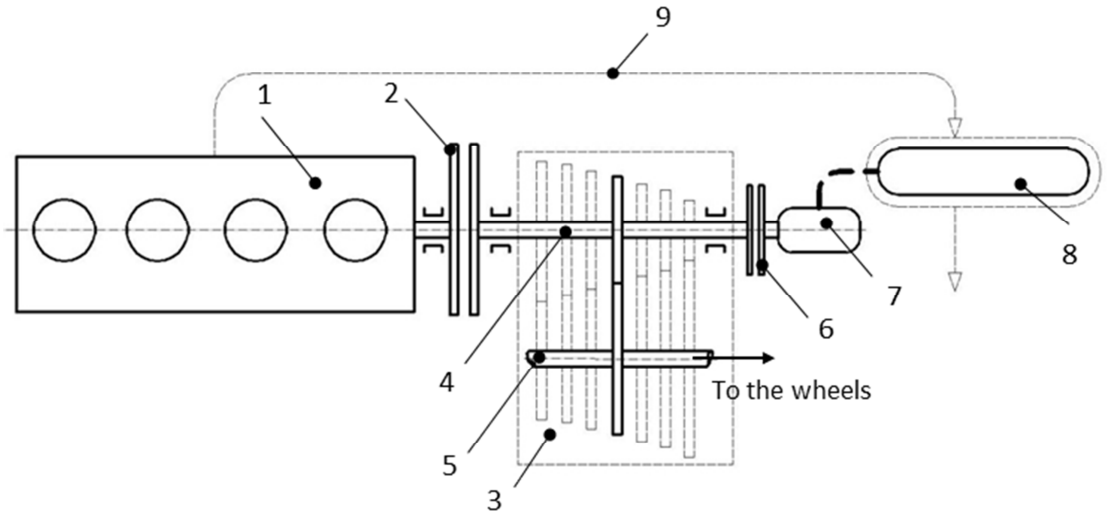

Figure 7.2.1.1 – Pneumatic Hybrid Vehicle (PHV) simplified layout 1-ICE 2-Main clutch 3-7 speed Automated Manual Transmission (AMT) 4-Primary AMT shaft 5-Secondary AMT shaft 6-Secondary (hybrid)clutch 7-Pneumatic Motor-Compressor (PMC) 8-Air Storage Tank with Exhaust gas recuperation (AST) 9-Exhaust gas flow

Figure 7.2.1.2 gives layout for main control parameters in the closed loop PHV system. The simulated pneumatic part of the powertrain consists of three blocks:

- ECUforPHV – In function of torque request that arrives from main supervisory control unit (HCU), the ECUforPHV block regulates displacement of the PMC with parameter x_{air}. Parameter x_{BP} regulates operation of backpressure valve that is used in order to limit minimal discharging temperature of the air.
- PMC block – includes model of the Pneumatic Motor Compressor defined on the basis of politropic compression and expansion process. The PMC model generates air mass flow through the PMC and effective (shaft) torque/power.
- Air Storage Tank (AST) – this block includes thermodynamic model of the air storage tank with exhaust gas recuperation.

In order to regulate the minimal temperature during expansion, discharge valve (backpressure valve BP) was added downstream the PMC during expansion. Control of the BP valve is given by X_{BP} control variable (Figure 7.2.1.2). Presence of the BP valve is particularly important during system warm-up as it will be demonstrated later on.

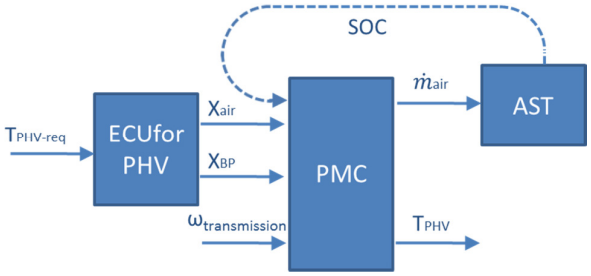

Figure 7.2.1.2 – Closed Loop PHV control layout (main parameters)

In the following chapters, detailed explanation of the models of the PMC and AST with exhaust gas recuperation will be presented as well as the simulation results of the pneumatic hybrid vehicle during NEDC cycle.

7.2.2 PNEUMATIC MOTOR COMPRESSOR (PMC) MODELING

As demonstrated in [61] in order to have efficient air compression process and to have the least required compression work, the compression has to proceed close to isothermal limit. That would imply that the initial temperature at the beginning of the compression process is equal to the final temperature and that all compression heat must be removed during the compression. In ideal case, this can be partially achieved by using multi-stage compression with intercooling between compression stages.

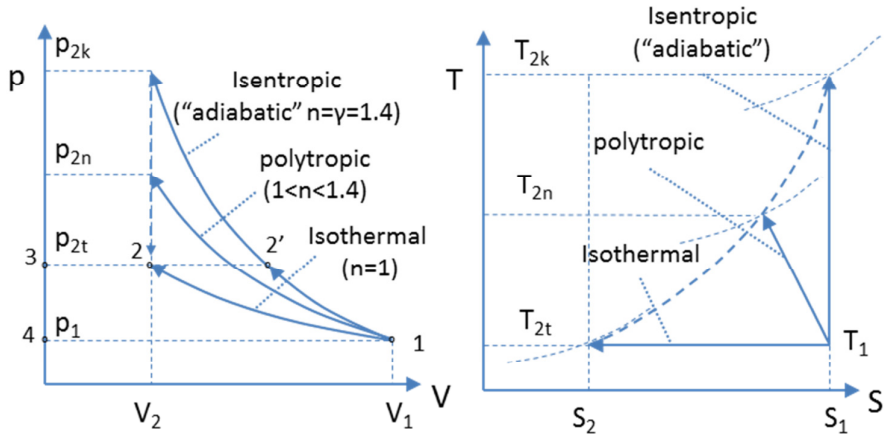

Figure7.2.2.1 – Single Stage Isothermal, polytropic and isentropic compression process [61]

Figure 7.2.2.1 represents isothermal, polytropic and isentropic (adiabatic) compression processes. In the case of isentropic (adiabatic) compression, no heat is exchanged with the environment nor generated internally by friction and in order to reach the same pressure level as isothermal process, the compression has to be followed by isochoric cooling (Figure 7.2.2.1). Further, technical work of compression with respect the same pressure level is higher for isentropic process than isothermal $W_{t12'} > W_{t12}$ (Figure 7.2.2.1). If the gas is being cooled during compression, the polytropic exponent is lower than isentropic (γ =1.4 for air) and entropy during the process reduces.

Figure 7.2.2.2 represents isothermal, polytropic and isentropic (adiabatic) expansion process. As it can be observed, with respect to the same pressure difference, highest technical work can be achieved with isothermal expansion. This would imply, that air temperature is maintained at the same level during the process while the ambient practically behaves as a heat source. In T-s diagram of Figure 7.2.2.2, isothermal process is performed with entropy increase, which implies that the heat is added to the system.

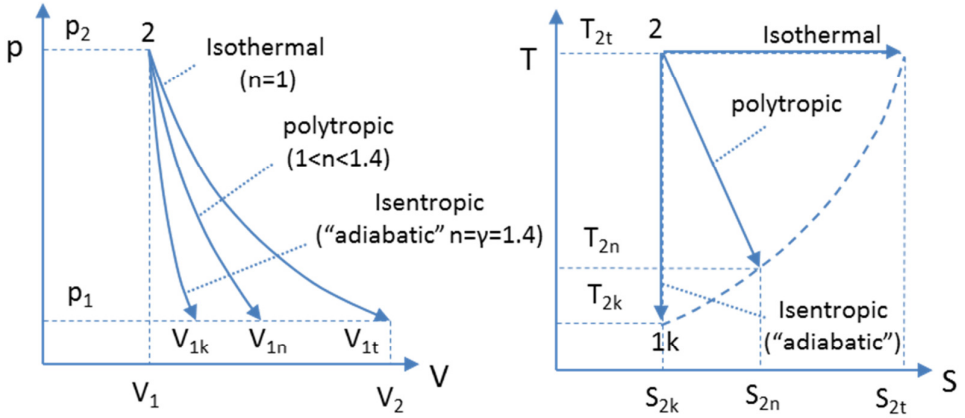

Figure 7.2.2.2 – Single stage isothermal, polytropic and isentropic expansion process [61]

The expansion temperature at the end of the process is lowest in the case of isentropic (adiabatic) process (Figure 7.2.2.2) and this might indicate that technical problems may limit the extraction of mechanical work from compressed air by expansion engines [61].

In reality, most expansions and compressions take place somewhere between isothermal and adiabatic, i.e. polytropic [75] and it can be defined with following equation.

$$p_1 V_1^n = p_2 V_2^n \qquad (7.2.2.1)$$

Temperature at the end of process can be defined as:

$$T_2 = T_1 \cdot \left(\frac{p_2}{p_1}\right)^{\frac{n-1}{n}} \qquad (7.2.2.2)$$

Where $T_1$is the initial temperature and p_1 and p_2 are the initial and final pressures.

Pneumatic Motor Compressor (PMC) used in this application is considered to be reversible variable displacement machine with two compression stages. Under assumption of polytropic compression and expansion processes and knowing the mechanical characteristic of the Pneumatic Motor Compressor, effective power (at the PMC shaft) can be defined with following relation for both first and second stage as:

$$P_{e1} = \bar{\eta}_m \cdot \dot{m}_{air} \cdot R \cdot T_{air1,In} \cdot \frac{n}{n-1}\left(\beta_1^{\frac{n-1}{n}} - 1\right) \qquad (7.2.2.3)$$

And for the second stage:

$$P_{e2} = \bar{\eta}_m \cdot \dot{m}_{air} \cdot R \cdot T_{air2,In} \cdot \frac{n}{n-1}\left(\beta_2^{\frac{n-1}{n}} - 1\right) \qquad (7.2.2.4)$$

Where $\dot{m}_{air}$ is the air mass flow through the compressor [kg/s], $\bar{\eta}_m$ is the mechanical efficiency and β_1 and β_2 are the pressure ratios of separate stages.

Total effective power at PMC crankshaft can be defined as

$$P_e = P_{e1} + P_{e2} \qquad (7.2.2.5)$$

Due to the unavailability of experimental data assumed mechanical efficiency of the PMC is defined in function of shaft speed and is given in the Figure 7.2.2.3. However, for the purpose of building more accurate model in the future work, these values should be confirmed with supplier.

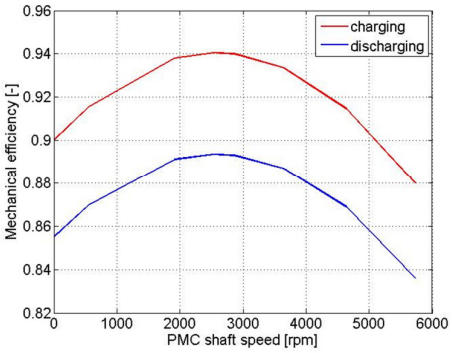

Figure 7.2.2.3 – Mechanical PMC efficiency during charging and discharging

Displacement per revolution [m^3/rev] of the individual PMC stage can be determination with the following relations:

$$D = D_1 + D_2 \qquad (7.2.2.6)$$

$$D_1 = \frac{D}{1 + \frac{1}{\beta_1}} \qquad (7.2.2.7)$$

Where D_1 is the first stage displacement [m^3/rev] and D_2 [dm^3/rev] is the second stage displacement.

Air mass flow of the PMC, having in mind variable displacement characteristic of the system, can be defined as:

$$\dot{m}_{air} = \dot{m}_{air,stage1} = \dot{m}_{air,stage2} \qquad (7.2.2.8)$$

$$\dot{m}_{air} = D_1 \cdot x \cdot n \cdot \eta_v \cdot \rho_1 \qquad (7.2.2.9)$$

Where volumetric efficiency is given in the following equation with some simplifications as:

$$\eta_v = 1 - \frac{D_n}{D_1}\left(\beta_1^{\frac{1}{n}} - 1\right) \qquad (7.2.2.10)$$

Where D_n is the dead volume of the PMC.

Therefore, based on the previous equations air mass flow equation 7.2.2.9 becomes:

$$\dot{m}_{air} = \frac{D}{1 + \frac{1}{\beta_1}} \cdot x \cdot n \cdot \left\{1 - \frac{D_n}{D_1}\left(\beta_1^{\frac{1}{n}} - 1\right)\right\} \cdot \rho_1 \qquad (7.2.2.11)$$

Where x is the displacement factor of the PMC that has values $-1 \leq x \leq 0$ for pneumatic motor mode and $0 \geq x \geq 1$ for compressor mode, n is the speed of the PMC in [rev/s] and ρ_1 is the input air density to the PMC in [kg/m^3].

Following table gives specifications of Pneumatic Motor Compressor used for the purpose of Pneumatic Hybrid Vehicle simulation.

	Unit	Overall PMC	Stage 1	Stage 2
Displacement per revolution D	[dm^3/rev]	2	1.67	0.33
Maximal pressure ratio	[-]	25	5	5
Dead volume	[%]	-	4	4
Weight	[kg]	40	-	-
Max charging power (for SOC_{max} and n_{max})	[kW]	50	-	-
Max discharging power (for SOC_{max} and n_{max})	[kW]	250	-	-

Table 7.2.2.1 – PMC characteristics

Figure 7.2.2.4 represents model layout of Pneumatic Motor Compressor. As mentioned, PMC was modeled as a two stage compression and expansion machine with intercooling between stages. Though detailed intercooler model is present in the system with pressure drop and heat rejection modeled in function of vehicle speed, all the simulations were performed with intercooler block deactivated. Since all the simulations were cycle based and the system was cold at the beginning, the heat generated by the compression process was used in order to warm-up the pneumatic system and to reduce the temperature losses of the charge as will be explained later on.

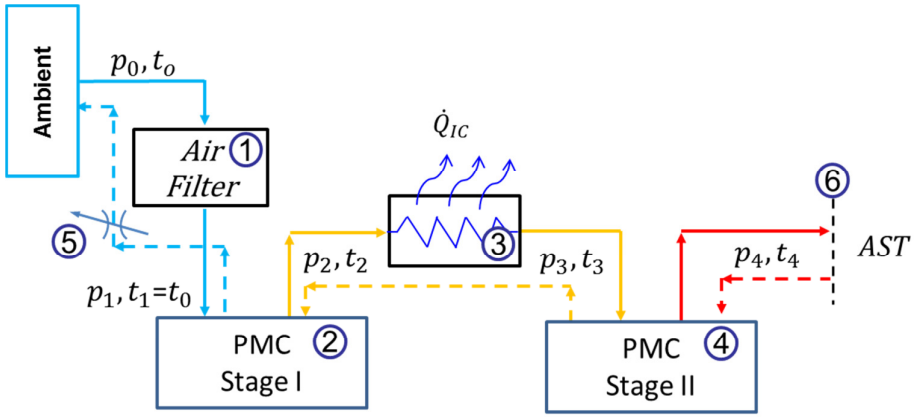

Figure 7.2.2.4 Pneumatic Motor Compressor (PMC) layout – 1) Air filter 2) PMC compression/expansion stage 1, 3) Intercooler 4) PMC compression/expansion stage 2, 5) Back pressure valve (BP) 6 - end section (after this point is attached Air Storage Tank via pneumatic tubes)

As stated in the previous text, extremely low discharging temperature conditions have to be avoided in order to avoid creation of water ice in the expansion machine and the ducts. From the

equation 7.2.2.2 can be seen that during polytropic expansion, temperature at the end of the process depends on the initial temperature, ratio between initial and final pressures as well as polytropic exponent. Since the initial temperature of the air charge during expansion can't be controlled (this would be possible if additional heat exchanger was added to the system), discharge pressure control was implemented into the model. For that reason, the backpressure valve was added downstream (discharge side) of the pneumatic motor (Figure 7.2.2.4 – position 5).

In order to investigate the "off-line" warm-up behavior of the PHV system and the behavior of the backpressure valve, 20 repetitive charging and discharging cycles from minimal to maximal SOC value over 2000s were carried out.

Following Figure represents air pressure [bar] in the Air Storage Tank (AST) during simulation.

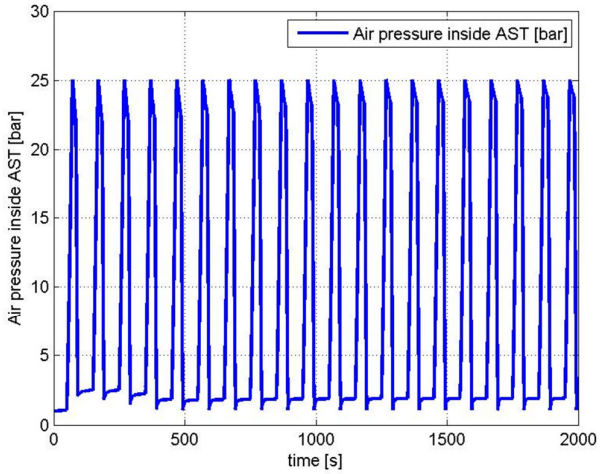

Figure 7.2.2.5 – Pressure [bar] variation in the AST during simulation

Operation of the Backpressure valve BP can be identified in Figure 7.2.2.5. During system warm-up when thermal losses of the air charge are high, BP valve limits backpressure during discharging to higher value with respect to atmospheric pressure in order to maintain the minimal discharging temperature (in case of this simulation minimal discharging temperature is set to 293K). This effect can be seen in Figure 7.2.2.5 from beginning of the simulation up to 500 seconds.

7.2.3 INTERCOOLER AND AIR FILTER MODEL

In order to investigate necessity of intercooling the charge between the stages during compression intercooler was modeled and inserted inside PMC block. Based on [63] intercooler pressure drop losses are given with the following equation:

$$\Delta p_{IC}[kPa] = \frac{\xi R}{2S^2}\frac{T_c \dot{m}^2{}_{air}}{p_c} = k\frac{T_c \dot{m}^2{}_{air}}{p_c} \qquad (7.2.3.1)$$

Where T_c $[°C]$ and p_c $[Pa]$ are the inlet air temperature and pressure and $\dot{m}_{air}$ $[\frac{kg}{h}]$ is the air mass flow. Parameter k can be determined from the [63] as k=8/2.5.

Intercooler efficiency can be explicitly determined on basis of the vehicle speed and it is represented with the following Figure 7.2.3.1 (from [62])

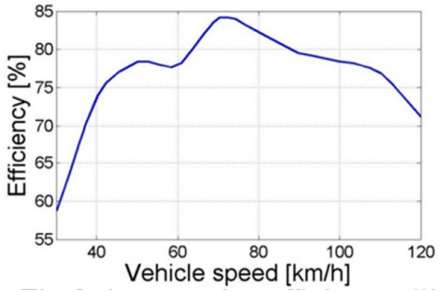

Figure 7.2.3.1 – Intercooler efficiency in function on vehicle speed [62]

Therefore, output temperature of the air charge during intercooling can be determined as:

$$t_{air,Out} = t_{air,\mathrm{In}} - \varepsilon\left(t_{air,\mathrm{In}} - t_{\mathrm{amb}}\right) \qquad (7.2.3.2)$$

Intercooler heat rejection can be defined as:

$$\dot{Q}_{IC} = \dot{m}_{air} c_{p,air}\left(t_{air,\mathrm{In}} - t_{air,Out}\right) \qquad (7.2.3.3)$$

In order to simulate pressure drop due to presence of the air filter in the intake duct, AF model was inserted in the PMC model. Air filter data were taken from [63].

Based on [63] air filter pressure drop losses are given with the following equation:

$$\Delta p_{AF}[kPa] = \frac{\xi R}{2S^2}\frac{T_c \dot{m}^2{}_{air}}{p_c} = k\frac{T_c \dot{m}^2{}_{air}}{p_c} \qquad (7.2.3.4)$$

Where T_c $[°C]$ and p_c $[Pa]$ are the inlet air temperature and pressure and $\dot{m}_{air}$ $[\frac{kg}{h}]$ is the air mass flow. Parameter k can be determined from the [63] as k=4/3.

7.2.4 AIR STORAGE TANK (AST)

7.2.4.1 AIR STORAGE TANK MODELING WITH EXHAUST GAS RECUPERATION

This block represents thermo-dynamical (physical) model of the air storage system with exhaust gas heat recuperation. It determines thermodynamic states (temperature and pressure) of the air inside AST taking into account thermal inertia of the system and losses (heat and pressure drop losses (concentrated/distributed) of the AST and the connecting lines (tubes between PMC and AST)).

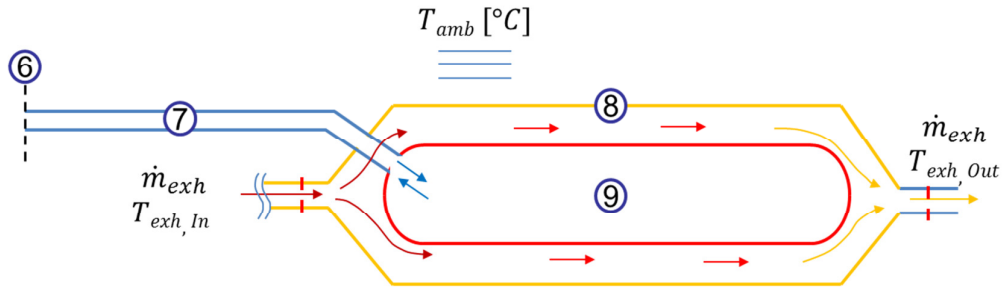

Figure 7.2.4.1.1: 6- entry section (before this point is connected PMC – Figure 7.2.2.4) 7- pneumatic lines (tubes) 8-external exhaust tube wall 9-Air Storage Tank

As an effort to improve the efficiency of the pneumatic system during operation, Air Storage Tank (AST) is conveniently positioned inside the exhaust line downstream the vehicle catalyst. Charge air (Figure 7.2.4.1.1– position 9) is contained inside constant volume vessel and surrounded by exhaust gas. Exhaust gas is separated from the environment by the exhaust tube wall (Figure 7.2.4.1.1– position 8). In that manner, air heat losses during operation should be reduced i.e. exhaust gas should provide the insulation effect, while in the case of lower air AST temperatures (expansion operation), heat should be transferred to the air in the AST, thus increasing its internal energy (and system efficiency).

In order to precisely define geometrical properties, CAD model was created of the AST system.

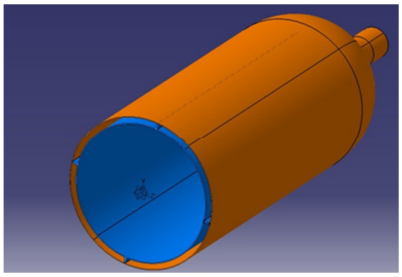

Figure 7.2.4.1.2 – AST with exhaust gas recuperation – lateral cross section view

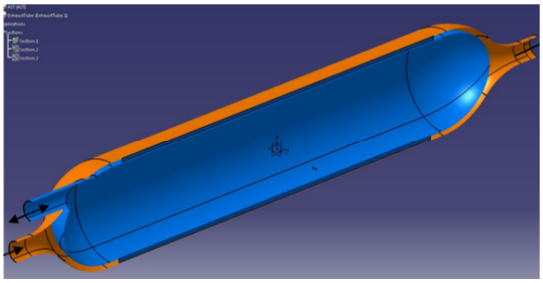

Figure 7.2.4.1.3 – AST with exhaust gas recuperation – longitudinal cross section view

Geometrical and physical characteristics of the AST system are disclosed in the following Table 7.2.4.1.1.

item		AST internal wall	Exhaust line wall
Dimensions	[mm]	Ø240x1240	Ø262x1475
material		Steel AISI302	Steel AISI302
weight	[kg]	12.58	10.7
volume	[dm^3]	54	65
Surface area	[m^2]	1.05	1.105
thickness	[mm]	1.5	1.2
Material density	[kg/m^3]	8055	8055
Mean thermal capacity	[J/kgK]	510	510
emissivity	[-]	0.6	0.1

Table 7.2.4.1.1 Geometrical and physical properties of the AST system

In order to give detailed explanation of the thermodynamic model of compressed air inside AST and the heat fluxes inside the system, the whole systems was divided into 6 zones and each of them is described individually.

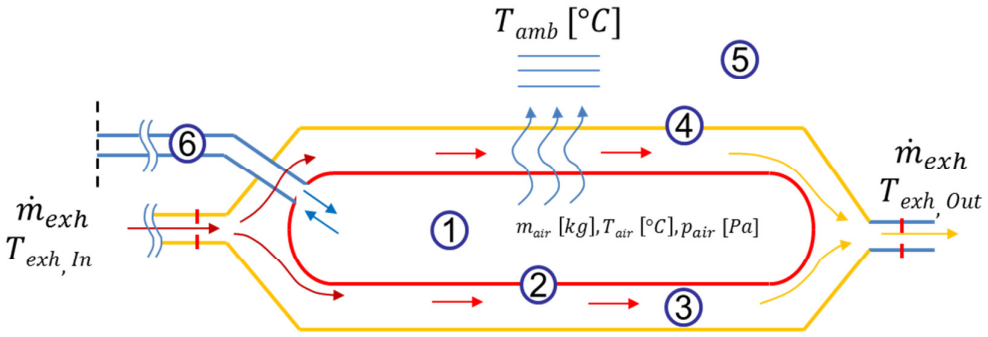

Figure 7.2.4.1.4 – Air Storage Tank (AST) with exhaust gas recuperation divided into 6 characteristic zones 1) Compressed air charge 2) AST wall 3) Exhaust gas flow 4) Exhaust line wall 5) Ambient 6) Pneumatic lines (tubes)

Zone 1- Air Storage Tank

On basis of general energy equation, air temperature inside the AST can be defined as:

$$\frac{dT_{air}}{dt} = \frac{-\dot{Q}_{1,conv} + \dot{m}_{air,IN} c_p T_{air,IN} - c_v T_{air} \frac{dm_{air}}{dt}}{m_{air} c_v} \qquad (7.2.4.1.1)$$

Where heat exchange between air in the AST (Figure 7.2.4.1.4- position 1) and the AST wall (Figure 7.2.4.1.4- position 2) can be defined as:

$$\dot{Q}_{1,conv} = h_1 S_1 (T_{air} - T_2) \qquad (7.2.4.1.2)$$

Where h_1 is the heat convection coefficient [W/m^2K], S_1 the surfaced area [m^2] of the AST wall and T_2 is the AST wall mean temperature.
Air mass trapped inside the AST has been calculated as follows:

$$m_{air} = \int \dot{m}_{air,IN}\, dt \qquad (7.2.4.1.3)$$

Heat convection coefficient criteria equations [76] have been implemented into the simulation in order to calculate the corresponding heat convection coefficients in all AST zones and in the general case heat convection coefficient can be defined as:

$$h = \frac{k \cdot N_{u_D}}{D_h} \qquad (7.2.4.1.4)$$

where k is the thermal conductivity, D_h is the hydraulic diameter and N_{u_D} is the Nusselt number. In the case of laminar flow, the influence coefficients can be obtained from Tables 8.2, 8.3 [76].
For a fully developed turbulent flow the influence coefficients are a function of the Reynolds and Prandtl numbers. However, to a first approximation the inner and outer convection coefficients may be assumed to be equal, and they may be evaluated using the hydraulic diameter

$$\mathrm{D_h} = \mathrm{D_o} - \mathrm{D_i} \qquad (7.2.4.1.5)$$

and Dittus – Boeler equation

$$\mathrm{Nu_D} = 0.023\mathrm{Re_D^{4/5}P_r^n} \qquad (7.2.4.1.6)$$

For $R_{eD} \geq 10000$, $0.6 \leq P_r \leq 160$ and (L/D) ≥ 10

Also in the case of fully developed turbulent flow, Nusselt number can be defined as:

$$\mathrm{Nu_D} = \frac{(\mathrm{f}/8)(\mathrm{Re_D} - 1000)\mathrm{P_r}}{1 + 12.7\left(\frac{\mathrm{f}}{8}\right)^{\frac{1}{2}}(\mathrm{P_r}^{\frac{2}{3}} - 1)} \qquad (7.2.4.1.7)$$

For $3000 \leq R_{eD} \leq 5 \cdot 10^6$, $0.5 \leq P_r \leq 2000$ and (L/D) ≥ 10

Where

$$\mathrm{f} = (0.79\ln\mathrm{Re_D} - 1.64)^{-2} \qquad (7.2.4.1.8)$$

AST model also considers concentrated pressure drop losses of the air entering and exiting the AST. Concentrated losses in [Pa] are modeled using the following relations for the case when the air is entering the AST volume:

$$\Delta p_{chg} = \xi_{chg}\rho_{air}\frac{v_{air}^2}{2} \qquad (7.2.4.1.9)$$

Where $\xi_{chg} = 1$

And for the case when air is exiting the AST volume:

$$\Delta p_{dis} = \xi_{dis}\rho_{air}\frac{v_{air}^2}{2} \qquad (7.2.4.1.10)$$

Where $\xi_{dis} = 0.5\left(1 - \frac{A_2}{A_1}\right)$ and A_1 and A_2 are the cross section areas of pneumatic line and AST tank respectively.

Zone 2- Air Storage Tank (AST) wall (Figure 7.2.4.1.4 position 2)

Thermal inertia of the wall has been introduced in order to simulate the wall behavior during transitory conditions (warm-up). Mean wall temperature has been defined as:

$$\frac{dT_2}{dt} = \frac{\dot{Q}_{1,conv} - \dot{Q}_{2,conv} - \dot{Q}_{2-4,rad}}{m_2 c_2} \qquad (7.2.4.1.11)$$

Where heat power flows from/to the wall can be defined as:

$\dot{Q}_{1,conv}$ – defined previously (zone 1)

$$\dot{Q}_{2,conv} = h_2 S_1 \left(T_2 - T_{Exh,Mean}\right) \qquad (7.2.4.1.12)$$

Where h_2 is heat convection coefficient between wall and the exhaust gas and $T_{Exh,Mean}$ (Figure 7.2.4.1.4 position 3) is the mean exhaust gas temperature between AST wall and exhaust line wall. $\dot{Q}_{2-4,rad}$ represents thermal power exchanged between AST wall and exhaust line wall by radiation, and it can be defined as:

$$\dot{Q}_{2-4,rad} = \sigma \varepsilon_{24} ({T^4}_2 - {T^4}_4) \qquad (7.2.4.1.13)$$

Where ε_{12} is the mean emissivity between two walls and it can be expressed as

$$\varepsilon_{24} = \frac{1}{\frac{1}{\varepsilon_2} + \frac{S_2}{S_4}\left(\frac{1}{\varepsilon_4} - 1\right)} \qquad (7.2.4.1.14)$$

Where ε_2, ε_4 are individual emissivity of the AST wall and exhaust line wall respectively.

Zone 3 - Exhaust gas mean temperature (Figure 7.2.4.1.4 position 4)

Mean temperature of the exhaust gas trapped between AST wall and exhaust line wall can be determined as:

$$\frac{dT_{Exh,Mean}}{dt} = \frac{\dot{m}_{Exh} c_{p,Exh,In} T_{Exh,In} - \dot{m}_{Exh} c_{p,Exh,Out} T_{Exh,Out} + \dot{Q}_{2,conv} - \dot{Q}_{3,conv}}{m_{Exh} c_{v_{Exh,Mean}}} \qquad (7.2.4.1.15)$$

Where $\dot{Q}_{3,conv}$ is the heat flux due to convection from the exhaust gas to the exhaust line wall and it can be defined as:

$$\dot{Q}_{3,conv} = h_3 S_2 \left(T_{Exh,Mean} - T_2\right) \qquad (7.2.4.1.16)$$

Where h_3 [W/m^{2}K] is heat convection coefficient and S_2 [m^2] is the exhaust line wall surface area.

Coefficient of recuperation in introduced in order to define the quality of exhaust gas heat recuperation.

$$\varepsilon \cong \frac{T_{Exh,In} - T_{Exh,Out}}{T_{Exh,In} - T_{amb}} \qquad (7.2.4.1.17)$$

Zone 4- Exhaust line wall (Figure 7.2.4.1.4 position 4)

Thermal inertia of the wall has been introduced in order to simulate the exhaust line wall behavior during transitory conditions (warm-up). Mean wall temperature has been defined as:

$$\frac{dT_4}{dt} = \frac{\dot{Q}_{3,conv} + \dot{Q}_{2-4,rad} - \dot{Q}_{4,conv} - \dot{Q}_{4,rad}}{m_4 c_4} \qquad (7.2.4.1.18)$$

Where heat convection from the wall to the ambient is defined as:

$$\dot{Q}_{4,conv} = h_4 S_2 (T_4 - T_{amb}) \qquad (7.2.4.1.19)$$

h_4 is heat convection coefficient between wall and the ambient air and T_4 is the mean wall temperature. $\dot{Q}_{4,rad}$ represents thermal power lost due to the radiation from the external wall surface to the ambient and it is defined as:

$$\dot{Q}_{4,rad} = \sigma \varepsilon_{4amb} (T^4{}_4 - T^4{}_{amb}) \qquad (7.2.4.1.20)$$

where ε_{4amb} is the mean emissivity between wall and the ambient and it can be expressed as:

$$\varepsilon_{4amb} = \frac{1}{\frac{1}{\varepsilon_4} + \frac{S_4}{S_{amb}}\left(\frac{1}{\varepsilon_{amb}} - 1\right)} \qquad (7.2.4.1.21)$$

and since $S_{amb} \to \infty$, $\varepsilon_{4amb} = \varepsilon_4$ where ε_4 is the individual emissivity of exhaust line wall.

Zone 5- Ambient air (Figure 7.2.4.1.4 position 5)

It is considered that ambient air is at standstill (v_{amb}=0 m/s) with following thermo dynamical characteristics:

$p_{amb}=10^5$ Pa, T_{amb}=293 K

Zone 6- Connecting lines (tubes) (Figure 7.2.4.1.4 position 6)

Pneumatic Motor Compressor and Air Storage Tank are connected by high pressure pneumatic tube (Figure 7.2.4.1.4 position 6). Transport losses between PMC and AST have been modeled in terms of pressure drop as well as heat loss from charged air to the environment.

Tube characteristics are given in Table 2.3.2.

material			Rubber
length	L	[m]	1.5
Internal diameter	D	[mm]	50
Wall thickness	a	[mm]	10
emissivity	ε_{tube}	[-]	0.1
Thermal conductivity	λ	[W/mK]	0.8

Table 7.2.4.1.2 Pneumatic line (tube) characteristics

Distributed losses of the tubes in [Pa] are modeled using the following equations:

$$\Delta p_{lines} = \lambda \cdot \rho_{air,mean} \frac{L}{D} \frac{v_{air,mean}^2}{2} \qquad (7.2.4.1.22)$$

Where λ is defined in function of the Reynolds number as:

$$\lambda = \frac{64}{R_e} \qquad (7.2.4.1.23)$$

In the case of laminar flow conditions ($R_e < 2300$) and in the case of turbulent flow conditions for ($R_e > 2300$):

$$\lambda = \frac{0.316}{R_e^{0.25}} \qquad (7.2.4.1.24)$$

Heat losses due to convection are defined by global heat exchange coefficient as:

$$\dot{Q}_{tube,conv} = h_{tube} S_{tube} \left(T_{air,tube} - T_{amb}\right) \qquad (7.2.4.1.25)$$

Global heat exchange coefficient h_{tube} between compressed air and ambient is defined as:

$$h_{tube} = \frac{1}{\frac{1}{h_{tube,1}} + \frac{a}{\lambda} + \frac{1}{h_{tube,2}}} \qquad (7.2.4.1.26)$$

Where $h_{tube,1}$ and $h_{tube,2}$ are heat convection coefficients from the air to the tube wall and from the tube wall to the ambient respectively. The λ is the wall thermal conductivity and a is wall thickness.

Mean tube wall temperature is determined in the following manner disregarding the wall thickness as:

$$T_{tube} = \frac{h_{tube,1} T_{air} + h_{tube,2} T_{amb}}{h_{tube,1} + h_{tube,2}} \qquad (7.2.4.1.27)$$

Heat losses from tube wall to the ambient due to radiation are expressed with the following relation:

$$\dot{Q}_{tube,rad} = \sigma \varepsilon_{tube-amb} (T^4{}_{tube} - T^4{}_{amb}) \qquad (7.2.4.1.28)$$

Where $\varepsilon_{tube-amb}$ is the mean emissivity between tube wall and ambient and it can be expressed as:

$$\varepsilon_{tube-amb} = \frac{1}{\frac{1}{\varepsilon_{tube}} + \frac{S_{tube}}{S_{amb}} \left(\frac{1}{\varepsilon_{amb}} - 1\right)} \qquad (7.2.4.1.29)$$

And since $S_{amb} \rightarrow \infty$, $\varepsilon_{tube-amb} = \varepsilon_{tube}$

7.2.4.2 PRESSURE BASED DETERMINATION OF STATE OF CHARGE (SOC)

Relative internal energy of the air trapped inside the AST in function of its temperature and mass can be defined as:

$$U_{AST} = c_v\left(m_{air}(t)T_{air}(t) - m_{air,init}T_{air,init}\right) \qquad (7.2.4.2.1)$$

Where c_v is the specific heat capacity of air under constant volume.

As a first approach, State of Charge (SOC) of the system can be determined as the ratio between available and maximal internal energy stored inside the AST.

$$\mathrm{SOC(t)} = \frac{\mathrm{U(t)}}{\mathrm{U_{max}}} \qquad (7.2.4.2.2)$$

$$\mathrm{SOC(t)} = \frac{\mathrm{m_{air}(t)c_{v,air}T_{air}(t)}}{max\{\mathrm{m_{air}c_{v,air}T_{air}}\}} \qquad (7.2.4.2.3)$$

Where:

$$\mathrm{p_{air}(t)\cdot V = m_{air}(t)\cdot R\cdot T_{air}(t)} \qquad (7.2.4.2.4)$$

$$\mathrm{p_{air,max}(t)\cdot V = m_{air,max}(t)\cdot R\cdot T_{air,max}(t)} \qquad (7.2.4.2.5)$$

Therefore after substitution of the equations it can be stated that SOC during operation can be defined only in function of the pressure of the AST system.

$$\mathrm{SOC(t)} = \frac{\frac{\mathrm{p_{air}(t)\cdot V}}{\mathrm{R}}\cdot \mathrm{c_{v,air}}}{max\ \{\frac{\mathrm{p_{air}(t)\cdot V}}{\mathrm{R}}\cdot \mathrm{c_{v,air}}\}} = \frac{\mathrm{p_{air}(t)}}{\mathrm{p_{air,max}}} \qquad (7.2.4.2.6)$$

For the purpose of this analysis the maximal and minimal pressure limits of the AST system are defined as:

$$\mathrm{SOC_{min}(p_{air} = 1bar) = 0\ [\%]\ \ and\ \ SOC_{max}(p_{air} = 25bar) = 100[\%]}$$

In the first approach the SOC of the systems can be defined only in the function of the air pressure. Due to simplicity of the considerations, storage tank should be equipped only with pressure gauge that would monitor the pressure level in order to determine the State of Charge of the system. However, according to the equation of state, same pressure level of the compressed air can be reached either by increasing the air mass during isothermal process or by adding the heat to the air charge while maintaining the air mass inside charge vessel constant. This would lead to analysis of the quality of stored energy inside the storage tank i.e. its availability to do work. This availability of compressed air to do work is named exergy and is evaluated in the following chapter.

7.2.4.3 EXERGY BASED DETERMINATION OF THE STATE OF CHARGE (SOC)

Exergy is defined as the maximal useful work that can be obtained from the system with respect to the given reference state without generalized friction [65]. During the process, according to the first law of thermodynamics, energy is never destroyed but it changes from one form to another. However, availability to do the work is lost due to irreversibility of the process and this loss is proportional to the entropy increase of the system (second law of thermodynamics). Once the system reaches equilibrium with the reference state (i.e. environment) the exergy becomes zero.

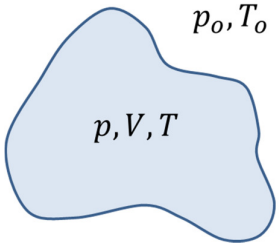

Figure 7.2.4.3.1 - The compressed air control volume (air storage tank) in mechanical and thermal imbalance with the reference state (environment)

In the most general approach (neglecting potential and kinetic energy), exergy of the stored compressed air (Figure 7.2.4.3.1) can be defined with the following relation as [65, 66]:

$$W_{max} = \Delta U - T_0 \Delta S + p_0 \Delta V \qquad (7.2.4.3.1)$$

Where T_0 *and* p_0 are the pressure and temperature of the reference state (ambient). If the compressed air is treated as an ideal gas the equation (7.2.4.3.1) can be given as:

$$W_{max} = m\left[c_v(T_1 - T_0) + T_0\left(c_p ln\frac{T_0}{T_1} - R_g ln\frac{p_0}{p_1}\right) + p_0(v_1 - v_0)\right] \qquad (7.2.4.3.2)$$

Where m is the mass of the compressed air and T_1 *and* p_1 is the temperature and pressure of the compressed air respectively. Specific volumes can be defined from equation of state as

$$v_1 = \frac{RT_1}{p_1} \qquad (7.2.4.3.3)$$

And

$$v_0 = \frac{RT_0}{p_0} \qquad (7.2.4.3.4)$$

Where R is the gas constant of the air.

If the compressed air is in the thermal equilibrium with the environment [66], specific exergy expression can be simplified and defined only in function of air pressure as:

$$w_{max} = RT_0\left[\left(\frac{p_0}{p_1} - 1\right) + ln\frac{p_1}{p_0}\right] \qquad (7.2.4.3.5)$$

In the case of Pneumatic Hybrid Storage System analyzed in this work, thermal as well as pressure imbalance has to be taken into account (equation 7.2.4.3.2).

Based on the previous equations, maximal work (exergy) can be represented in function of mass and temperature of the air inside tank (i.e. AST) with the following figure:

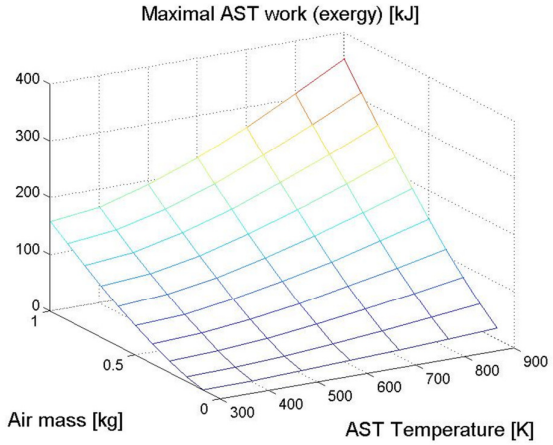

Figure 7.2.4.3.2– Maximal work (exergy) of compressed air stored in 54 lit tank (AST)

Maximal pressure of the air stored in the Air Storage Tank (AST) has to be defined in function of the permissible stress of the tank material. For the purpose of this analysis, maximal tank pressure was limited to 25 bar. Figure 7.2.4.3.3 represents contours of air pressure and exergy in function of air temperature and mass inside the air storage tank. Intersection of the maximal pressure (dashed blue line that corresponds to constant pressure of 25 bar) with exergy contours gives maximal exergy of the stored air in function of its temperature.

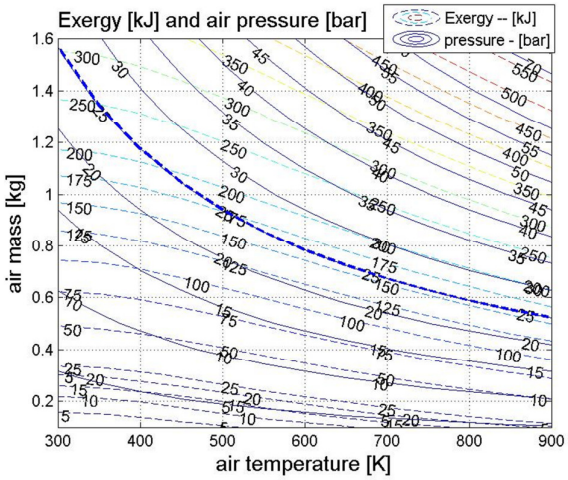

Figure 7.2.4.3.3– Maximal work (exergy) of compressed air stored in 54 lit tank (dashed lines) and pressure levels (continuous lines). Dashed thick blue line represent max pressure contour (25bar).

State of charge based on pressure can be defined as

$$\mathrm{SOC} = \frac{\mathrm{p_{air}}}{\mathrm{p_{air,max}}}$$

(As explained in the chapter 7.2.4.2 equation 7.2.4.2.6).

State of charge based on exergy can be defined as a ratio between exergy for the current temperature and pressure and maximal exergy (for maximal pressure) in the Air Storage Tank (AST) as:

$$SOC = \frac{W_{max}(p,T)}{W_{max}(p_{max},T)} \qquad (7.2.4.3.6)$$

After substituting with equation (7.2.4.3.2), SOC equation becomes

$$SOC = \frac{m\left[c_v(T_1 - T_0) + T_0\left(c_p ln\frac{T_o}{T_1} - R_g ln\frac{p_o}{p_1}\right) + p_0(v_1 - v_0)\right]}{m_{max}\left[c_v(T_1 - T_0) + T_0\left(c_p ln\frac{T_o}{T_1} - R_g ln\frac{p_o}{p_{max}}\right) + p_0(v_{max} - v_0)\right]} \qquad (7.2.4.3.7)$$

Where air mass and specific volume can be determined in function of temperature and maximal pressure as:

$$m_{max} = \frac{p_{max}V}{RT} \qquad (7.2.4.3.8)$$

$$v_{max} = \frac{RT}{p_{max}} = \frac{V}{m_{max}} \qquad (7.2.4.3.9)$$

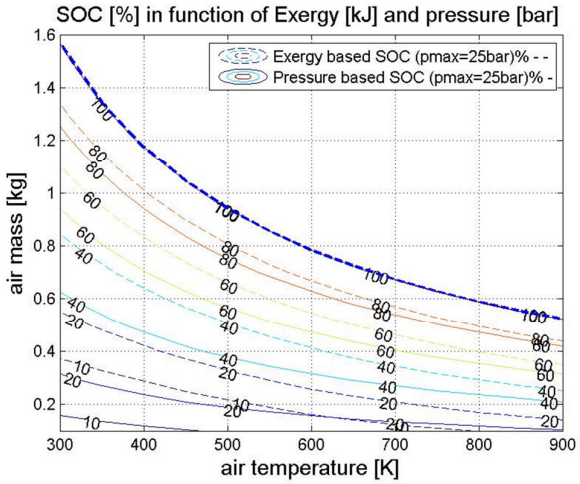

Figure 7.2.4.3.4– State of Charge (SOC) defined in function of maximal work - exergy (dashed lines) and pressure in the AST (continuous line).

Based on figure 7.2.4.3.4 it can be noted that SOC lines for pressure and exergy based SOC lines have parallel trends. However, pressure based SOC lines state higher energy availability with respect to exergy based SOC.

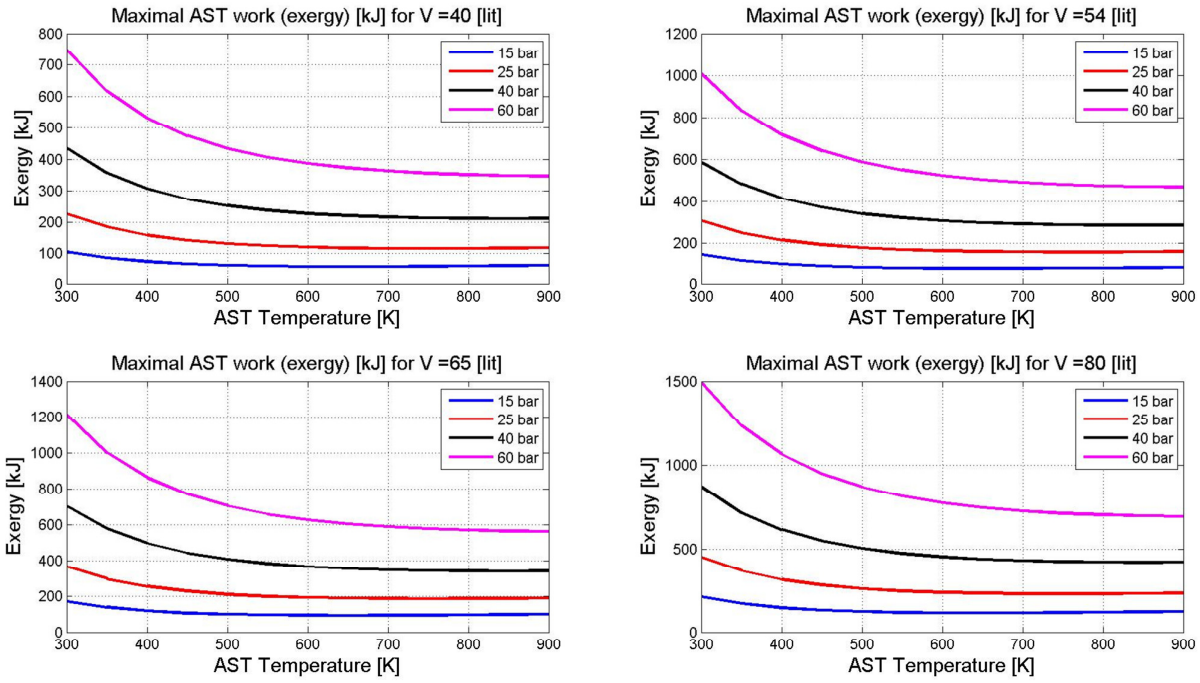

Figure 7.2.4.3.5– Maximal work - exergy variation in function of air pressure [bar] and temperature [K] for different storage tank volumes

Figure 7.2.4.3.5 represents exergy of the stored air in the AST in function of different pressure levels and storage tank volumes.

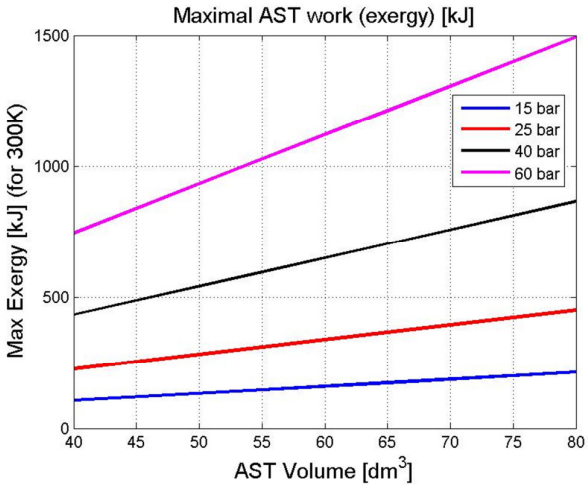

Figure 7.2.4.3.6 – Maximal exergy (for 300 K) in function of AST volume and for different pressure levels.

7.2.5 GLOBAL CHARGING AND DISCHARGING EFFICIENCY - “OFFLINE” ANALYSIS

Detailed efficiency analysis of the pneumatic powertrain part was carried out during charging and discharging process. The analysis determined instantaneous efficiency of the whole pneumatic system and took into account losses described in the previous chapters. Charging and discharging efficiency maps were created as well as effective (at the PMC shaft) power that systems can develop and are presented in Appendix I.
The efficiency analysis was carried out in function of several operational parameters:

1. Pneumatic Motor Compressor (PMC) shaft speed
2. Air Storage Tank (AST) state of charge value
3. Displacement factor x of the PMC
4. Mean AST wall temperature

All efficiency maps were created in “off-line” mode, i.e. pneumatic system was decoupled from the vehicle driveline. Later the efficiency data was introduced as 4-D maps into Pneumatic Hybrid Vehicle (PHV) simulation.

It should be noted that efficiency results represent only instantaneous efficiency and don’t include the energy “drain” losses when the system is not in use. There losses would manifest themselves as thermal losses of the compressed air charge versus ambient when the temperature of the compressed air is higher than ambient temperature.

7.3 SIMULATION RESULTS DURING NEDC CYCLE

7.3.1 PHV WITH EXHAUST GAS RECUPERATION IN THE AST

Following chapter represents extract of the simulation results for NEDC cycle for Pneumatic Hybrid Vehicle. Figure 7.3.1.1 demonstrates variation of the State of Charge (SOC) of the system during the cycle, where initial SOC value is equal to the final SOC value.

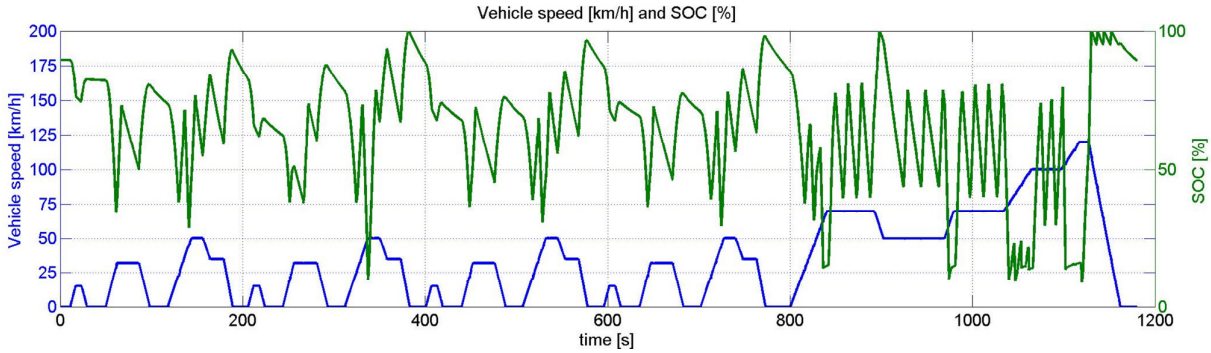

Figure 7.3.1.1 NEDC cycle

Adaptable control strategy operation results in charge sustaining cycle operation over whole cycle, even with high SOC variation that are present due to extremely limited energy storage capacity of the AST system. Also, relatively high percentage of SOC loss can be observed during the instances when the vehicle is at standstill. It should be mentioned, that maximal SOC value (100%) corresponds to the air pressure inside AST of 25 bars.

Figures 7.3.1.2, 7.3.1.3 and 7.3.1.4 represent the behavior of the Air Storage System during the cycle. Figure 7.3.1.2 represents temperatures of the AST wall (Figure 7.2.4.1.4 – position 2), Exhaust line wall (Figure 7.2.4.1.4 – position 4) and Mean exhaust gas temperature (Figure 7.2.4.1.4 – position 3). At the beginning of the cycle, all components are at the same temperatures (cold start conditions). The thermal state of the AST system begins to increase due to the heat released by the compression of the air inside AST and flow of the exhaust gas when the engine is turned on. During the instances of the cycle when the engine is turned off and vehicle is in pneumatic traction, the mean exhaust gas temperature is determined by mean temperatures of AST wall and Exhaust line wall since there are no hot exhaust gasses present in the AST system.

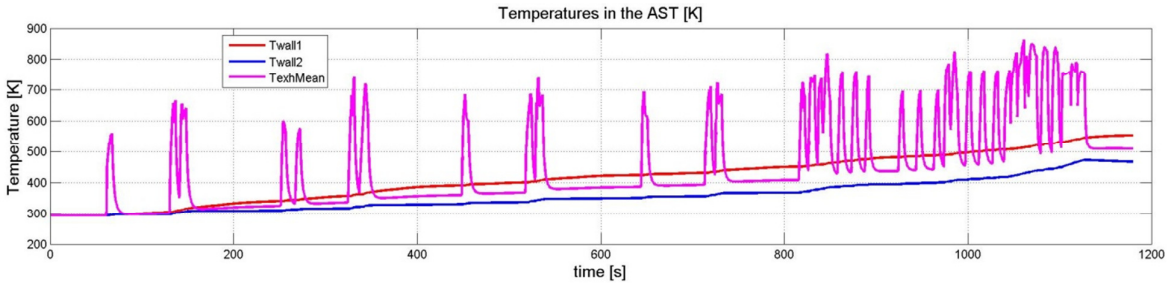

Figure 7.3.1.2 NEDC cycle

Figure 7.3.1.3 represents thermal power exchanged between compressed air inside AST and the AST wall (Figure 7.2.4.1.4 – Zone 1 & Equation (7.2.4.1.2)) where positive values represent thermal power loss from the air charge. As it can be observed, relatively high thermal losses are present and they can be related to system warm-up and the heat dissipated to the ambient. Negative power values represent recuperation benefit of the system.

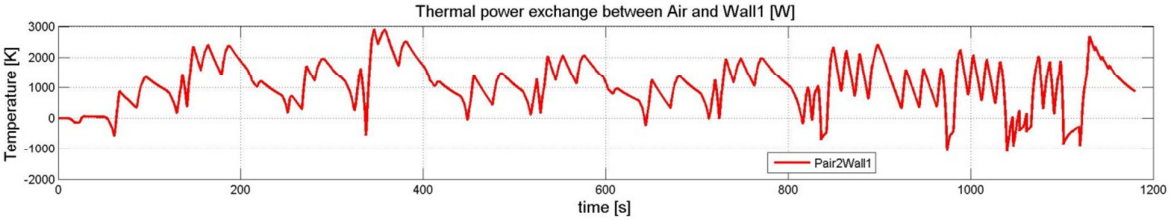

Figure 7.3.1.3 Thermal power exchanged between air charge and the wall during NEDC cycle

Figure 7.3.1.4 represents temperature trends of the compressed air inside AST and the mean exhaust gas temperature. Negative temperature values of the air inside AST can be observed briefly at the beginning of cycle.

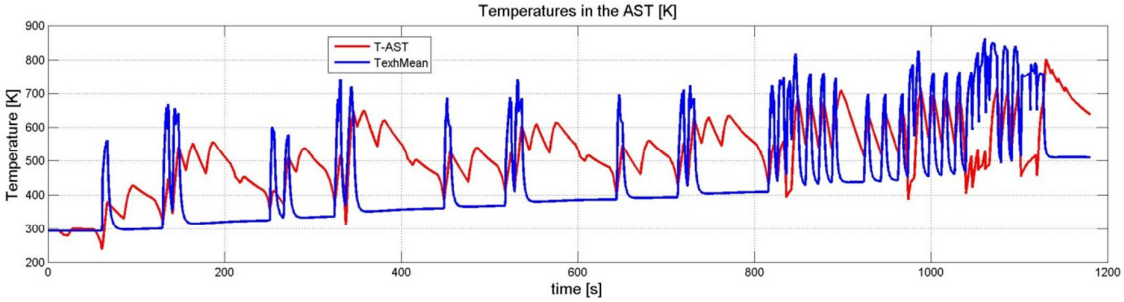

Figure 7.3.1.4 Air charge and exhaust gas temperature inside the AST during NEDC cycle

Following figures represent histograms of engine efficiency, charging and discharging efficiency and PMC displacement factor during NEDC cycle. As it can be seen from Figure 7.3.1.5, due to the ECMS strategy engine operates in the zone of highest efficiency throughout the cycle. Charging

and discharging efficiency histograms are related to global efficiency of the pneumatic part of the powertrain that include PMC and AST with exhaust heat recuperation (detailed efficiency for charging and discharging can be found in Appendix I).

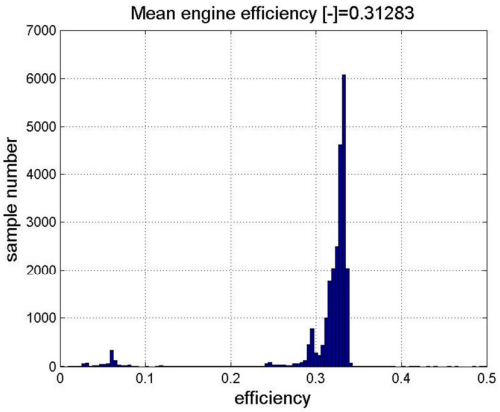

Figure 7.3.1.5 Engine efficiency

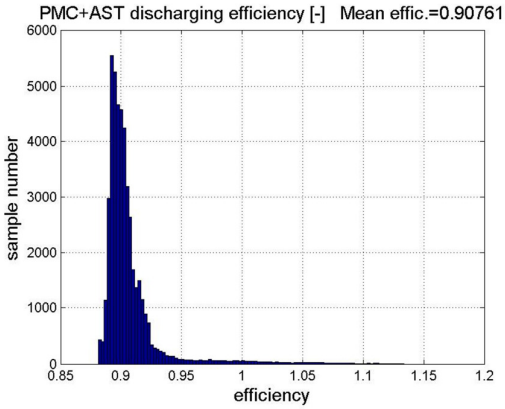

Figure 7.3.1.7 Discharging efficiency of the PHV system

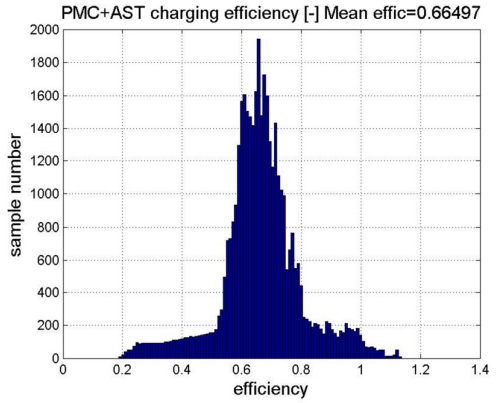

Figure 7.3.1.6 Charging efficiency of the PHV system

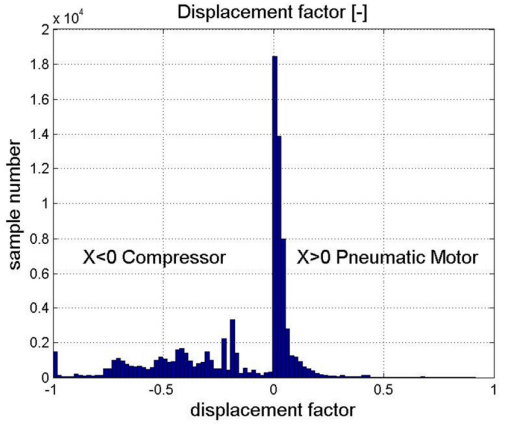

Figure 7.3.1.8 Displacement factor of the PMC

Figure 7.3.1.8 represents histogram of the displacement factor x of the Pneumatic Motor Compressor (PMC). As it can be observed pneumatic motor operates with low displacement factor values during cycle since the discharging process always begins with relatively high SOC values (high air pressure inside the AST). Therefore, on basis of the required power, low air mass flow is required (and therefore low displacement value).

Figure 7.3.1.9 gives detailed analysis of the energy fluxes inside the whole pneumatic hybrid vehicle during NEDC cycle. Due to the control strategy operation and load point shift, mean engine efficiency over the cycle has been increased from 23.8 (Figure 2.4.4) to 31.1 %. Relatively high mechanical braking energy is present (644 kJ) due to very limited energy storage capacity of the PHV system. Mean pneumatic hybrid efficiency (position 2) is defined as ratio between mechanical energy output during discharging (at the PMC shaft) and sum of mechanical energies input during charging of the system and is relatively low (around 60%) when compared to other analyzed hybrid systems. However high percentage of engine energy that is used for recharging is present (43%) and this can be contributed to highly dissipative storage system that has small energy storage capacity and requires frequent recharging.

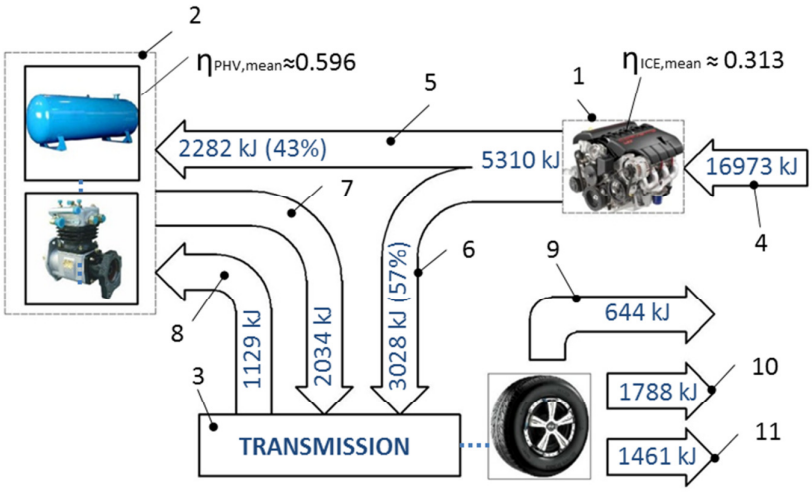

Figure 7.3.1.9 – Energetic analysis for PHV with exhaust gas recuperation during NEDC (all energies are referred to the primary AMT shaft axis): 1-Internal Combustion Engine 2-Hybrid powertrain part (Pneumatic Motor Compressor PMC, Air Storage Tank (AST) with exhaust gas recuperation) 3- Vehicle transmission 4- Fuel energy consumed during the cycle 5-Direct recharging energy from ICE to the PMC 6-Direct traction energy (from the ICE to the transmission) 7-Hybrid traction energy (from the hybrid system to the transmission) 8-Regenerative braking energy (from the transmission to the hybrid system) 9-Mechanical braking energy 10-Aerodynamic resistance energy 11-Rolling resistance energy

Figure 7.3.1.10 represent distribution in [s] of the engine operating points during NEDC cycle. Independently of the cycle power demand, engine operates always in the zone of the high efficiency.

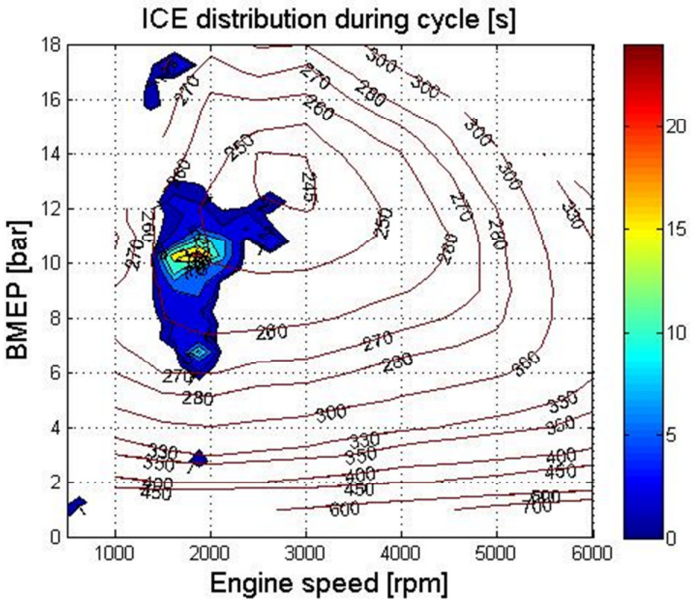

Figure 7.3.1.10 – ICE operating points during NEDC cycle

In order to investigate the influence of the exhaust gas recuperation system on the cycle fuel economy and energetic efficiency, two additional simulation cases were explored and they will be described in the following chapters.

7.3.2 PHV W/O EXHAUST GAS RECUPERATION IN THE AST – CASE 1

This simulation case was performed in order to determine the benefit of exhaust gas recuperation system. AST system presented in Figure 7.2.4.1.4 was modified and the secondary exhaust line wall was removed, placing the AST wall in direct contact with the ambient. Figure 7.3.2.1 represents modified AST modes.

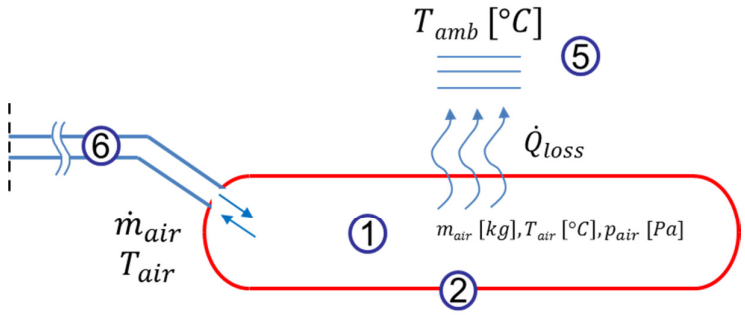

Figure 7.3.2.1 – Air Storage Tank (AST) w/o exhaust gas recuperation
1) Compressed air charge 2) AST wall 5) Ambient 6) Pneumatic lines (tubes)

Figure 7.3.2.2 represents energetic fluxes and efficiency analysis of the PHV vehicle without exhaust gas recuperation.

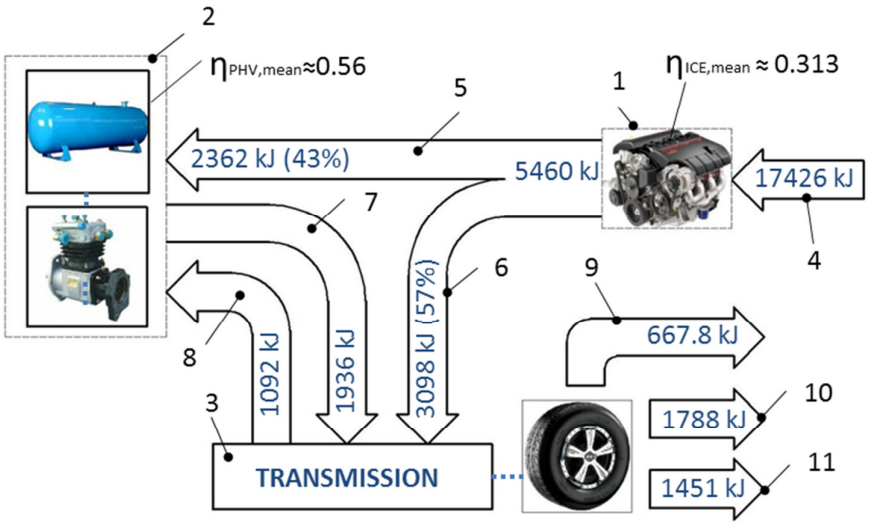

Figure 7.3.2.2 – Energetic analysis for PHV w/o exhaust gas recuperation during NEDC cycle (all energies are referred to the primary AMT shaft axis): 1-Internal Combustion Engine 2-Hybrid powertrain part (Pneumatic Motor Compressor PMC, Air Storage Tank (AST) with exhaust gas recuperation) 3- Vehicle transmission 4- Fuel energy consumed during the cycle 5-Direct recharging energy from ICE to the PMC 6-Direct traction energy (from the ICE to the transmission) 7-Hybrid traction energy (from the hybrid system to the transmission) 8-Regenerative braking energy (from the transmission to the hybrid system) 9-Mechanical braking energy 10-Aerodynamic resistance energy 11-Rolling resistance energy

With respect to the PHV with exhaust gas recuperation (Figure 7.3.1.9) drop in the mean pneumatic efficiency (position 2) can be observed (from 59.6 % to 56 %) and this can be related to increased heat loss from the compressed air to the ambient.

7.3.3 PHV W/O HEAT LOSSES IN THE AST (PERFECTLY INSULATED AST) –CASE 2

This simulation case was performed in order to determine the benefit of exhaust gas recuperation system. Ideal case of the AST system that is perfectly insulated from the surroundings is presented in Figure 7.3.3.1.

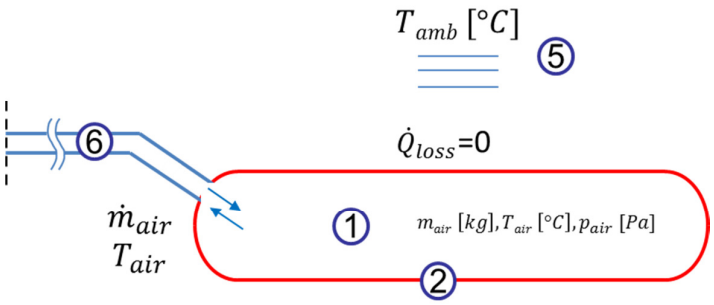

Figure 7.3.3.1 – Air Storage Tank (AST) with no heat exchange with the ambient 1) Compressed air charge 2) AST wall 5) Ambient 6) Pneumatic lines (tubes)

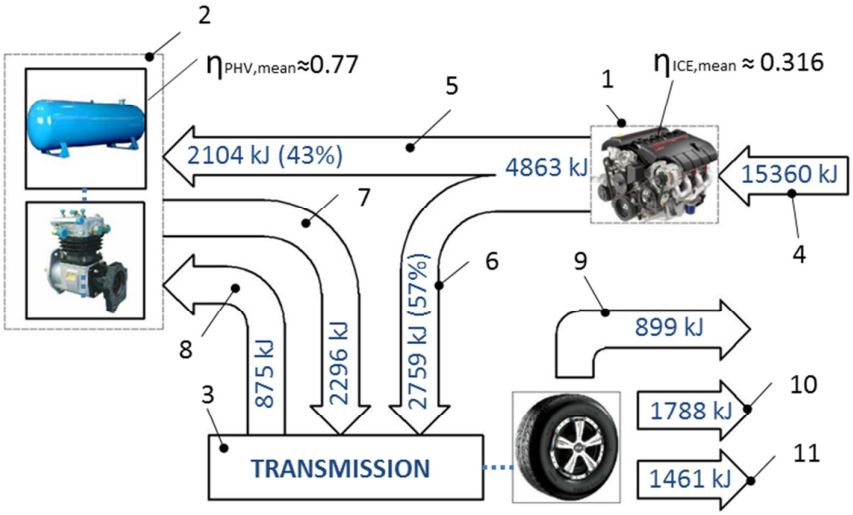

Figure 7.3.3.2 Energetic analysis for PHV w/o heat losses in the AST during NEDC cycle (all energies are referred to the primary AMT shaft axis): 1-Internal Combustion Engine 2-Hybrid powertrain part (Pneumatic Motor Compressor PMC, Air Storage Tank (AST) with exhaust gas recuperation) 3- Vehicle transmission 4- Fuel energy consumed during the cycle 5-Direct recharging energy from ICE to the PMC 6-Direct traction energy (from the ICE to the transmission) 7-Hybrid traction energy (from the hybrid system to the transmission) 8-Regenerative braking energy (from the transmission to the hybrid system) 9-Mechanical braking energy 10-Aerodynamic resistance energy 11-Rolling resistance energy

As it can be observed from energetic analysis presented in Figure 7.3.3.2 the mean pneumatic efficiency (position 2) increases up to 77 %. Also mechanical braking energy is increased since the storage system becomes less dissipative (no energy is lost due to heat losses from the AST to ambient) and maximal storage capacity (i.e. maximal air pressure inside AST) during braking is reached more easily.

7.3.4 COMPARISON AND NUMERICAL RESULTS

Table 7.3.4.1 gives numerical simulation results for PHV simulation with exhaust gas recuperation and cases 1 and 2 for NEDC and FTP72 cycle. FTP72 cycle has been included into the analysis as a representative of cycle that is closer to the real world driving.

		Base vehicle	PHV with simple AST (no exhaust gas recuperation)	**PHV with AST Exhaust gas recuperation**	PHV with perfectly insulated AST (adiabatic)
base weight	[kg]	1470	1470	1470	1470
PMC	[kg]	0	40	40	40
AST	[kg]	0	12.6	23.3	12.6
total	[kg]	1470	1522.6	1533.3	1522.6
FE ECE	[lit/100km]	6.68	4.221	4.06	3.309
Δ FE_{ECE}	[%]	x	**36.81**	**39.24**	**50.46**
FE EUDC	[lit/100km]	5.21	5.332	5.23	4.933
Δ FE_{EUDC}	[%]	x	**-2.34**	**-0.38**	**5.32**
FE NEDC	[lit/100km]	5.76	4.915	4.796	4.33
Δ FE_{NEDC}	[%]	x	**14.67**	**16.74**	**24.83**
FE FTP75	[lit/100km]	6.294	5.111	4.849	4.371
Δ FE_{FTP75}	[%]	x	**18.80**	**22.96**	**30.55**
		Mean AST temperature during the cycle [K]			
	ECE	x	463	480	644
	EUDC	x	544	590	676
	NEDC	x	490	518	655
	FTP72	x	541	580	686
		Mean thermal power exchanged between air and wall [kW]			
	ECE	x	1.25	1.14	0
	EUDC	x	1.49	0.98	0
	NEDC	x	1.33	1.08	0
	FTP72	x	1.58	1.11	0
		AST Heat loss (from air charge to the ambient) [kJ]			
	ECE	x	974.4	888.7	0
	EUDC	x	596.9	390.7	0
	NEDC	x	1571	1279	0
	FTP72	x	2162	1521	0

Table 7.3.4.1 – Results for PHV with without exhaust gas recuperation and Case 1 and Case 2 during NEDC and FTP72 cycle for $\Delta SOC = 0$ (-no S&S)*

As it can be observed, PHV vehicle with exhaust recuperation has lowest fuel economy improvement results when compared to other analyzed hybrid cases. This can be partly contributed to highly dissipative pneumatic storage system. With respect to the ideal PHV case (Table 7.3.4.1 column 3), PHV with exhaust recuperation dissipated 1279 kJ of energy as heat from the AST surface during the NEDC cycle (Table 7.3.4.1 column 2) and PHV with simple AST (Table 7.3.4.1 column 1) dissipated even higher energy amount (1571 kJ). However 22.1% fuel economy

improvement can be achieved by AST with exhaust gas recuperation when compared to the simple AST solution (Table 7.3.4.1 column 1).
Following figures give comparison between PHV with exhaust gas recuperation (Table 7.3.4.1 column 2) and PHV with simple AST (Table 7.3.4.1 column 1) over NEDC cycle.
Figure 7.3.4.1 gives comparison of compressed air temperature in the AST. In the case of PHV with exhaust gas recuperation, higher mean temperatures during ECE and EUDC cycles can be observed.

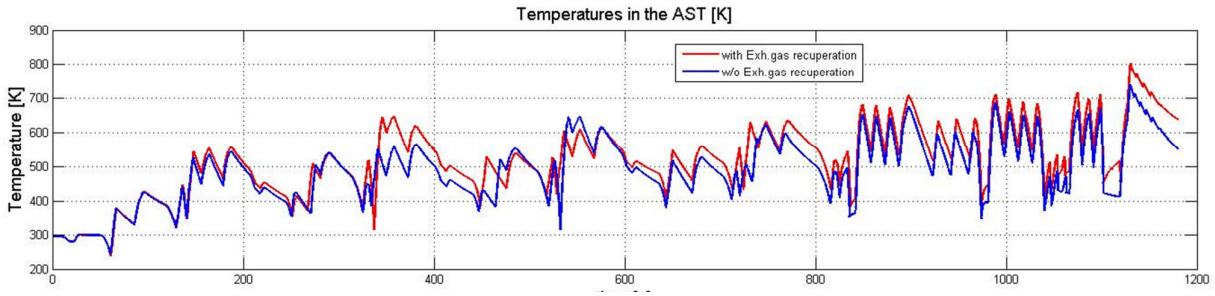

Figure 7.3.4.1 - NEDC cycle with exh.gas rec.($T_{mean,ECE}$=480K, $T_{mean,EUDC}$=590K), w/o exh.gas rec.($T_{mean,ECE}$=463K, $T_{mean,EUDC}$=544K)

Figure 7.3.4.2 gives comparison of the thermal power exchanged between air inside the AST and the AST wall where positive values represent heat loss and negative values represent recuperated heat. In the case of PHV with exhaust gas recuperation, lower mean thermal power values during ECE and EUDC cycles can be observed.

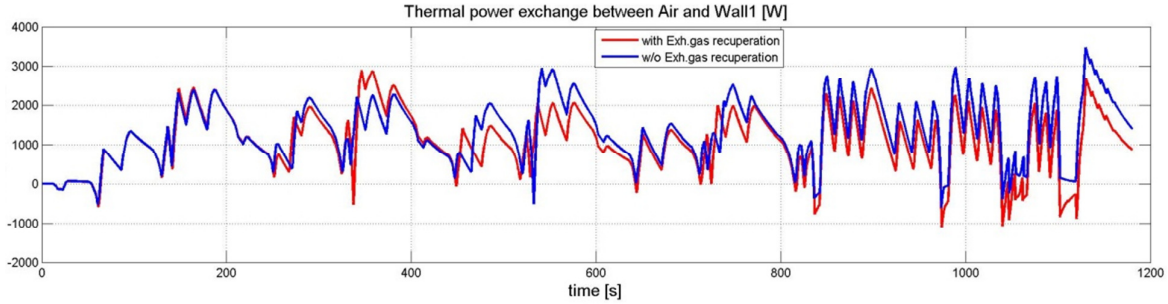

Figure 7.3.4.2- NEDC cycle with exh.gas rec.($P_{mean,ECE}$=1.14kW, $P_{mean,EUDC}$=0.98kW), w/o exh.gas rec.($P_{mean,ECE}$=1.25kW, $P_{mean,EUDC}$=1.49kW)

Figure 7.3.4.3 gives comparison of the AST wall (Figure 7.2.4.1.4 position 2) temperatures for both reported cases. AS expected, mean wall temperature increases more rapidly for the case with exhaust gas recuperation.

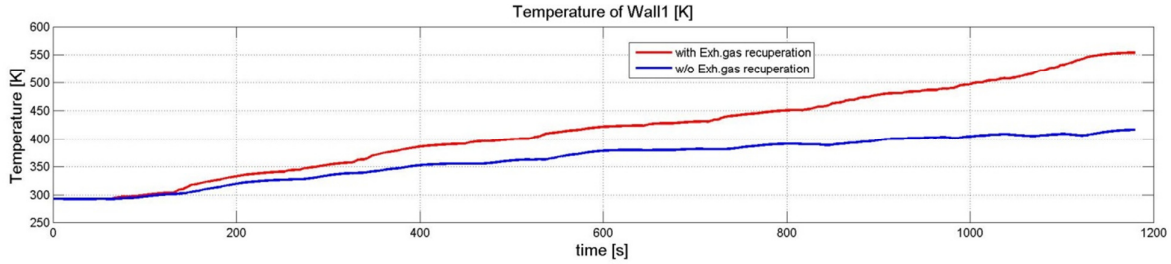

Figure 7.3.4.3 AST wall temperature during NEDC cycle for cases with and w/o exhaust gas recuperation

Based on the presented simulation results PHV vehicle with exhaust gas recuperation offers fuel economy improvement of 39 % in the urban cycle, no improvement in extra-urban and close to 23 % in combined cycle (NEDC). Presented fuel economy improvement results are compared to a standard vehicle without start & stop system and with idealized case of regenerative braking i.e. all braking is performed only with regenerative brakes when braking deceleration is below 0.1 g. Also, ECMS strategy implies discontinuous operation of the engine and that does not favor the quality of the exhaust gas recuperation. Further, high exhaust gas temperature is present in the AST when the AST tank is typically being charged and the air is already at high temperature.

However, margin for improvement of the PHV vehicle still remains. In order to decrease thermal losses of the AST system, its surface area can be decreased. This would lead to increasing the pressure level for the equivalent stored energy. Furthermore, ECMS control strategy is not oriented to the Short Term Energy Storage systems, and therefore is not able to anticipate the conditions when vehicle is stopped and the stored energy is quickly dissipated. Control algorithm should be expanded in order to include these conditions and not to over-charge the system when immediate vehicle stop is expected. Besides, strategy should also consider extremely limited energy storage capacity of the AST in the way not to over-charge the system when vehicle is at high speeds and the regenerative braking is expected to follow. Also, adding heat to the air between expansion stages can be considered in the way to lead the process as close as possible to isothermal expansion.

8. CONCLUSIONS

In this work comparative analysis of alternative hybrid systems for a parallel hybrid passenger vehicle was presented. The main objective of this analysis was to investigate the impact of different hybridization concepts and levels of hybridization on fuel economy of a standard road vehicle where both conventional and non-conventional hybrid architectures are treated exactly in the same way from the point of view of overall energy flow optimization.

One of the objectives was also to demonstrate that non-conventional hybrid layouts may (and should) be fully exploited to achieve the best possible results in terms of cycle overall fuel economy, extending and widening the mainstream perspective of alternative hybrid solutions.

Hybrid component models were developed and presented in detail in previous chapters as well as the simulations results mainly during NEDC cycle.
The analysis was performed on four different parallel hybrid powertrain concepts:

- Hybrid Electric Vehicle (HEV)
  - Case 1
  - Case 1* (this is particular case with VSP-ECMS algorithm implemented)
  - Case 2
  - Case 3
- High Speed Flywheel Hybrid Vehicle (HSF-HV)
- Hydraulic Hybrid Vehicle (HHV)
- Pneumatic Hybrid Vehicle (PHV)

Following table represents main characteristics of analyzed hybrid solutions such as energy storage and power capability, as well as specific energy and specific power for each system. It should be noted, that all energy and power values are referred to weight of the whole hybrid system that takes into account not only energy storage system (i.e. battery, accumulator, air storage tank or high speed flywheel) but also hybrid propulsion device (electric motors and generators, hydraulic motor pump, pneumatic motor compressor, continuously variable transmission) as well as the accessories of each particular system.

	Overall hybrid weight [kg]	Maximal hybrid energy [kJ]	Specific energy [Wh/kg]	Nominal hybrid power [kW]	Specific power [kW/kg]
HEV Case 1	99.6	1872	5.22	30	0.301
HEV Case 2	63.4	1296	5.68	10	0.158
HEV Case 3	49	625	3.54	10	0.204
HSF-HV	40	625	4.34	86	2.150
HHV	135.6	625	1.28	125	0.922
PHV	63.3	300	1.32	50	0.790

Table 8.1 Main parameters of analyzed hybrid solutions

In order to perform equitable analysis of different hybrid systems, comparison was performed also on the basis of the same usable system energy storage capacity (i.e. 625kJ for HEV case 3, HSF and

the HHV) but in the case of pneumatic hybrid systems maximal storage capacity was limited by the size of the systems in order to comply with the packaging requirements of the vehicle.

Figure 8.1 gives comparison between different hybrid systems with respect to overall hybrid weight and energy storage capacity.

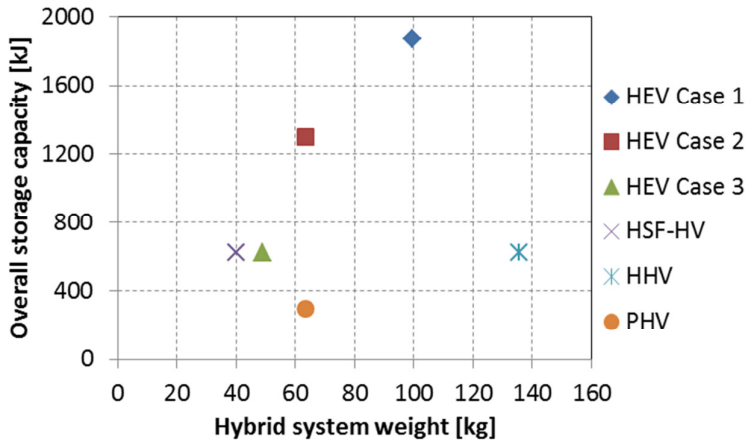

Figure 8.1 Comparison between different hybrid systems with respect to overall hybrid weight and energy storage capability

Figure 8.2 demonstrates specific energy and power for all hybrid solutions. As can be seen, Hydraulic and Pneumatic hybrid systems have high specific power capabilities as well as lowest specific energy potential, while Hybrid electric systems have opposite characteristics. However, in comparison with other systems, High Speed Flywheel System (HSF) offers best compromise between specific energy and power requirements for a given application.

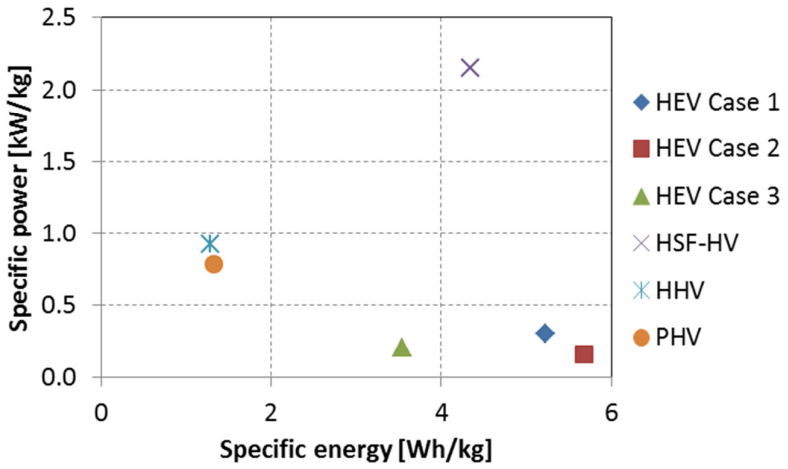

Figure 8.2 Comparison between different hybrid systems with respect to specific power and specific energy of the systems

As described in the previous chapters, the simulations were performed within the IAV Gmbh - VeLoDyn software simulator based on Matlab / Simulink software package. Advanced cycle independent control strategy (ECMS) was implemented into the hybrid supervisory control unit in order to solve power management problem for all hybrid powertrain solutions (HEV, HSF, HHV

and PHV). In order to maintain State of Charge within desired boundaries during different cycles and to facilitate easy implementation and recalibration of the control strategy for very different hybrid systems, Charge Sustaining Algorithm was added into the ECMS framework.

Also, a Variable Shift Pattern VSP-ECMS algorithm was proposed as an extension of ECMS capabilities so as to include gear selection into the determination of minimal (energy) cost function of the hybrid system. Further, cycle-based energetic analysis was performed in all the simulated cases, and the results have been reported in the corresponding chapters. All the simulations were carried out by using steady experimental engine state maps without taking into account warm-up of the engine at the beginning of the homologation cycle. Also, ideal regenerative braking scenario was considered [1] and the vehicle was able to brake only with regenerative brakes whenever the vehicle deceleration was below 1 m/s^2.

Figure 8.3 represents fuel economy improvement (%) for all simulated powertrain configurations with respect to the base vehicle, during urban (ECE), extra-urban (EUDC) and combined European cycle (NEDC).

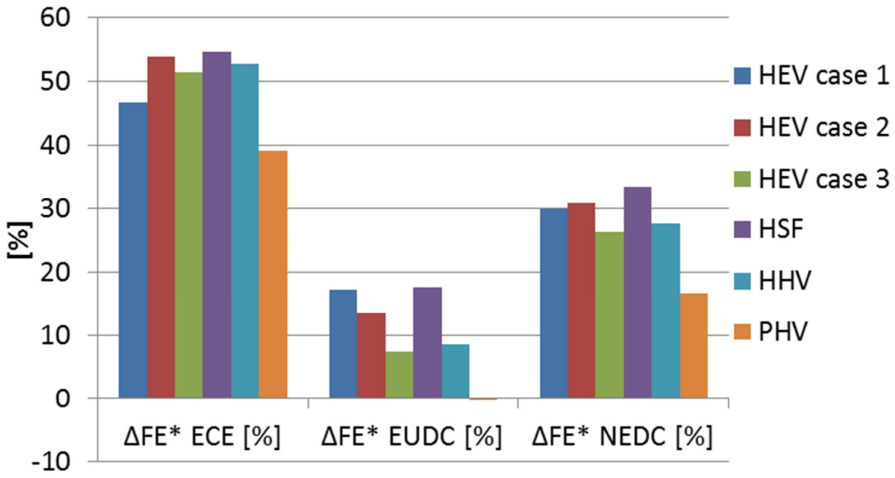

Figure 8.3 - Fuel Economy improvement [%] during NEDC cycle with respect to the base vehicle

Based on Figure 8.3 it can be stated that biggest advantage of most hybrid solution can be observed during urban cycle (ECE) under low cycle load conditions when the engine is operating at low efficiency. In this situation, it proves advantageous to avoid utilization of the internal combustion engine by using hybrid system to provide propulsion for the vehicle, or to use the hybrid system in order to shift the engine operating point into zones of higher load and higher efficiency. However, during extra-urban driving (EUDC) advantage of using any hybrid system diminishes since the engine is mainly operating in the more favorable efficiency zone (Figures 2.4.1. and 2.4.2). The main advantage of the hybrid system in these conditions lies is in the fact that it is able to recover part of the vehicle kinetic energy during regenerative braking. All results presented in the Figure 8.3 have been corrected according to the ECE directive regarding the Method of Measuring of the Emissions of Carbon Dioxide, Fuel Consumption and the Electric Energy Consumption of Vehicles Powered by a Hybrid Electric Powertrain [12].

	ECE		EUDC		NEDC	
	FE [lit/100km]	ΔFE* [%]	FE [lit/100km]	ΔFE* [%]	FE [lit/100km]	ΔFE* [%]
base vehicle	6.68	x	5.21	x	5.76	x
HEV Case 1	3.56	46.71	4.31	17.32	4.03	29.96
HEV Case 2	3.08	53.87	4.51	13.39	3.98	30.80
HEV Case 3	3.25	51.37	4.83	7.40	4.24	26.31
HSF-HV	3.04	54.57	4.29	17.7	3.82	33.5
HHV	3.16	52.67	4.76	8.62	4.17	27.57
PHV	4.06	39.24	5.23	-0.38	4.796	16.74

Table 8.2 Numerical result for all hybrid simulations for cycle NEDC

Based on Figure 8.3 and Table 8.2, highest fuel economy improvement during NEDC cycle can be achieved with HSF hybrid solution. This can be related to the relatively high system efficiency of the mechanical energy path (Figure 8.4) and high power to weight ratio (Table 8.1) of the hybrid part of the powertrain.

As it can be observed, Pneumatic Hybrid System offers lowest fuel economy improvement during NEDC cycle due to the extremely dissipative nature of the pneumatic storage system (high thermal losses of the air charge inside the Air Storage System (AST) are present). Also, extremely limited storage capacity limits regenerative braking potential of the hybrid system that is accompanied by high utilization of mechanical braking during the cycle (Figure 7.3.1.9). HHV system offers better FE with respect to the HEV-Case 3 and PHV, though HHV system has highest weight penalization. Good trade-off between EMG size and Battery size represents HEV – Case 2, though a low EMG power capability deteriorates regenerative potential (Figure 4.4.1.5) when compared to HEV-Case 1. The HEV-Case 3 system offers lowest fuel improvement when compared to the other hybrid electric solutions, as a result of insufficient battery energy storage and power capabilities that results with lower mean hybrid efficiency when compared to HEV Case 2 and lower energy recovery during regenerative braking.

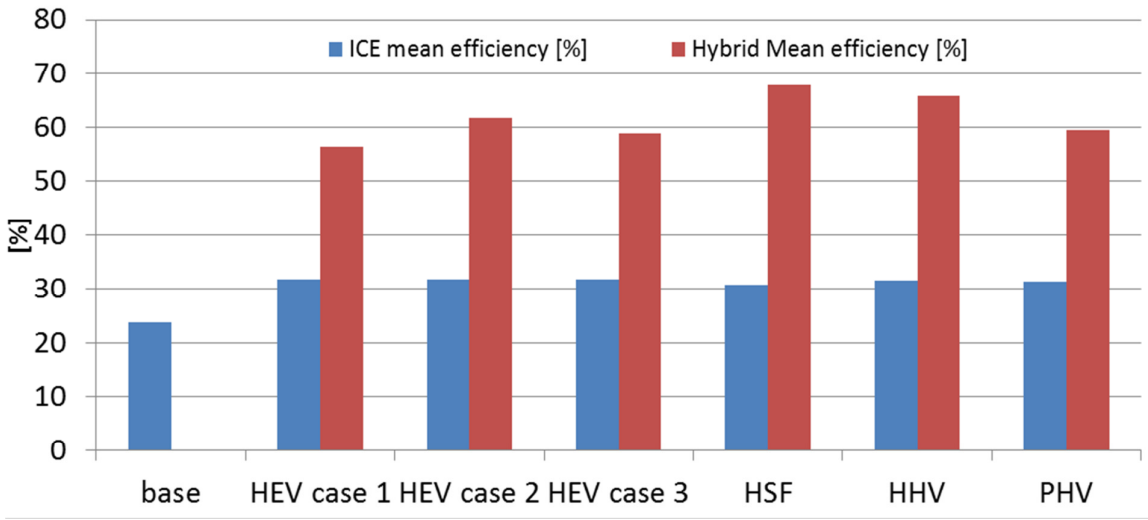

Figure 8.4 – Mean engine and Hybrid powertrain part efficiency (HEV (Case 1, 2 and 3), HSF, HHV and PHV) during NEDC cycle

Figure 8.4 demonstrates mean engine and mean hybrid efficiency during NEDC cycle for all analyzed hybrid solutions. As a first point, it can be noticed that thanks to global energy minimization principle embedded into the control strategy operation, mean efficiency of the engine during NEDC cycle is risen from 0.23 (Figure 2.4.4) to values above 0.30, for all hybrid powertrain cases (HEV, HSF, HHV and PHV). HSF hybrid solution has the highest mean hybrid efficiency of all analyzed systems (~68%), and this can be contributed to the relatively high individual efficiencies of the hybrid components as well as efficient energy storage system (flywheel). HHV system offers also high mean efficiency value due to efficient hydraulic energy storage system (≥95%) but it suffers from weight penalization. Difference between mean hybrid efficiency for HEV solutions was explained in the previous chapters (4.4.1) and is mainly related to sizing of the components.

Figure 8.5 represents braking energy distribution during the NEDC cycle for all analyzed powertrain cases and base vehicle. Highest percentage of mechanical braking is present in the pneumatic hybrid vehicle case, due to extremely limited storage capacity of the system. HEV Case 3 also has relatively high mechanical braking percentage during cycle and this can be attributed to limited power capabilities of the Case 3 battery (Figure 4.4.1.6). Due to the sufficiency energy and power capability HEV Case 1 is able to recuperate all braking energy during NEDC cycle. Certainly, further FE improvement can be achieved by increasing recuperative potential of the systems (minimizing the mechanical braking) by proper selection (sizing) of the hybrid components (battery and propulsion (generator) device).

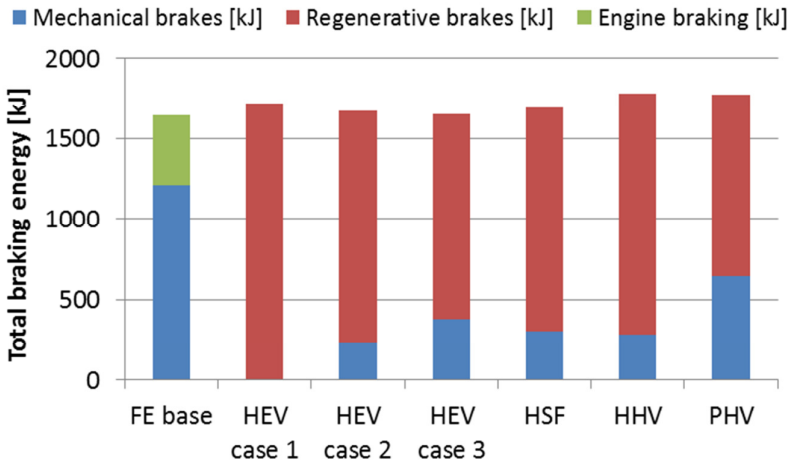

Figure 8.5 – Braking energy distribution during NEDC cycle

Figure 8.6 displays graphical representation of all energy flows within the powertrain during homologation cycle. Overall energy produced by the internal combustion engine is distributed between direct traction energy (T) that follows mechanical energy path from the engine to the wheel and recharging energy (R) that follows the hybrid part.

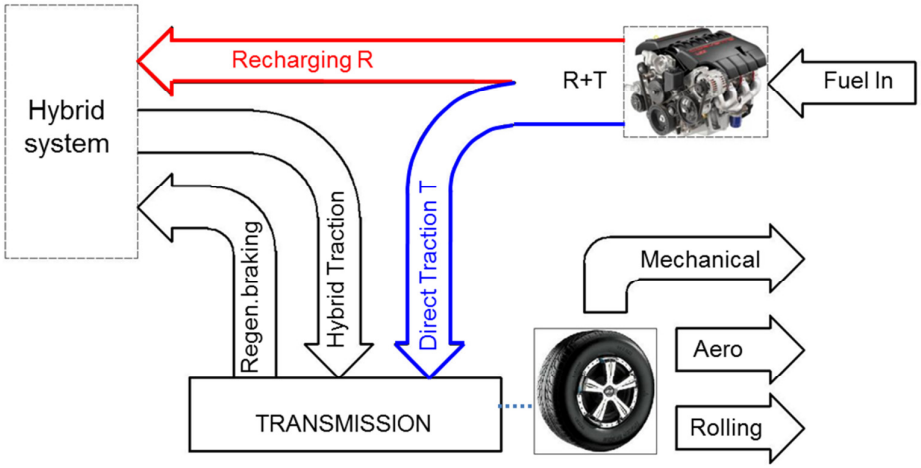

Figure 8.6 - Engine energy distribution between recharging (R) and direct traction (T) energy

Interesting question presents itself as what is the ideal engine energy distribution that will lead to best fuel economy during the cycle for a given powertrain configuration?

Direct traction (Figure 8.6 – Position T) energy path (engine →transmission →wheel) is certainly the most efficiency way to transfer energy from the engine to the wheel while hybrid energy path (engine → hybrid system →transmission →wheel) inadvertently suffers from energy conversion losses. However, as we know from the standard (non-hybrid) vehicle simulations during NEDC cycle the engine usually operates in the zone of relatively low efficiency. As stated before, in order to improve mean engine efficiency during the cycle, the hybrid powertrain is utilized as means to perform engine operating (load) point shift to the zones of higher efficiency whenever the engine is operating in low load conditions. Excess energy created by the engine is stored inside the energy storage system of each hybrid system (battery, hydraulic accumulator, High speed flywheel, Air storage tank). In this way the energy is "forced" down the hybrid path and has to suffer energy conversion losses though engine is operating in the zone of higher efficiency and lower specific fuel consumption. Therefore, for every specific hybrid powertrain solution it is important to find the optimal engine energy flow distribution that will result with minimal fuel consumption during the cycle. Increase of the recharging percentage (Figure 8.7 Position R) might lead to serial powertrain behavior that would suffer energy conversion losses, while extreme decrease of the recharging percentage might lead to non-charge sustaining powertrain behavior during the cycle (and possibly decrease of the mean engine cycle efficiency). In the extreme case, when recharging percentage is zero, all engine energy will be forced down the "mechanical" path (standard vehicle operation) while the hybrid system will assume simple KERS functionality (recovery of the braking energy).

In order to further improve the fuel consumption of the hybrid vehicle, standard ECMS algorithm was expanded in order to include the optimized gear shift pattern (Chapters 3.2 and 3.3). Due to the optimization of the shift pattern, relative consumption improvement with respect to the non-optimized case during urban cycle is 8.6 %, extra-urban 15.9 % and NEDC cycle 11% for the HEV Case 1.

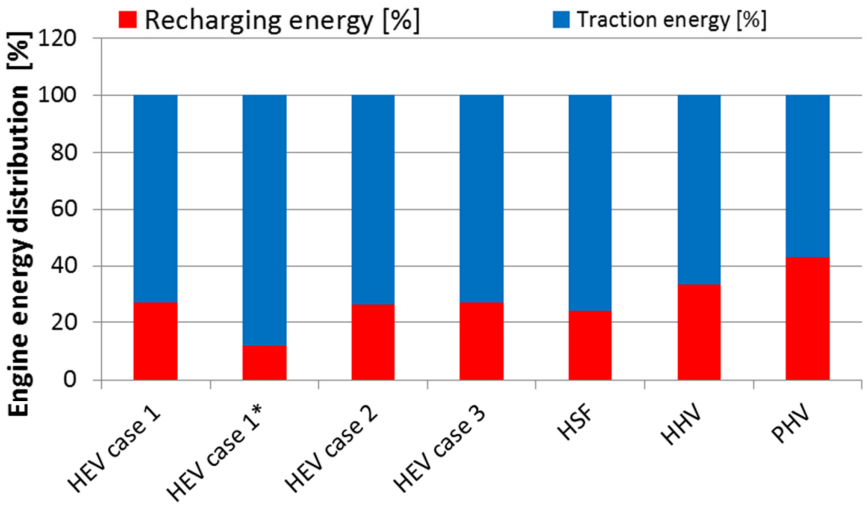

Figure 8.7 Engine energy distributions during NEDC cycle for different hybrid solutions

Figure 8.7 represents energy distribution of the internal combustion engine during NEDC cycle for all analyzed cases. As can be seen, highest recharging percentage accompanies pneumatic hybrid system since it is highly dissipative and requires constant recharging. HEV Case 1* represent the simulation case that utilizes newly proposed Variable Shift Pattern ECMS (VSP-ECMS) algorithm. In this case, recharging percentage is decreased by using the most efficient shift pattern that is able to "force" higher percentage of engine energy down the mechanical path while maintain high engine mean cycle efficiency. As can be seen from the Chapters 3.2, 3.3, 4.4.2 VSP-ECMS algorithm implementation, leads to the cycle fuel economy improvement when compared to the same simulation case with standard ECMS algorithm.

9. DEFINITIONS/ABBREVIATIONS

HEV	Hybrid Electric Vehicle
HSF	High Speed Flywheel
HSF-HV	High Speed Flywheel Hybrid Vehicle
HHV	Hydraulic Hybrid Vehicle
PHV	Pneumatic Hybrid Vehicle
ECMS	Equivalent Consumption Minimization Strategy
VSP	Variable Shift Pattern
CVT	Continuously Variable Transmission
HMP	Hydraulic Motor Pump
ICE	Internal Combustion Engine
HPA	High Pressure Accumulator
LPA	Low Pressure Accumulator
EMG	Electric Motor Generator

10. REFERENCES

1. Yimin Gao, Liping Chen, Mehrdad Ehsani, Investigation of the Effectiveness of Regenerative braking for EV and HEV, Future Transportation Technology Conference & Exposition, August 1999, Costa Mesa, CA, USA, SAE technical paper number 1999-01-2910
2. Young Jae Kim, Zoran Filipi, Simulation study of a Series Hydraulic Hybrid Hybrid Propulsion System for a Light Truck, Commercial Vehicles Engineering Congress and Exhibition, Rosemont, USA, October 2007, SAE technical paper number 2007-01-4151
3. Cristian Musardo, Giorgio Rizzoni, Benedetto Staccia, A-ECMS: An Adaptive Algorithm for Hybrid Electric Vehicle Energy Management, Proceedings of the 44th IEEE Conference on Decision and Control and the European Control Conference 2005, Seville, Spain, MoC13.2
4. Pierluigi Pisu, Giorgio Rizzoni, A Comparative Study of Supervisory Control Strategies for Hybrid Electric Vehicles, IEEE transactions on Control Systems Technology, vol.15, NO.3, May 2007, 1063-6536
5. Karem Koprubasi, Modeling and Control of a Hybrid Electric Vehicle for Drivability and Fuel Economy Improvements, 2008 The Ohio State University, USA, PhD thesis
6. Lorenzo Serrao, A Comparative Analysis of Energy Management Strategies for Hybrid Electric Vehicles, 2009 The Ohio State University, USA, PhD thesys
7. Georges E.M. Vael, Peter A.J. Achten, Titus van der Brink, Efficiency of a Variable Displacement Open Circuit Floating Cup Pump, The 11th Scandinavian International Conference on Fluid Power, SICFP '09 , 2009 Linkoping, Sweden
8. Peter A.J.Achten, The Hydrid Transmission, Commercial Vehicle Engineering Congress and Exhibition, Il USA, 2007, SAE technical paper number 2007-01-4152
9. Z.Filipi, Y.J.Kim, Hydraulic Hybrid Propulsion for Heavy Vehicles: Combining the Simulation and Engine-In-the-Loop Techniques to Maximize the Fuel Economy and Emission Benefits, Oil & Gas Science and Technology – Rev. IFP, Vol. 65 (2010), No. 1, pp. 155-178, 2009
10. EPA, Progress Report on Clean and Efficient Automotive Technologies Under Development at EPA Interim Technical Report, 2004
11. Davide Moro, Nicolò Cavina, Igor Trivić, Vittorio Ravaglioli, Guidelines for Integration of Kinetic Energy Recovery System (KERS) based on Mechanical Flywheel in an Automotive Vehicle , International Powertrains, Fuels & Lubricants Meeting, May 2010, Rio De Janeiro, BRAZIL, SAE technical paper number 2010-01-1448
12. Agreement Concerning The Adoption of Uniform Technical Prescriptions for Wheeled Vehicles, Equipment and Parts Which Can be Fitted and /or be Used on Wheeled Vehicles and the Conditions for Reciprocal Recognition of Approvals Granted on The Basis of These Prescriptions, Regulation N. 83 and 101, Annex 8 " Method of Measuring of the Emissions of Carbon Dioxide, Fuel Consumption and the Electric Energy Consumption of Vehicles Powered by a Hybrid Electric Powertrain", United Nations 2005
13. Douglas Cross, Chris Brockbank, Mechanical Hybrid System Comprising a Flywheel and CVT for Motorsport and Mainstream Automotive Applications, SAE 2009 World Congress and Exhibition, Detroit USA, SAE technical paper number 2009-01-1312
14. Barr A, Veshagh A, "Fuel Economy and Performance Comparison of Alternative Mechanical Hybrid Powertrain Configurations", SAE 2008 World Congress, Detroit, USA. SAE technical paper number : 2008-01-0083
15. Enrico Cacciatori, Baptiste Bonnet, Nicholas D.Vaughan, Matthew Burke, David Price, Krzysztof Wejrzanovski, Regenerative Braking Strategies for a Parallel Hybrid Powertrain with Torque Controlled IVT, SAE 2005 Powertrain and Fluid Systems Conference and Exhibition, San Antoni USA, SAE technical paper number 2005-01-3826

16. Flynn M M, Zierer J J, Thompson R C, "Performance Testing of a Vehicular Flywheel Energy System." Advanced Hybrid Vehicle Powertrains 2005, Detroit USA, SAE technical paper number: 2005-01-0809
17. D.Cross, J.Hilton, High Speed Flywheel Based Hybrid Systems for Low Carbon Vehicles, Coventry, 2008 Hybrid and Eco-Friendly Vehicle Conference, IET HEVC, ISSN:0537-9989
18. R.J.Hayes, J.P.Kajs, R.C.Thompson and J.H.Beno Design and Testing of a Flywheel Battery for a Transit Bus, SAE 1999 Internation Congress and Exposition, Detroit, USA, SAE technical paper number 1999-01-1159
19. Joseph Beno, Richard Thompson, Robert Hebner, Flywheel batteries for Vehicles, IEEE Autonomous Underwater Vehicles, 2002 Proceedings of the 2002 workshop.
20. Curtis Darrel Anderson, Judy Anderson, Electric and hybrid cars: a history, McFarland &Company, Inc., Publishers, ISBN 0-7864-1872-9
21. www.hybrid-cars.us
22. www.hybridcars.com
23. www.volkswagen-media-services.com
24. Michael Duoba, Henry Ng, Robert Larsen, Characterization and Comparison of Two Hybrid Electric Vehicles (HEVs) – Honda Insight and Toyota Prius, SAE 2001 World Congress, March 2001, Detroit, MI, USA, paper No. 2001-01-1335
25. Jerome Meisel, An Analytic Foundation for the Toyota Prius THS-II Powertrain with a Comparison to a Strong Parallel Hybrid-Electric Powertrain, SAE 2006 World Congress & Exhibition, April 2006, Detroit, MI, USA, Paper No. 2006-01-0666
26. http://www.toyota-global.com/innovation/environmental_technology/
27. www.uqm.com
28. Giancarlo Genta, Motor vehicle dynamics – modeling and simulation, World Scientific Publishing Co. Pte. Ltd, 1997 ISBN 9810229119
29. http://www.flybridsystems.com
30. http://www.torotrak.com
31. http://en.wikipedia.org
32. Sung K. Ha, Dong-Gun Lee, Dong-Jin Kim, Optimization of Hybrid Composite Rotor in Flywheel Battery, Future Transportation Technology Conference & Exposition Costa Mesa, CA, August 11-13, 1998, SAE 981899
33. J.D.Herbst, S.M. Manifold, B.T. Murphy, J.H. Price, R.C. Thompson, W.A. Walls, A. Alexander, K. Twigg, Design, Fabrication and Testing of 10MJ Composite Flywheel Energy Storage Rotors, Aerospace Power Systems Conference, April 1998, Williamsburg, VA, USA, Session: Power Units for the Future, SAE 981282
34. Mukund R. Patel, Flywheel energy Storage for Spacecraft Power Systems, 34th Intersociety Energy Conversion Engineering Conference, August 1999, Vancouver, Space Power Systems, Applications and Requirements III, SAE 1999-01-2589
35. B. G. Beaman,G. M. Rao, Hybrid battery and flywheel energy storage system for LEO spacecraft, Battery Conference on Applications and Advances, 1998., IEEE 1089-8182
36. http://www.williamshybridpower.com/technology/whps-flywheel-technology
37. Jerome Tzeng, Ryan Emerson, Paul Moy, Composite Flywheels for Energy Storage, Composites Science and Technology 66 (2006) 2520–2527
38. Rob C. Wagner, David R. Boyle, Kent Decker, Commercialization of Flywheel Energy Storage Technology on the International Space Station, 37th Intersociety Energy Conversion Engineering Conference, 2002, IECEC paper No. 20015
39. B.T. Murphy, D.A. Bresie, J.H. Beno, Bearing Loads in a Vehicular Flywheel Battery, SAE Special Publications, v 1243, Feb, 1997, Electric and Hybrid Vehicle Design Studies, Proceedings of the 1997 International Congress and Exposition, Feb 24-27 1997, Detroit, MI

40. Pourmovahed A., Baum S.A., Fronczak F.J., Beachley N.H. (1988) Experimental Evaluation of Hydraulic Accumulator Efficiency with and without Elastomeric Foam, J. Propul. Power 4, 2, 185-192.
41. Pourmovahed A., Otis D.R. (1990) An Experimental Thermal Time-Constant Correlation for Hydraulic Accumulators, J. Dyn. Syst.-T. ASME 112, 1, 116-121.
42. Wilson, W.E., Performance Criteria for Positive Displacement Pumps and Fluid Motors, ASME Semi-Annual Meeting, 1948, paper No. 48-SA-14
43. Wilson, W.E., Hydraulic Pumps and Motors, Machine Design, 1949
44. Schlöser, W.M.J, Ein Mathematisches Modell für Verdrängerpumpen und motoren, Ölhzdraulik und Pneumatik 5, No.4, 1961, pp. 122-129
45. Thoma, J., Mathematische Modelle und die effective Leistung hzdrostatischer Maschinen und Getriebe, Ölhzdraulik und Pneumatik 14, No.6, 1970, pp. 233-237
46. Wilson, W.E., How to Calculate Hydrostatic Transmission Coefficiencts, Hydraulics and pneumatics, 1964, pp. 104-106
47. Karl-Erik Rydberg, Efficiencies for variable hydraulic pumps and motors – Mathematical models and operation conditions, 2009, LiTH, IEI/FluMeS
48. Hugosson C, Cumulo Hydrostatic Drive – a Vehicle Drive with Secondary Control , The Third Scandinavian Int. Conference on Fluid Power, Linköping, Sweden, 1995, vol. 2, pp 475-494.
49. Achten P., A serial hydraulic hybrid drive train for off-road vehicles,
50. EPA (2006) World's first full hydraulic hybrid in a delivery truck, http://www.epa.gov/otaq/technology/420f06054.pdf
51. www.permo-drive.com
52. Mohamed Saber Ahmed Ibrahim, Investigation of Hydraulic Transmissions for Passenger Cars, Doctoral dissertation, RWTH Aachen University, 2011
53. www.eaton.com
54. http://www.epa.gov/oms/technology/research/demonstration-vehicles.htm
55. www.artemisip.com
56. The Automotor and Horseless Vehicle Journal, No. 006. 1897 March 17
57. www.tramwayinfo.com
58. www.aircaraccess.com
59. www.aircarfactories.com
60. www.mdi.lu
61. Ulf Bossel, Thermodynamic Analysis of Compressed Air Vehicle Propulsion, Journal of KONES Internal Combustion Engines, 2005, vol. 12, 3-4
62. SAE 2011-01-1133, "Evaluation of Intercooler Efficiency as a Technique for Reducing Diesel Engine Emissions "
63. Lars Eriksson, Lars Nielsen, Jan Brugard "Modeling of Turbocharged SI Engine" – Annual reviews in Control 26 (2002) 129-137
64. Incropera, DeWitt, Bergman, Lavine – " Fundamentals of Heat and Mass Transfer "
65. Yantovski E. "What is exergy?" Proc. Int. Conf. ECOS 2004, Ed. By R.Rivero, L.Monroy, R.Pulido, G.Tsatsaronis, Mexico, 7-9 July 2004, pp 801-817.
66. Leonardo de Oliveira Carvalho, "Exergetic Analysis of Compressed Air for Vehicular Propulsion", SAE 2008-36-0315
67. Y.M.Kim, D.Favrat, "Energy and Exergy analysis of a micro-compressed air energy Storge and cycle heating and cooling system", Energy Volume 35, Issue 1, January 2010, Pages 213–220
68. J.F.Osterie, "The Thermodynamics of Compressed Air Exergy Storage", Journal of Energy Resources Technology, March 1991, Vol.113/7

69. Noam Lior, Na Zhang, Energy, Exergy and Second Law Performance Criteria, 18th International Conference on Efficiency, Cost, Optimization, Simulation, and Environmental Impact of Energy Systems — ECOS 05, Volume 32, Issue 4, April 2007, Pages 281–296
70. Christian Dönitz, Iulian Vasile, Christopher Onder, and Lino Guzzella, Dynamic Programming for Hybrid Pneumatic Vehicles, 2009 American Control Conference Hyatt Regency Riverfront, St. Louis, MO, 2009
71. Lino Guzzella, Antonio Sciarretta, Vehicle Propulsion Systems, Springer ISBN 978-3-540-74691-1
72. Christian Dönitz, Iulian Vasile, Christopher Onder and Lino Guzzella, Realizing a Concept for High Efficiency and Excellent Driveability: The Downsized and Supercharged Hybrid Pneumatic Engine, SAE World Congress & Exhibition, April 2009, Detroit, MI, USA, 2009-01-1326
73. Sasa Trajkovic, The Pneumatic Hybrid Vehicle, Doctoral Thesis, Faculty of Engineering Lund University, 2010
74. Saša Trajković, Per Tunestål and Bengt Johansson, Investigation of Different Valve Geometries and Valve Timing Strategies and their Effect on regenerative Efficiency for a Pneumatic Hybrid with Variable Valve Actuation, SAE International Powertrains, Fuels and Lubricants Congress, June 2008, Shanghai, CHINA, paper No 2008-01-1715
75. Peter Beater, Pneumatic drives: system design, modeling and control, Springer 2007, ISBN 13-978-3-540-69470-0
76. Incropera; DeWitt, Bergman, Lavine (2007). Fundamentals of Heat and Mass Transfer (6th edition ed.). John Wiley & Sons. pp. 260–261. ISBN 978-0-471-45728-2.

APPENDIX I

"OFFLINE" ANALYSIS OF THE GLOBAL CHARGING AND DISCHARGING EFFICIENCY OF THE PHV SYSTEM

Detailed efficiency analysis of the pneumatic powertrain part was carried out during charging and discharging process. The analysis determines instantaneous efficiency of the whole pneumatic system and takes into account losses described in the chapters 7.1 and 7.2. Charging and discharging efficiency maps were created as well as effective (at the PMC shaft) power that systems can develop and are presented in this Appendix.

The efficiency analysis was carried out in function of several operational parameters:

1. Pneumatic Motor Compressor (PMC) shaft speed
2. Air Storage Tank (AST) state of charge value
3. Displacement factor x of the PMC
4. Mean AST wall temperature

All efficiency maps were created in "off-line" mode, i.e. pneumatic system was decoupled from the vehicle driveline. Later the efficiency data was introduced as 4-D maps into Pneumatic Hybrid Vehicle (PHV) simulation.

It should be noted that efficiency results represent only instantaneous efficiency and don't include the energy "drain" losses when the system is not in use. There losses would manifest themselves as thermal losses of the compressed air charge versus ambient when the temperature of the compressed air is higher than ambient temperature.

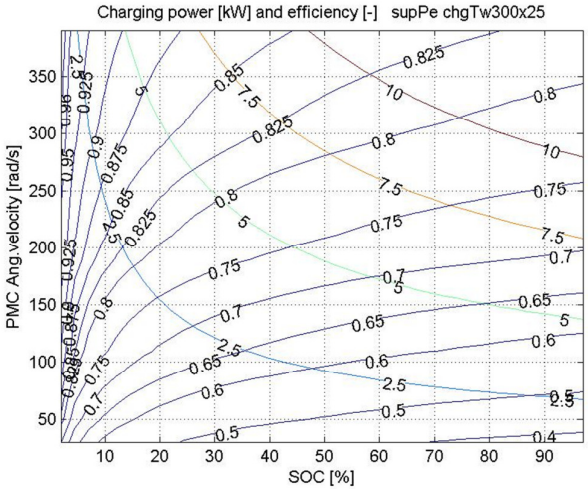

Figure AI-01– Global efficiency and available power during charging for AST wall temperature T_{wall}=300K and displacement factor x=0.25

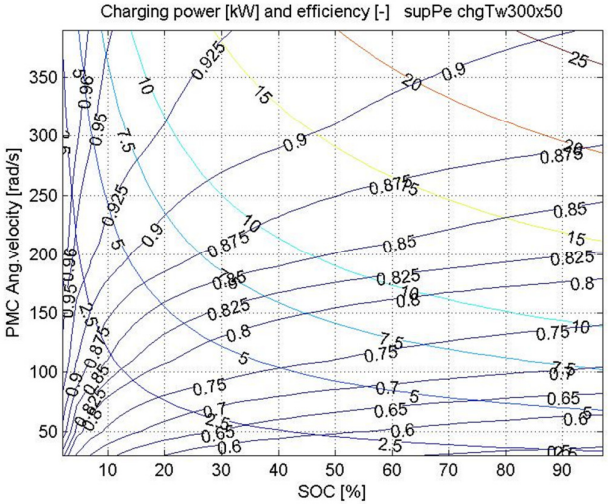

Figure AI-02– Global efficiency and available power during charging for AST wall temperature T_{wall}=300K and displacement factor x=0.5

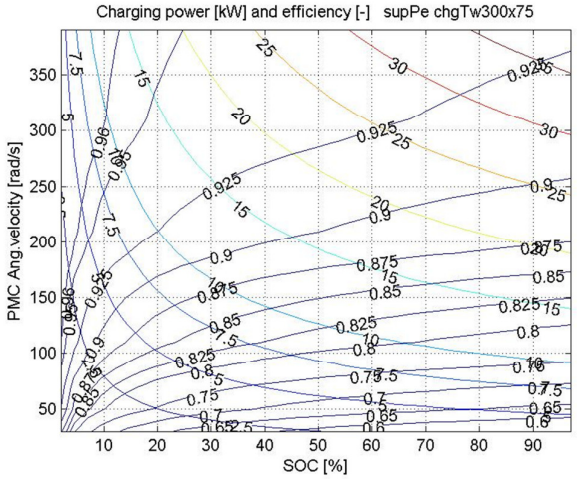

Figure AI-03– Global efficiency and available power during charging for AST wall temperature T_{wall}=300K and displacement factor x=0.75

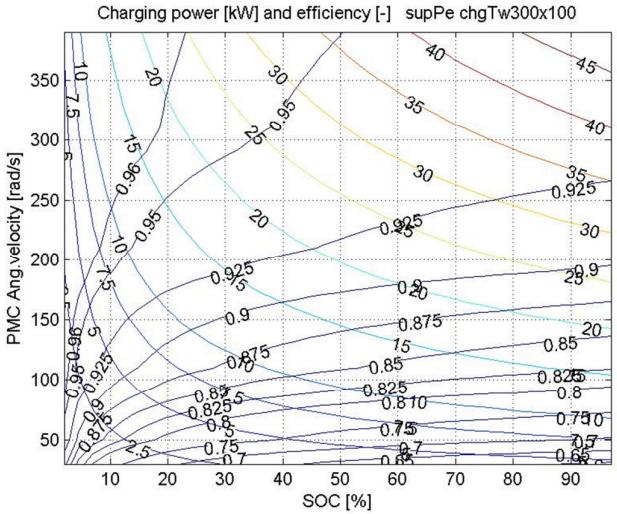

Figure AI-04– Global efficiency and available power during charging for AST wall temperature T_{wall}=300K and displacement factor x=1

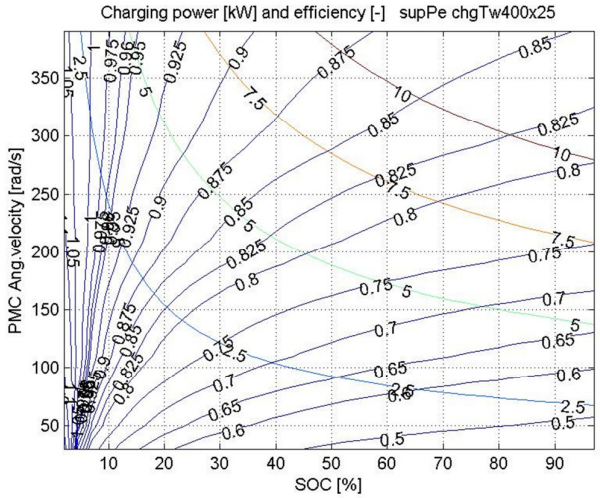

Figure AI-05– Global efficiency and available power during charging for AST wall temperature T_{wall}=400K and displacement factor x=0.25

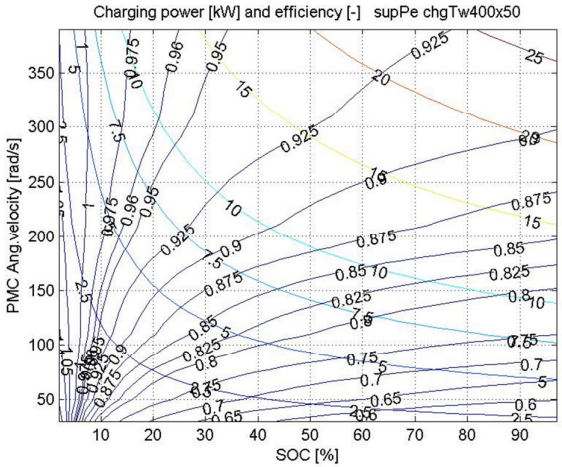

Figure AI-06– Global efficiency and available power during charging for AST wall temperature T_{wall}=400K and displacement factor x=0.5

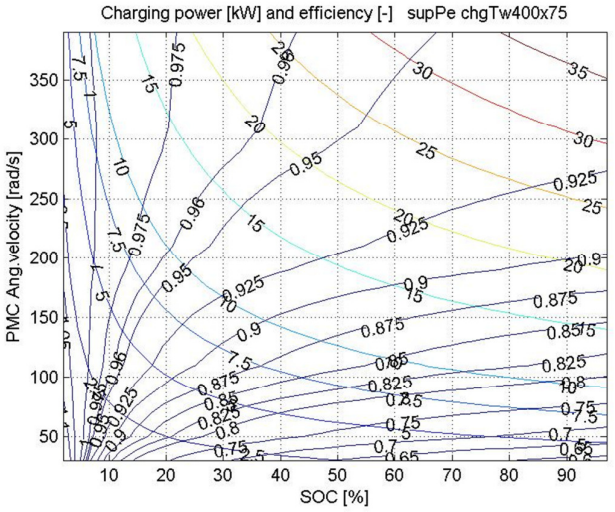

Figure AI-07– Global efficiency and available power during charging for AST wall temperature T_{wall}=400K and displacement factor x=0.75

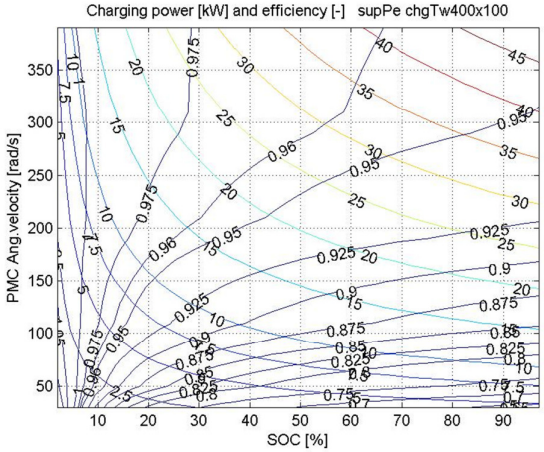

Figure AI-08– Global efficiency and available power during charging for AST wall temperature T_{wall}=400K and displacement factor x=1

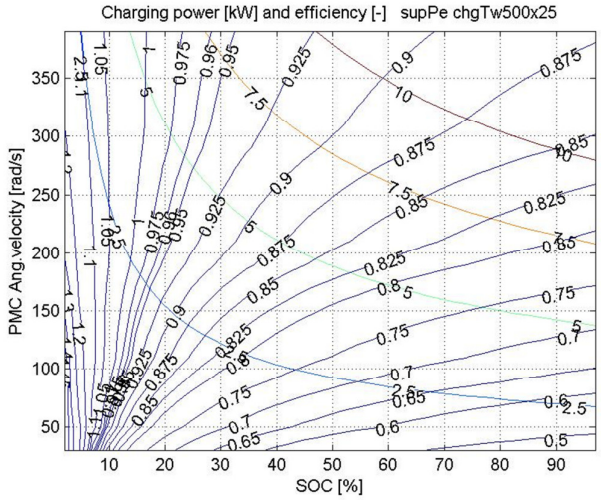

Figure AI-09– Global efficiency and available power during charging for AST wall temperature T_{wall}=500K and displacement factor x=0.25

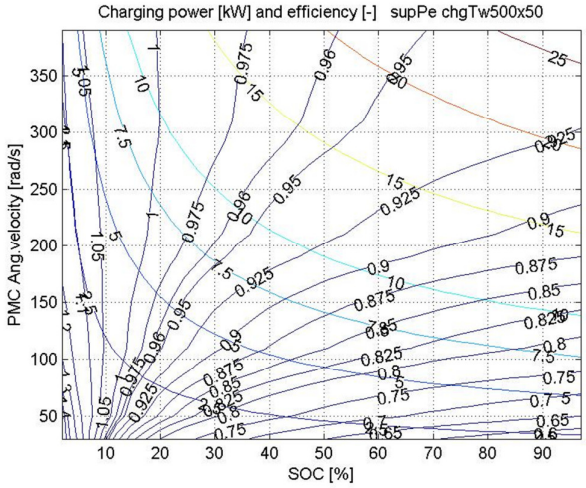

Figure AI-10– Global efficiency and available power during charging for AST wall temperature T_{wall}=500K and displacement factor x=0.5

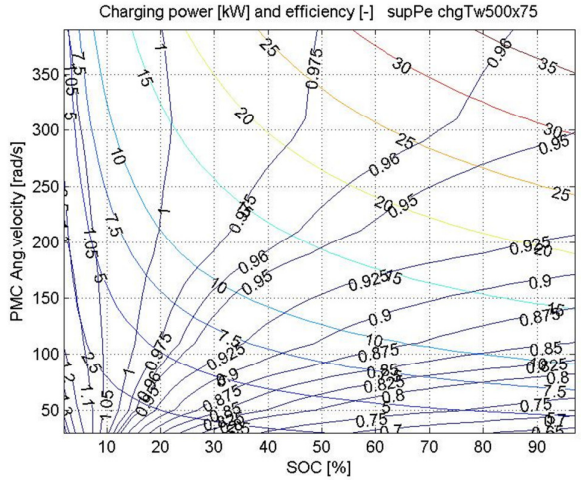

Figure AI-11– Global efficiency and available power during charging for AST wall temperature T_{wall}=500K and displacement factor x=.75

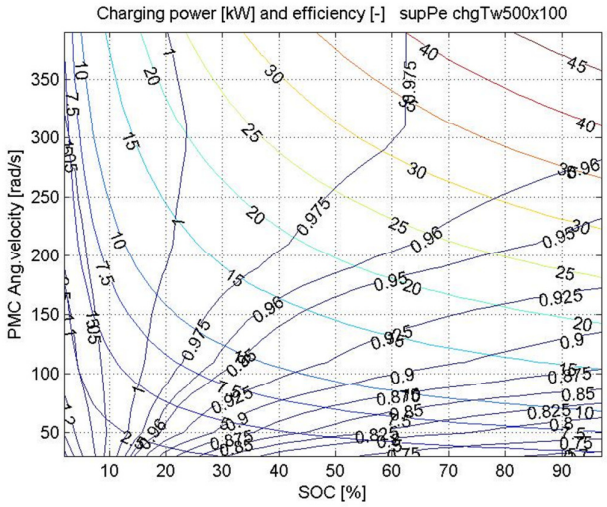

Figure AI-12– Global efficiency and available power during charging for AST wall temperature T_{wall}=500K and displacement factor x=1

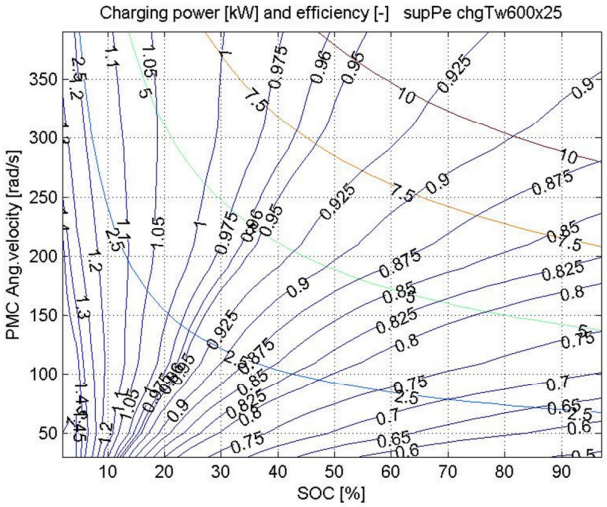

Figure AI-13– Global efficiency and available power during charging for AST wall temperature T_{wall}=600K and displacement factor x=0.25

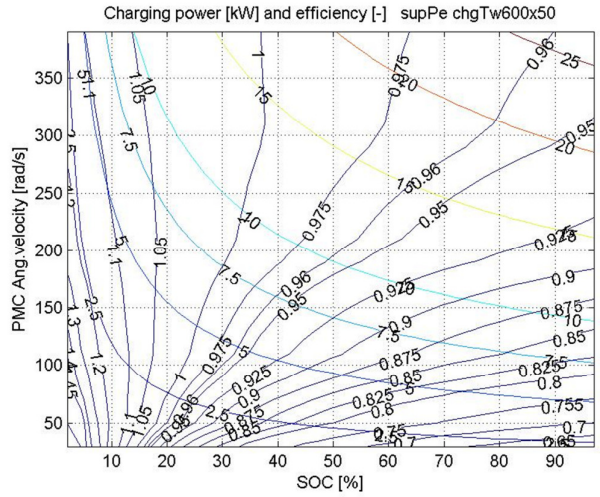

Figure AI-14– Global efficiency and available power during charging for AST wall temperature T_{wall}=600K and displacement factor x=0.5

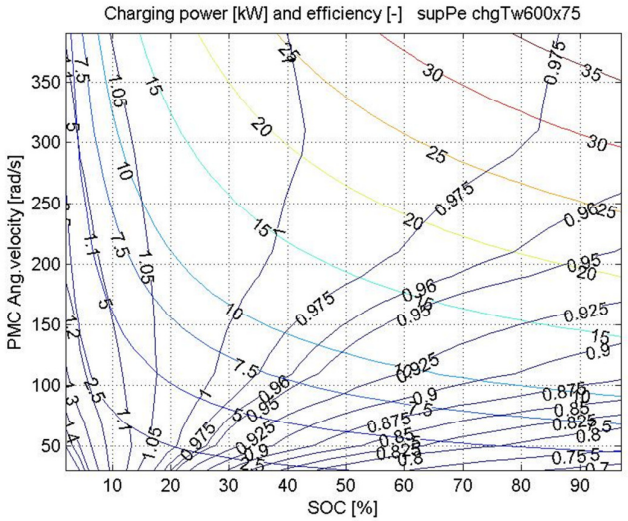

Figure AI-15– Global efficiency and available power during charging for AST wall temperature T_{wall}=600K and displacement factor x=0.75

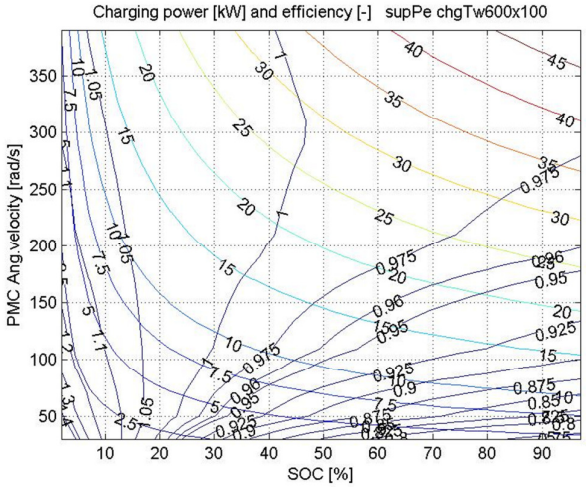

Figure AI-16– Global efficiency and available power during charging for AST wall temperature T_{wall}=600K and displacement factor x=1

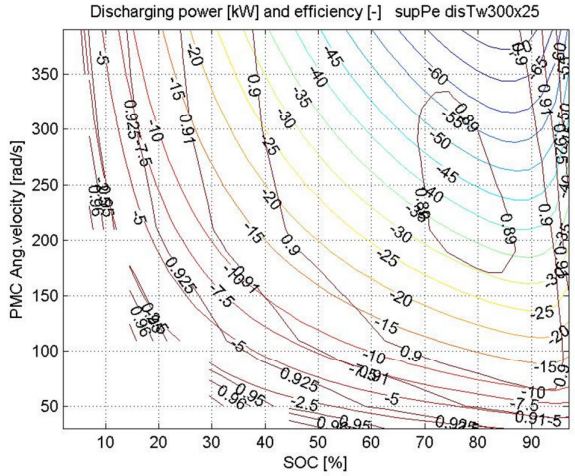

Figure AI-17– Global efficiency and available power during discharging for AST wall temperature T_{wall}=300K and displacement factor x=0.25

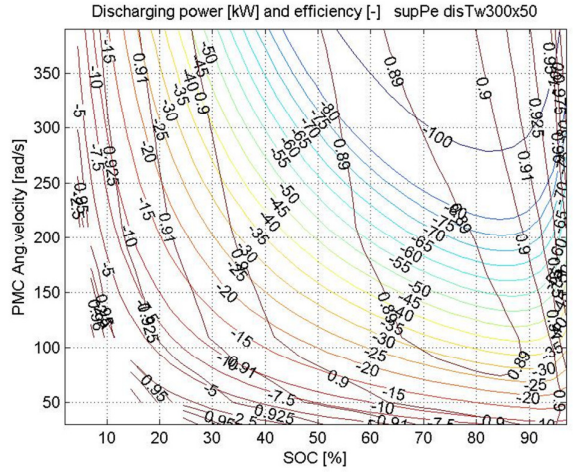

Figure AI-18– Global efficiency and available power during discharging for AST wall temperature T_{wall}=300K and displacement factor x=0.5

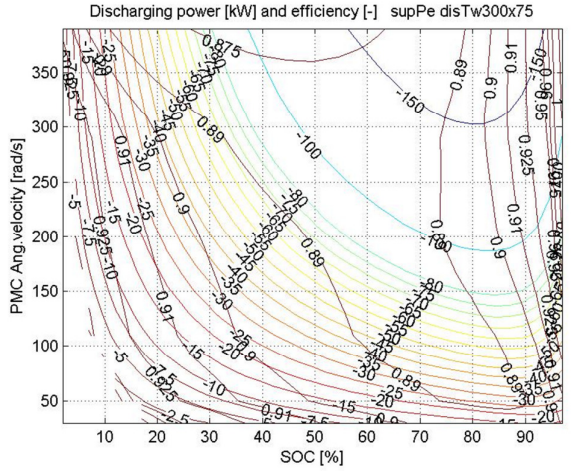

Figure AI-19– Global efficiency and available power during discharging for AST wall temperature T_{wall}=300K and displacement factor x=0.75

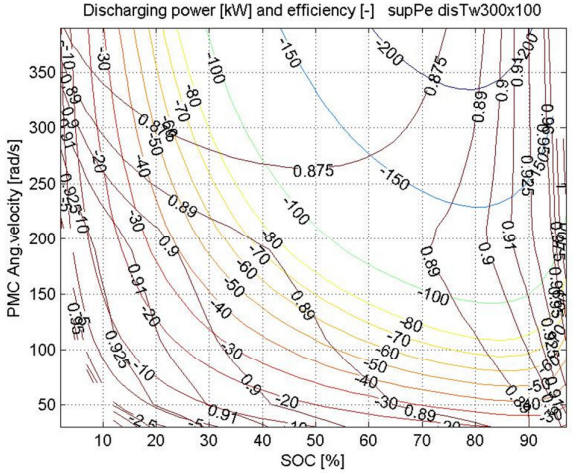

Figure AI-20– Global efficiency and available power during discharging for AST wall temperature T_{wall}=300K and displacement factor x=1

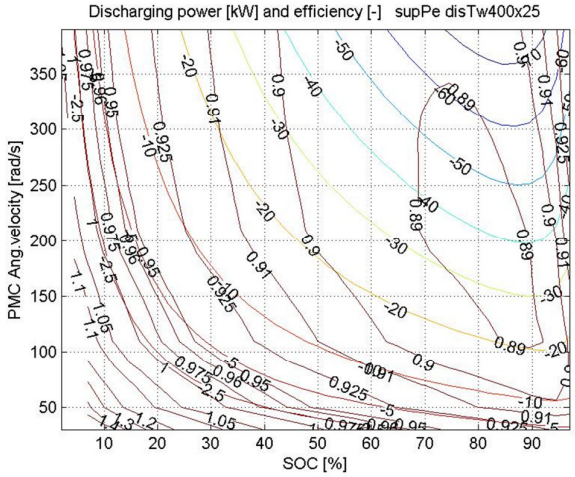

Figure AI-21– Global efficiency and available power during discharging for AST wall temperature T_{wall}=400K and displacement factor x=0.25

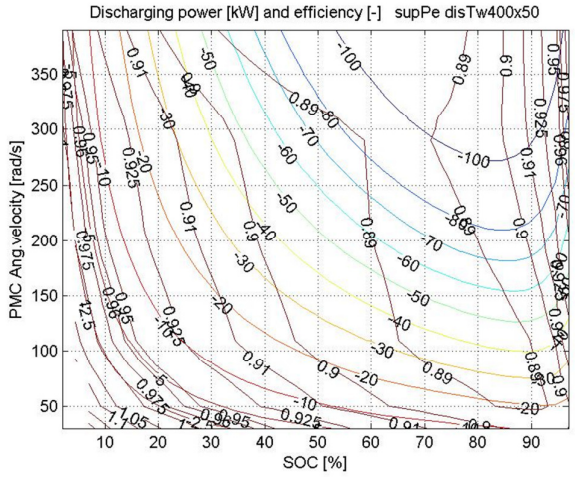

Figure AI-22– Global efficiency and available power during discharging for AST wall temperature T_{wall}=400K and displacement factor x=0.5

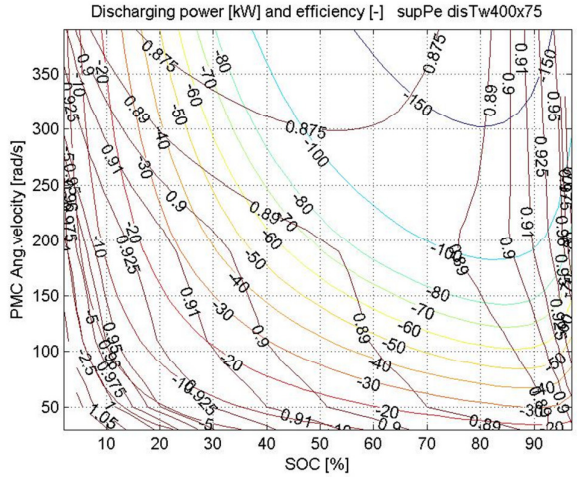

Figure AI-23– Global efficiency and available power during discharging for AST wall temperature T_{wall}=400K and displacement factor x=0.75

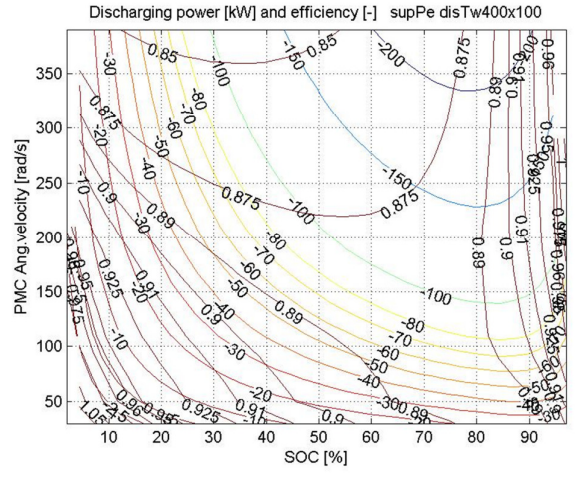

Figure AI-24– Global efficiency and available power during discharging for AST wall temperature T_{wall}=400K and displacement factor x=1

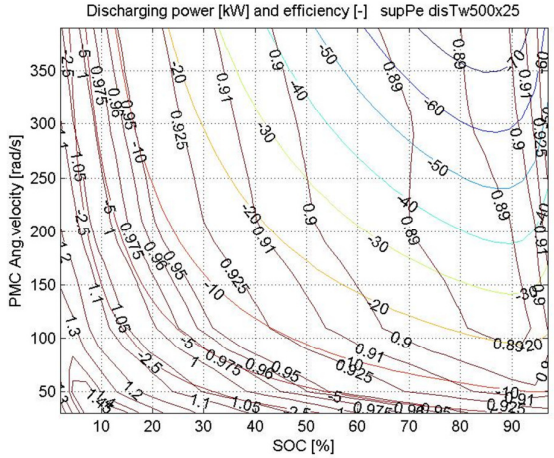

Figure AI-25– Global efficiency and available power during discharging for AST wall temperature T_{wall}=500K and displacement factor x=0.25

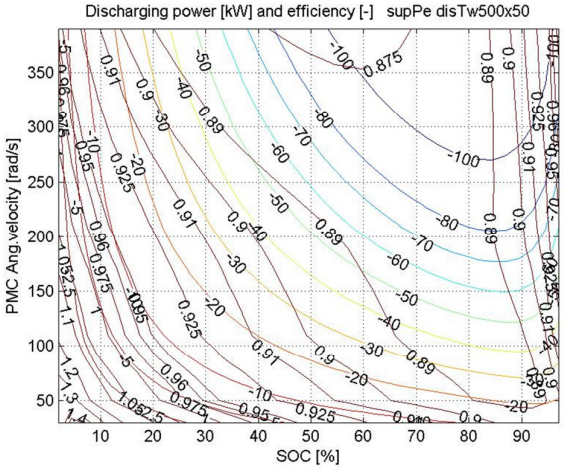

Figure AI-26– Global efficiency and available power during discharging for AST wall temperature T_{wall}=500K and displacement factor x=0.5

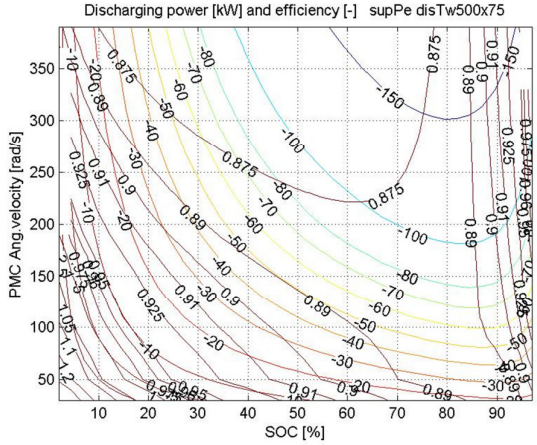

Figure AI-27– Global efficiency and available power during discharging for AST wall temperature T_{wall}=500K and displacement factor x=0.75

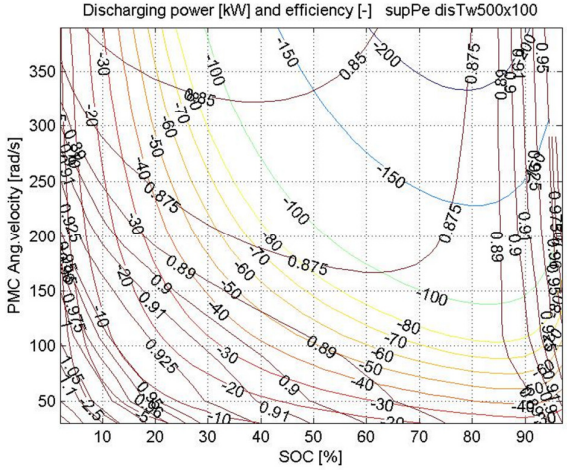

Figure AI-28– Global efficiency and available power during discharging for AST wall temperature T_{wall}=500K and displacement factor x=1

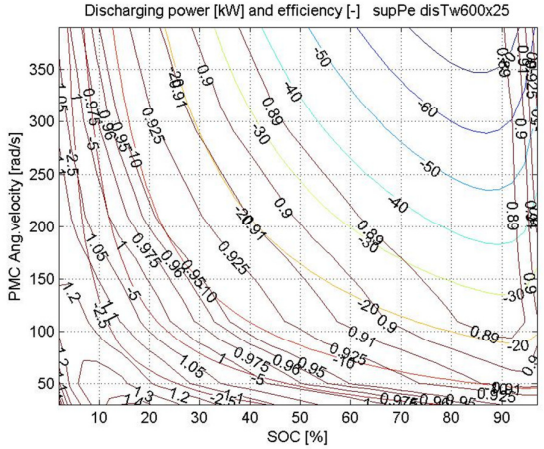

Figure AI-29– Global efficiency and available power during discharging for AST wall temperature T_{wall}=600K and displacement factor x=0.25

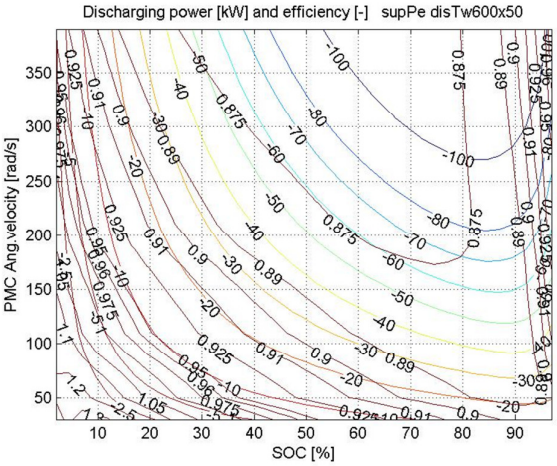

Figure AI-30– Global efficiency and available power during discharging for AST wall temperature T_{wall}=600K and displacement factor x=0.5

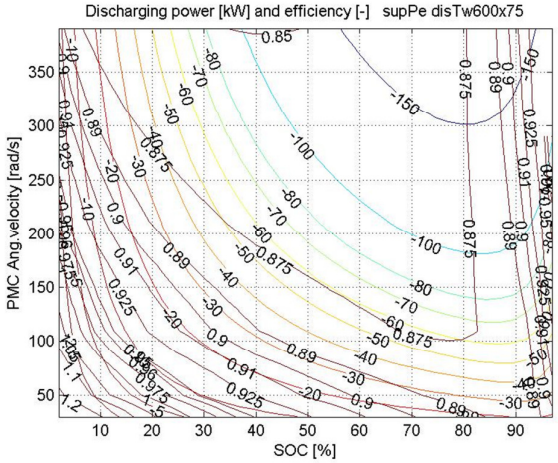

Figure AI-31– Global efficiency and available power during discharging for AST wall temperature T_{wall}=600K and displacement factor x=0.75

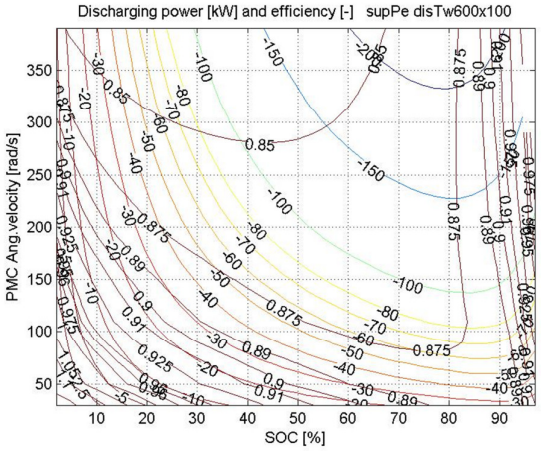

Figure AI-32– Global efficiency and available power during discharging for AST wall temperature T_{wall}=600K and displacement factor x

APPENDIX II

GLOBAL EFFICIENCY AND POWER ANALYSIS OF HYDRAULIC MOTORS AND PUMP ON BASIS OF COEFFICIENCT LOSS MODEL [47]

An example of efficiency maps and actual effective (shaft) power for one bent-axis hydraulic pump (V11-110) and motor (V11-110) build on the basis of [47] are given in this Annex. Methodology was described in Chapter 6.2.2. Global efficiency of the variable displacement Hydraulic Motor Pump is given as a function of three parameters – load, speed and the displacement.

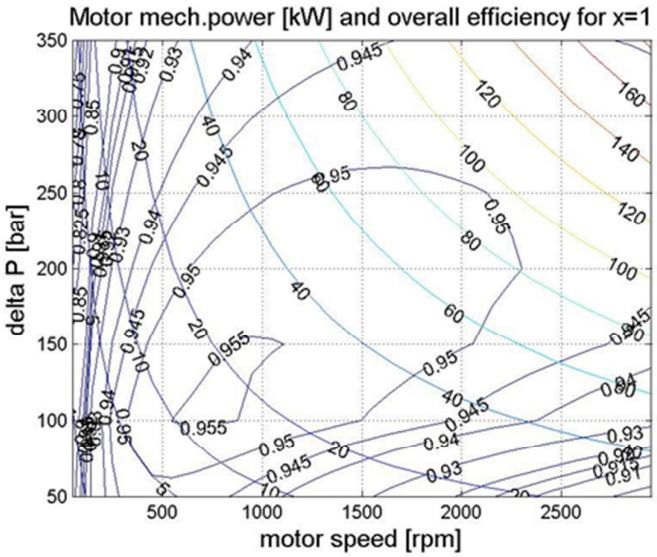

Figure AII-01 - Hydraulic motor V11-110 (110 cm^3/rev)

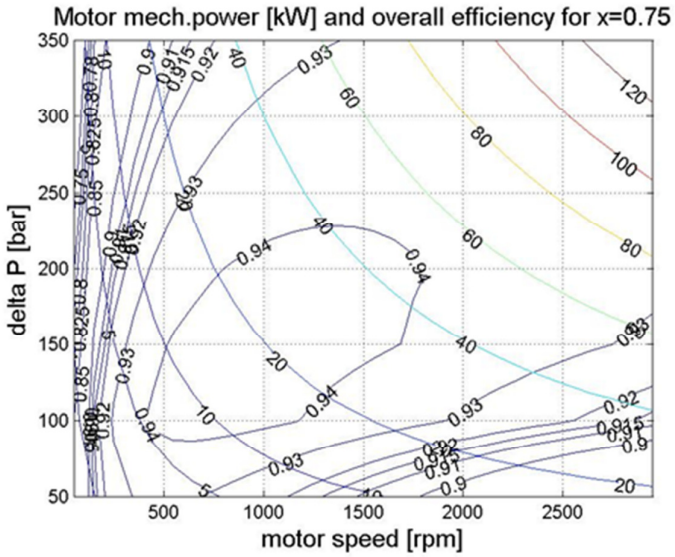

Figure AII-03 - Hydraulic motor V11-110 (110 cm^3/rev)

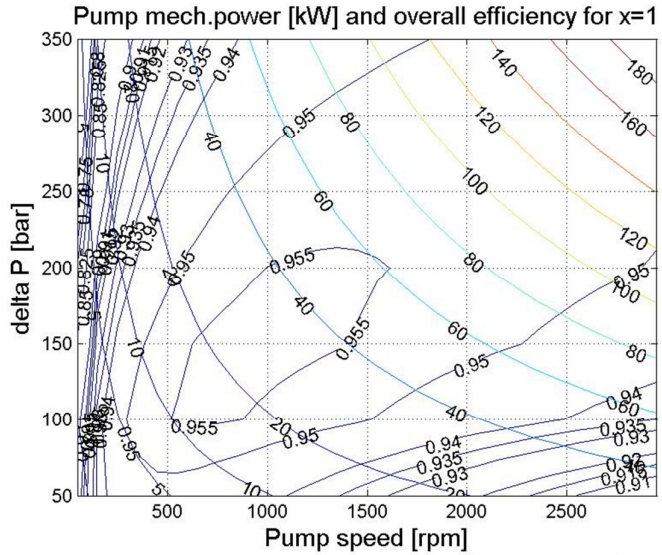

Figure AII-02 - Hydraulic pump V11-110 (110 cm^3/rev)

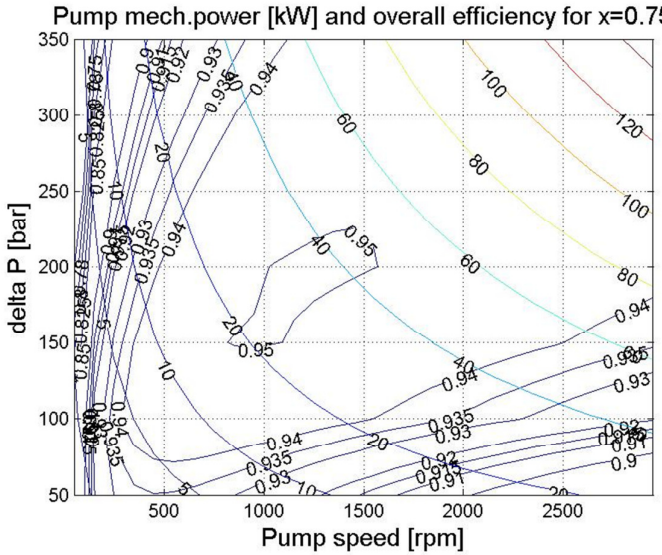

Figure AII-04 - Hydraulic pump V11-110 (110 cm^3/rev)

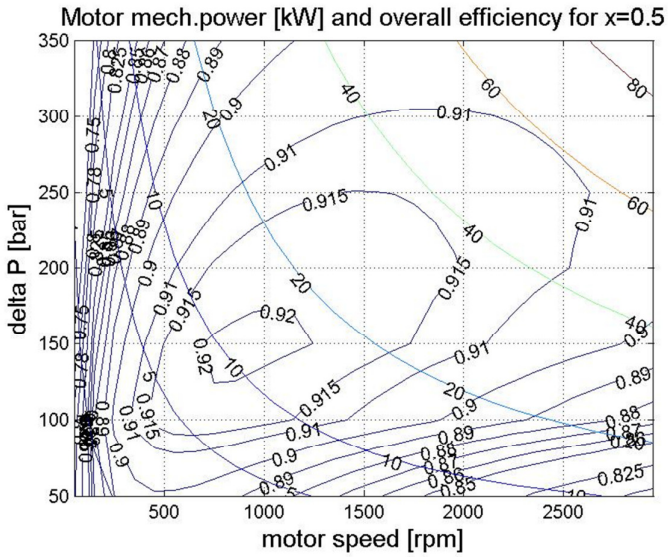

Figure AII-05 - Hydraulic motor V11-110 (110 cm^3/rev)

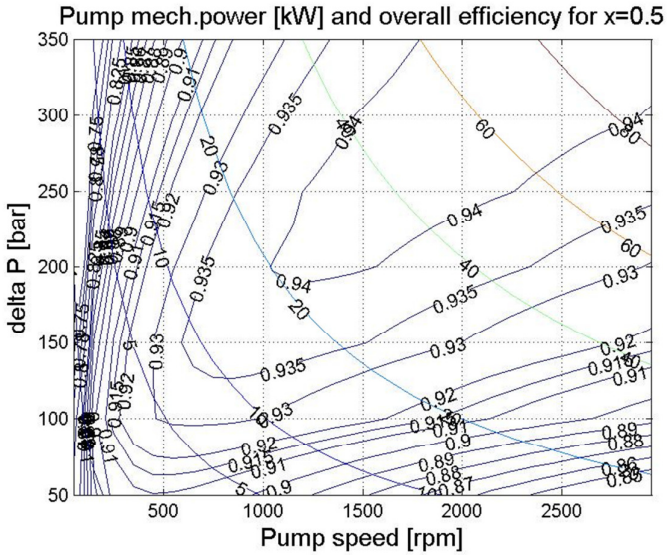

Figure AII-06 - Hydraulic pump V11-110 (110 cm^3/rev)

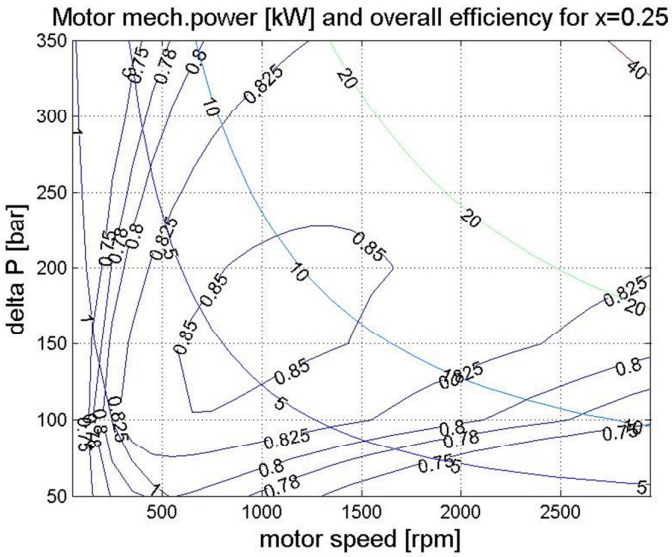

Figure AII-07- Hydraulic motor V11-110 (110 cm^3/rev)

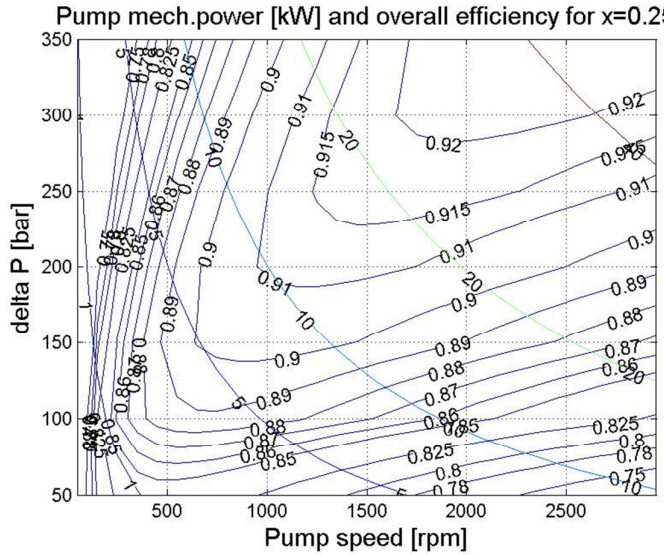

Figure AII-08 - Hydraulic pump V11-110 (110 cm^3/rev

CONTACT DETAILS:

Igor Trivić
Department of Energy Management, DA-E3
Advanced Development Division
IAV GmbH
Kauffahrtei 25
09120 Chemnitz
GERMANY
Email:igor.trivic@iav.de